Alma Mater Studiorum - University of Bologna

Faculty of Engineering

Department of Electric, Electronic and Information Engineering "Guglielmo Marconi"

Experimental Analysis and Numerical Simulation of Quench in Superconducting HTS Tapes and Coils

**Ph. D. Thesis
by
Marco Casali**

Coordinator:
Prof. Ing. Domenico Casadei

Supervisor:
Dr. Ing. Marco Breschi
Prof. Ing. Pier Luigi Ribani

Nothing is so good as an experiment which, whilst it sets an error right, gives us (as a reward for our humility in being reproved) an absolute advancement in knowledge.

Michael Faraday

Abstract

The quench characteristics of second generation (2 G) YBCO Coated Conductor (CC) tapes are of fundamental importance for the design and safe operation of superconducting cables and magnets based on this material. Their ability to transport high current densities at high temperature, up to 77 K, and at very high fields, over 20 T, together with the increasing knowledge in their manufacturing, which is reducing their cost, are pushing the use of this innovative material in numerous system applications, from high field magnets for research to motors and generators as well as for cables.

The aim of this Ph. D. thesis is the experimental analysis and numerical simulations of quench in superconducting HTS tapes and coils. A measurements facility for the characterization of superconducting tapes and coils was designed, assembled and tested. The facility consist of a cryostat, a cryocooler, a vacuum system, resistive and superconducting current leads and signal feedthrough. Moreover, the data acquisition system and the software for critical current and quench measurements were developed.

A 2D model was developed using the finite element code COMSOL Multiphysics®. The problem of modeling the high aspect ratio of the tape is tackled by multiplying the tape thickness by a constant factor, compensating the heat and electrical balance equations by introducing a material anisotropy. The model was then validated both with the results of a 1D quench model based on a non-linear electric circuit coupled to a thermal model of the tape, to literature measurements and to critical current and quench measurements made in the cryogenic facility.

Finally the model was extended to the study of coils and windings with the definition of the tape and stack homogenized properties. The procedure allows the definition of a multi-scale hierarchical model, able to simulate the windings with different degrees of detail.

Sommario

La comprensione e la valutazione dei fenomeni che causano una transizione allo stato normale dei materiali superconduttivi, denominati fenomeni di quench, sono alla base della progettazione dei magneti superconduttivi. Mentre tali comportamenti sono stati largamente indagati e compresi per magneti costruiti con superconduttori metallici a bassa temperatura critica (LTS), la scarsitá di dati sperimentali relativi ai piú recenti superconduttori ceramici ad alta temperatura critica (HTS) lascia aperti diversi interrogativi riguardanti il loro funzionamento.

Le caratteristiche di propagazione del quench degli YBCO coated conductors (CC), nastri superconduttivi di seconda generazione (2 G), sono di fondamentale importanza per la progettazione e l'utilizzo in sicurezza di cavi e magneti superconduttivi costruiti con questo materiale. La loro capacitá di trasportare elevate densitá di corrente ad alta temperatura, fino a 77 K, in campi molto elevati, superiori a 20 T, insieme con il crescente sviluppo del loro processo di produzione, che ne sta riducendo il costo, rendono l'utilizzo di questo materiale innovativo interessante in numerose applicazioni, dai magneti ad alto campo per la ricerca, ai motori, ai generatori, ai cavi per il trasporto di corrente.

Lo scopo della ricerca svolta durante il mio periodo di dottorato é stata l'analisi sperimentale e simulativa del quench in nastri e bobine in YBCO. Dapprima é stato progettato, assemblato e testato un impianto di misura per la caratterizzazione di nastri e bobine superconduttive. L'apparato di misura consiste in un criostato, un cryocooler, un sistema da vuoto, discendenti di corrente resistivi e superconduttivi e passanti del segnale. Inoltre sono stati sviluppati il sistema di acquisizione dati e il software per le misure di corrente critica e di quench.

Per quanto riguarda la parte simulativa é stato sviluppato un modello 2D agli elementi finiti utilizzando il codice commerciale COMSOL Multiphysics®. Il problema della modellazione dell'elevato rapporto di aspetto del nastro é stato affrontato moltiplicando lo spessore del nastro per un fattore costante, compensando le equazioni di bilancio del calore e dell'elettro-

dinamica stazionaria introducendo una anisotropia materiale. Il modello é stato convalidato sia con i risultati di un modello monodimensionale circuitale non lineare accoppiato ad un modello termico del nastro, sia con misure di letteratura, sia con le misure di corrente critica e di quench realizzate nella struttura criogenica precedentemente descritta.

Infine, il modello é stato esteso allo studio di bobine e avvolgimenti con la definizione delle proprietá omogeneizzate di un nastro e di una pila di nastri. La procedura permette la definizione di un modello gerarchico multi-scala in grado di simulare gli avvolgimenti con diversi gradi di dettaglio.

Contents

List of Figures

List of Tables

Introduction to Superconductivity

It was the beginning of the 20th century when in the Leiden laboratory of the Dutch physicist Heike Kamerlingh Onnes the liquefaction of helium, the last remaining gas to be liquefied, was achieved. The most common method to liquefy a gas is to compress it; however, if the temperature of that gas is higher than the critical point, even under strong pressure it is impossibile to achieve the liquid state.

In order to obtain the transition from the gas state to the liquid state it is important to know the minimun temperature at which this phenomenon can be seen, that is the critical point temperature, then to cool down the gas before compressing it.
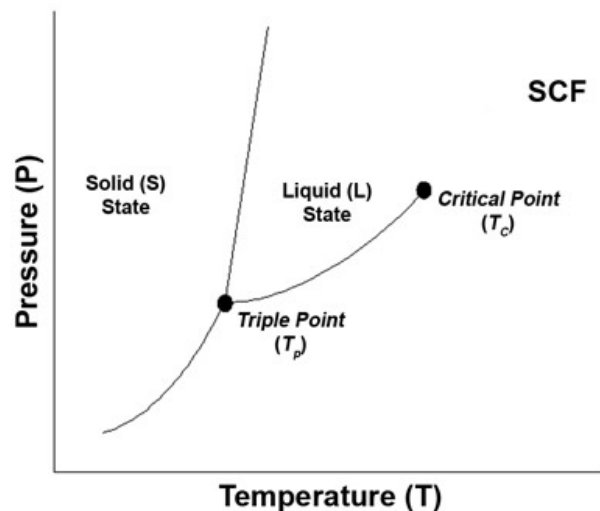
Figure (1.1)   *Phases Diagram.*

Element	T_c [K] at p_{atm}	T_c [K]	p_c [atm]
He	4.22	5.19	2.24
H_2	20.39	33.24	12.8
N_2	77.33	126.2	33.5
O_2	90.2	154.6	49.8
H_2O	373.15	647.096	217.7

Table (1.1)   *Critical temperature and pressure for some important gasses.*

As shown in Table (1.1) the transition temperature for helium is only 4.22 K. This means that the technologies needed to achieve that value should be very sophisticated and much more complicated than the clever but modest means needed for the other gasses.

Finally in 1908, after a sixteen-hour long experiment, the history of searching for "new liquids" was pushed to its end. As we can always see in the developing of science, after solving a problem a new one is ready to be investigated, thanks to the new discoveries. In fact, the liquefaction of helium was the fundamental step for the discovery of strange properties of some materials at very low temperature, thus opening a new chapter in solid-state physics.

In 1911 Onnes discovered that at a temperature close to 4 K the electrical resistance of mercury suddenly dropped to unmeasurable values.
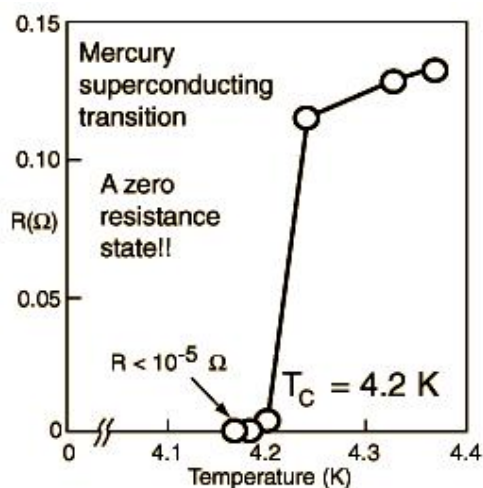
Figure (1.2)   *Discovery of superconductivity (H. Kamerling Onnes, 1911): resistance of mercury versus temperature.*

A large amount of experimental studies followed that incredible discovery leading to the finding of other materials with the same property but below different temperatures. It was suddenly seen that the temperature at which the resistivity drops to zero was a property of each material, which was called *Critical Temperature T_c*. However, the absence of any resistance is not the only fundamental characteristic of superconductors, as they also possess anomalous magnetic and thermal properties, so that it is more useful to talk about a new state of matter, as Onnes himself defined it in one of his papers:

> [...] *the mercury at 4.2 K has entered a new state, which, owing to its particular electrical properties, can be called the state of superconductivity* [1].

Since its first years this physical state of matter was considered very attractive by a large amount of physicists and engineers, as it was regarded, and with some restrictions it could be regarded also nowadays, as the natural case nearest to the concept of a "Perpetual Motion".

1.1 PROPERTIES OF SUPERCONDUCTORS

1.1.1 Electrotechnical basis

Before entering the world of superconductivity, it is useful to recall the behaviour of normal conductors.

An electrical conductor is a material that allows the current to flow easily through it. A current is nothing else than a net flux of electrons inside a material (although conventionally the direction of the current is the opposite with respect to the electrons motion) due to free electrons in the Valence Band (first species conductors), or thanks to the presence of ionic species which carry the current (second species conductors). Some examples of conductors are metals, water and the human body. The birth of a current has to be forced by an electric field, which drives the electrons to move from the negative potential to the positive one, in order to neutralize the difference of charge. According to the "Simplified Ohm's Law" current and voltage are linked in a proportional way, thanks to the *Resistance R* :

$$R = \frac{V}{I} \tag{1.1}$$

that is measured in Ohm $[\Omega]$ in the S.I.[1].

However, the Resistance depends on the geometry of the samples, so it is more useful to define the *Resistivity*, the resistance per unit of the cross section area S and unit of the length l, that is a unique function of the temperature, characteristic of every material:

$$\rho = R \cdot \frac{S}{l} \quad [\Omega\,\mathrm{m}] \tag{1.2}$$

As we can see from inverting the Eq. (1.1) at the same applied voltage a conductor, characterised by a small resistance, will lead a larger current with respect to a low conductive material. The explanation of this behaviour is that in a conductor, for example a metal, the *outerboundary-electrons* are not bound with a single atom, but they are shared among them, so they are allowed to flow across the lattice. Without an external force the chaotic movement will prevail, and no effect will be seen. Whereas in the presence of an electric field the motion forced by that field will prevail on the Brownian motion, leading the current to flow. The resistance is due to the loss of energy that these electrons undergo when they collide with the ions of the crystal lattice, growing with the presence of impurities inside the material, and with its temperature, which increases the thermal motion of the ions of

---

[1]International System of Units

the lattice around their site. Therefore, if we push a metal near the absolute zero, the resistance will tend to a very small value but not to zero due to the inevitable presence of some impurities.

Following *Matthiessen's Rule* the resistivity could be expressed as the sum of two contributions:

$$\rho = \rho_t + \rho_r \tag{1.3}$$

where ρ_t is the thermal component due to the vibration of the crystal lattice (which vanishes at absolute zero) while ρ_r is the residual resistivity due to the imperfections, and therefore it could be considered as a first rough measurement of the purity of a metal. Thus, an ideal crystal would have $\rho = 0$, while a real crystal has $\rho = \rho_r$. But the lack of resistance is not enough to classify a pure crystal as a superconductor. First of all because superconductors are characterized by a sudden drop of the resistance to zero regardless of their degree of purity; moreover they exhibit different thermal and magnetic behaviours.
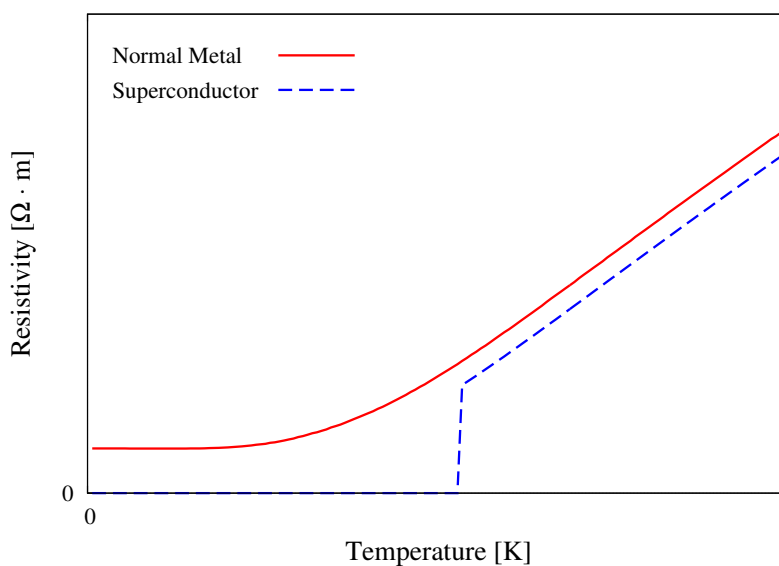
Figure (1.3)   *Resistivity vs temperature in an impure metal and in a superconductor.*

1.1.2 Meissner-Ochsenfeld Effect

In 1933 Meissner and Ochsenfeld discovered one of the fundamental properties of superconductors, by measuring the magnetic field distribution outside tin and lead samples. If we consider a PERFECT CONDUCTOR, with $\rho = 0$, we obtain from local Ohm's equation:

$$\boldsymbol{E} = \rho\boldsymbol{J} \quad \implies \quad \boldsymbol{E} = 0 \tag{1.4}$$

and from Faraday-Neumann-Lenz equation:

$$\boldsymbol{\nabla} \times \boldsymbol{E} = -\frac{\partial \boldsymbol{B}}{\partial t} \quad \implies \quad \boldsymbol{B} = cost \tag{1.5}$$

This means that in a perfect conductor the induction field is constant in time thus, the magnetisation state does not depend only on the external conditions, but also on the history of magnetisation.

As we can see from Fig. (1.4) the state of the magnetisation changes with the history of the magnetisation itself, keeping its initial value unchanged. In a SUPERCONDUCTOR the behaviour is different and really interesting: the magnetic field does not penetrate the superconducting sample and moreover it is ejected from it if the transition to superconducting state is forced to happen in a magnetic field [see Fig. (1.5)].

All metals other than ferromagnetics have zero magnetic induction in the absence of a magnetic field. The cause of this property is that the magnetic field due to the magnetic moment of any atom is oriented chaotically, so that
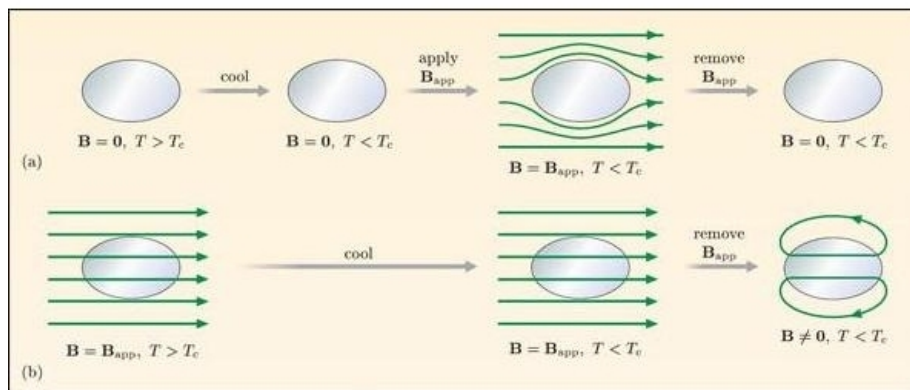
Figure (1.4)   *Magnetic behaviour of a perfect conductor.*
(a): Sample cooled down in absence of any magnetic field;
(b): Sample cooled down in the presence of a magnetic field.
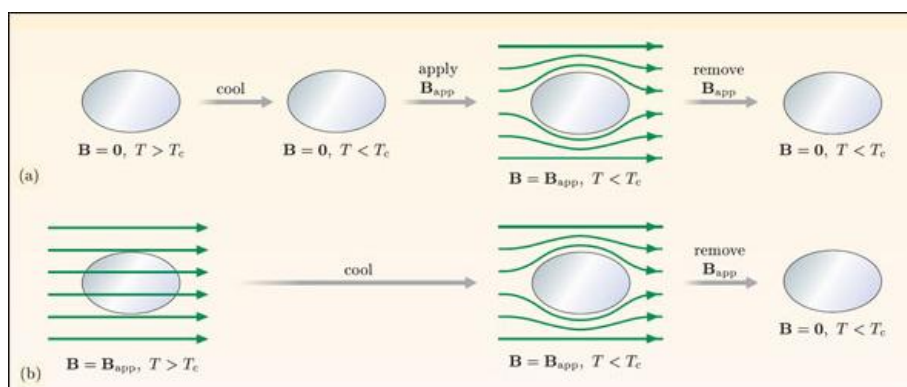
Figure (1.5) *Magnetic behaviour of a superconductor.*
(a): Sample cooled down in absence of any magnetic field;
(b): Sample cooled down in the presence of a magnetic field.

the magnetic moments cancel each other out. When an external field $\boldsymbol{H}$ is applied, there appears to be a finite induction field $\boldsymbol{B} = \mu\boldsymbol{H}$, where μ is the magnetic permeability.

In paramagnetic materials $\mu > 1$ so the applied field is enhanced; in diamagnetic materials $\mu < 1$ and the applied field is weakened ($\boldsymbol{B} < \boldsymbol{H}$). In a superconductor the Meissner effect implies $\boldsymbol{B} = 0$ also in the presence of $\boldsymbol{H}$, corresponding to zero magnetic permeability. This effect is called *Ideal Diamagnetism.*

As

$$B = B_i + B_e \tag{1.6}$$

where B_i and B_e are respectively the absolute values of the internal and external induction field, a superconductor must have an internal flux density opposite to the external one everywhere:

$$B_i = -B_e \tag{1.7}$$

or alternatively as $H_e = B_e/\mu_0$

$$M = -H_e \tag{1.8}$$

To oppose the applied field, thus having no magnetic induction inside the sample, an electrical current flowing in the surface layer of the supeconductor is needed, called **Surface Supercurrent**, which acts as a magnetic shield. As the resistance is zero that supercurrent will flow perpetually without dumping.
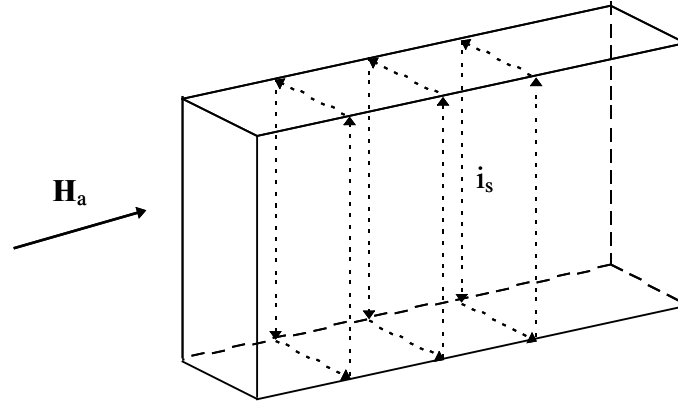
Figure (1.6) *Surface Supercurrents in the surface layer of the sample.*

Besides, if we consider the superconducting sample as homogeneous and amagnetic ($\mu = 1$), assigning the diamagnetic behaviour to the shielding currents ($\mu = 0$), from the Ampère-Maxwell law we find

$$\boldsymbol{\nabla} \times \boldsymbol{B} = \mu_0 \boldsymbol{J} \tag{1.9}$$

If $\boldsymbol{B}$ is zero inside the superconductors, $\boldsymbol{J}$ must be zero, too. Thus, the current cannot flow inside the superconductors, but only in their surface layer.

It is almost clear that the current cannot flow only in the surface of a material, as this implies an infinite current density, but it can penetrate a thin thickness ($10^{-6} \div 10^{-5}$ cm) that differs for every material and with the current density, called **Penetration Depth** λ. As the magnetic field decreases with an exponential law, the penetration depth is defined as the distance at which the field decreases by a factor e.

Like every superconducting parameter the penetration depth varies with the temperature, tending to infinity for $T = T_c$, which is when the materials turn to normal conducting state.

$$\lambda(T) = \frac{\lambda(0)}{\sqrt{1 - \left(\frac{T}{T_c}\right)^4}} \tag{1.10}$$

The penetration depth also grows with the presence of impurities. This characteristic is very important from an engineering point of view as if the penetration depth is too small, the current density able to flow in the cable will be so small that the superconductivity could not have any practical application.
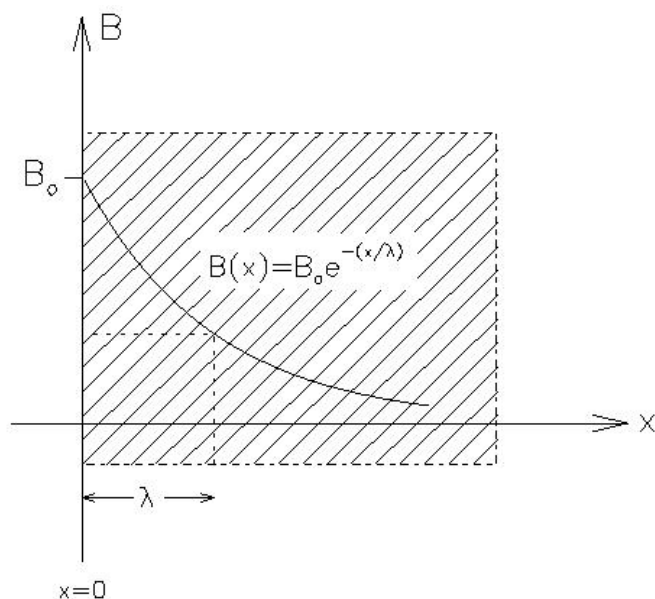
Figure (1.7)
Magnetic field B_0 at the surface of the supeconductor decays to B_0/e at a distance equal to λ inside a superconductor (shaded region).

1.1.3   Thermal Properties

We have already stressed that superconductivity is different from being only the absence of any electric resistance, but it is a real phase transition. The specific heat plot as a function of the reduced temperature $(T\backslash T_c)$ is a further evidence of this:
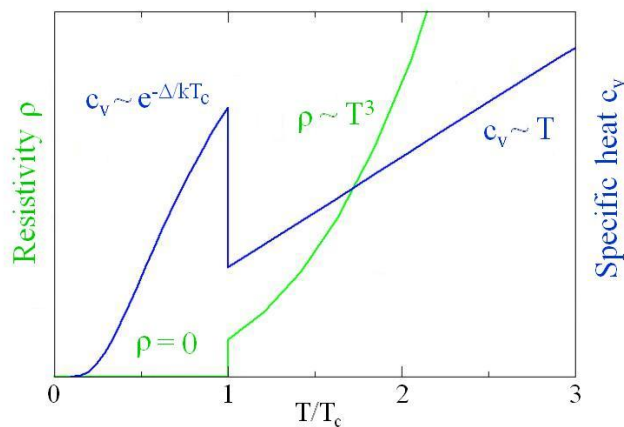
Figure (1.8)   *Resistivity and specific heat as a function of the reduced temperature.*

The heat capacity of any metal is made up of two contributions:

1. the *electronic heat capacity* due to the electrons;

2. the *lattice heat capacity* due to the crystal lattice.

As the electronic heat capacity decreases linearly with decreasing temperature, while the lattice one with the third power of the temperature, the latter one will be negligible for $T \to 0$.

The behaviour of a superconductor is rather different, in fact c_{el} does not decrease linearly with temperature but exponentially, as shown in Fig. (1.8), in agreement with:

$$\frac{c_{el}}{\alpha T_c} = a e^{-b(T_c/T)} \tag{1.11}$$

where a and b are two material constants independent of the temperature. This means that even a very small heat loss can lead to a strong cooling.

At $T = T_c$ we can notice a jump in the heat capacity, due to the transition to the normal conductive state. Nevertheless, the magnitude of this jump varies in different superconductors.

Also the thermal conductivity is characterized by some rather distinctive features.

As we know in the presence of a temperature gradient a metal is not in thermal equilibrium, a heat flux $P = -k\, dT/dx$ proportional to the temperature gradient arises. The proportionality constant k is the thermal conductivity, which depends on the material and on the temperature and, in analogy with the heat capacity, it can be written as the sum of an electronic and a lattice contribution.

There are several mechanisms of thermal conductivity, related to the different kinds of scattering processes, so those two contributions can be calculated as:

$$\frac{1}{k_{el}} \simeq \frac{1}{k_{el-lat}} + \frac{1}{k_{el-imp}} + \frac{1}{k_{el-el}} \tag{1.12}$$

$$\frac{1}{k_{lat}} \simeq \frac{1}{k_{lat-el}} + \frac{1}{k_{lat-imp}} + \frac{1}{k_{lat-lat}} \tag{1.13}$$

In normal metals the major role is played by the electronic thermal contribution $k_{el}^{-1} = aT^2 + b/T$, while in superconductors the temperature dependence is completely different and so the lattice contribution is considerably enhanced at $T < T_c$.

1.2 THEORIES AND MODELS

The discovery of superconductivity aroused an enormous interest. Many physicists tried their hand at explaining the disappearance of electrical resistance and the other features of the superconducting state, including Einstein, Heisenberg, Landau, Frenkel and many others.

A number of important phenomenological and microscopic theories were created, allowing to describe and predict, step by step, an increasing number of phenomena.

1.2.1 "Two Fluid" Model

The first important model was proposed in 1934 by C.J. Gorter and H.B.G. Casimir. It was a macroscopic model then called *"Two Fluid" Model*, because it assumes the contemporary presence of two electron carriers inside a superconductor:

1. the "normal" carriers, identical to those of the electron system in a normal metal;

2. the "superconducting" carriers, responsible for the anomalous properties.

The superconducting carriers, called **Superelectrons**, are able to flow inside the material without interaction with the lattice, that is with no dissipation of their energy.

We could think that for:

- $T > T_c$ there are only electrons;

- $T < T_c$ we are in the presence of both the contribution;

- $T = 0$ there are only superelectrons.

Actually we are able to have really zero losses only in Direct Current (DC), because the sample could be modelled as in Fig. (1.9).

In DC the current is carried only by the superconducting branch that short-circuits the branch of normal electrons. In fact, the electric field is not allowed inside the material, since it will accelerate the superelectrons indefinitely leading to a change in the current flow, by hypothesis constant. As a consequence, remembering Eq. (1.4), the current density must be zero, too.
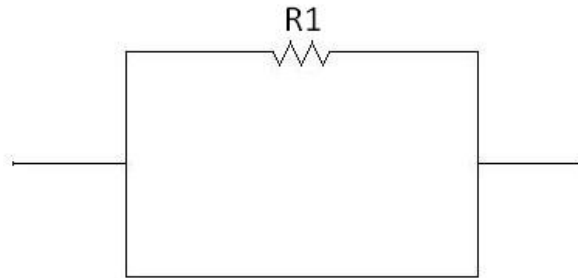
Figure (1.9)   *Equivalent circuit of a DC powered superconductor.*

In alternate current (AC) on the other hand, the electric field is necessary to accelerate the carriers, since the electrons change their direction of motion continuously. In that case we can model the circuit as in Fig. (1.10).

Thanks to their greater inertia superelectrons will follow the changes of $\boldsymbol{E}$, and behave as an inductance. So they cause a loss of energy due to the fact that a fraction of the current has to flow in the resistive branch. However, the magnitude of that phenomenon is much lower than many other losses inside a real superconductor, since the resistive fraction of current is very little (the induction in Henry is about 10^{-12} times the Ohm resistance). As we can imagine with increasing frequency the normal electron conduction will also increase, until reaching a critical value f_c [see Paragraph (1.3.3)] at which the sample will go back to the normal conductive state.
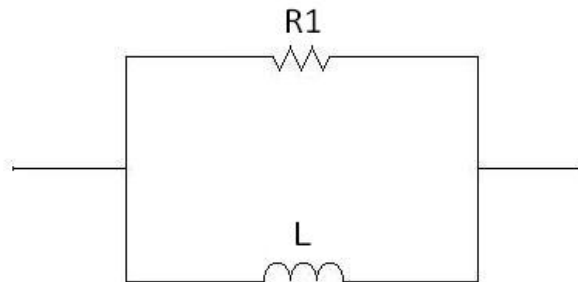
Figure (1.10)   *Equivalent circuit of an AC powered superconductor.*

1.2.2 Classical Model: the London's equations

In 1935 the London brothers proposed a macroscopic (non-quantic) model, that could explain the perfect conductivity and the Meissner effect of superconducting materials with two simple equations [2].

Let us consider a linear, homogeneous, isotropic and time-invariant medium with the electrons weakly bounded to the atoms and in thermodynamic equilibrium. Neglecting the reciprocal interactions between them, every electron feels a force made of two contributions:

$$m\frac{d\boldsymbol{v}}{dt} = \boldsymbol{F}_{em} + \boldsymbol{F}_{coll} \tag{1.14}$$

where $\boldsymbol{F}_{em} \simeq q\boldsymbol{E}$ is the force induced by the electric field and $\boldsymbol{F}_{coll} \simeq -m\boldsymbol{v}/\tau_{tr}$ is the collision term, with τ_{tr} mean time among two collisions. Hence we can write:

$$m\frac{d\boldsymbol{v}}{dt} = q\boldsymbol{E} - \frac{m\boldsymbol{v}}{\tau_{tr}} \tag{1.15}$$

In the presence of an electric sinusoidal forcing field of pulsation ω we have

$$\underline{v} = \frac{q\tau_{tr}}{m}\frac{1}{1 + j\omega\tau_{tr}}\underline{E} \tag{1.16}$$

so we can obtain the current density fasor:

$$\underline{J} = \frac{\sigma_0}{1 + j\omega\tau_{tr}}\underline{E} = \sigma(\omega)\underline{E} \tag{1.17}$$

where $\sigma(\omega)$ is the complex electrical conductivity. If we consider an electrical conductor as copper, characterized by $\tau_{tr} \simeq 2.4 \cdot 10^{-14}$, we can simply approximate the complex conductivity with the real value σ_0.

An interesting result of this model is that for $f \gg 1/\tau_{tr}$ the conductivity becomes purely complex, which means that the material has no losses. Physically this means that the electrons are oscillating so rapidly that they cannot cross a distance long enough to collide with any atom, they are fixed around a point, behaving as a dipole, so the current will flow without losses, as the only carriers are the superelectrons. The superelectrons must therefore not be affected by the collisions with the ions of the crystal lattice. Mathematically this is equivalent to set $\omega \gg 1/\tau_{tr}$, but it has to be valid also for $\omega = 0$, so the unique solution is that $\tau_{tr} \to \infty$, so:

$$\sigma(\omega) = \lim_{\tau_{tr} \to \infty}\left(\frac{n_s q_s^2 \tau_{tr}}{m_s}\frac{1}{1 + j\omega\tau_{tr}}\right) = \frac{1}{j\omega}\frac{n_s q_s^2}{m_s} = \frac{1}{j\omega}\cdot\frac{1}{\Lambda} \tag{1.18}$$

where $\Lambda = m_s/\left(n_s q_s^2\right)$. Applying this limit to the Eq. (1.17) we obtain the **First London Equation**:

$$\boxed{\boldsymbol{E} = \frac{\partial}{\partial t}(\Lambda \boldsymbol{J})} \tag{1.19}$$

and it is easy to see that the factor Λ is strictly connected with the penetration depth

$$\lambda = \sqrt{\frac{m_s}{\mu_0 n_s q_s^2}} \tag{1.20}$$

If we apply the curl operator to Eq. (1.19)

$$\boldsymbol{\nabla} \times \boldsymbol{E} = \boldsymbol{\nabla} \times \frac{\partial}{\partial t}(\Lambda \boldsymbol{J}) \tag{1.21}$$

remembering Eq. (1.5) we obtain:

$$\frac{\partial}{\partial t}\left[\boldsymbol{\nabla} \times (\Lambda \boldsymbol{J}) + \boldsymbol{B}\right] = 0 \tag{1.22}$$

Assuming that there was a time when magnetic fields and currents did not exist we can write the **Second London equation**:

$$\boxed{\boldsymbol{\nabla} \times (\Lambda \boldsymbol{J}) = -\boldsymbol{B}} \tag{1.23}$$

We shall underline that the system formed by the London's equation does not explain the origin of superconductivity; it is only a mathematical model that reproduces the experimental results and the presence of the penetration depth and the Meissner Effect with very good accuracy. Those equations do not substitute the Maxwell's equation but they are restrictive conditions of them in the superconducting domain. However, they cannot explain the penetration of the magnetic field in Type II superconductors [see 1.4].

1.2.3 BCS Theory

The BCS Theory was postulated in 1957 by three American physicists, John Bardeen, Leon Cooper and John Robert Schrieffer, who won the Nobel prize in 1972 [3]. This was the first microscopic theory which explained every phenomenon of superconductivity and also nowadays it is considered the best one to explain the behaviour of the metallic materials (both Type I and II), even though it shows remarkable disagreements with the results obtained with the new ceramic High Temperature Superconductors (HTS) materials as for example YBCO.
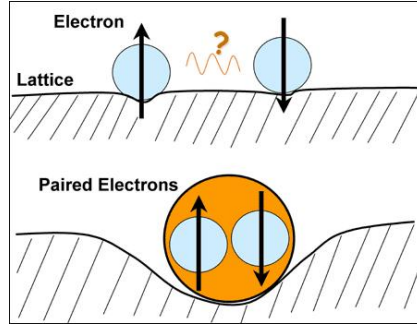
Figure (1.11) *Formation of a Cooper pair.*

This model says that to explain the strange nature of superconductivity the interaction between electrons and the crystal lattice must be taken into account. It turns out that this interaction leads to attraction between the electrons in a superconductor. Normally two electrons will repel each other since they have the same charge. However we are not considering the problem of two isolated electrons; the electrons are located in a medium that can change the nature of their interaction.

An electron moving in a metal deforms, or polarizes, the crystal lattice. In fact, when it passes in the vicinity of an ion it will be attracted to it by the Coulomb force. Also the ion will move in the direction of the electron, causing a displacement of the ions in the lattice. This displacement will result in a more positive charged zone that flows in the medium as a wave with a peculiar momentum and energy. The magnitude of this positive charge can exceed the electron charge attracting another electron.

At normal temperature the thermal motion is however strong enough to push particles apart from each other and wash away the ion "coat", which reduces the attractive force. On the other hand at very low temperature the thermal motion will become negligible and those attractive forces will prevail.

At $T = 0$ K a metal is not at absolute rest but it executes the so called "zero-point" vibrations, since the quantum mechanics does not permit a zero value for the energy as a consequence of the Heisenberg uncertainty principle. An electron moving in the crystal disrupts this order of vibration exciting the lattice. The lattice will recover its ground state emitting some energy that can be absorbed by another electron.

The crystal lattice behaves as a set of harmonic oscillators of energy

$$E = \sum_{q_i} \hbar\Omega_{q_i}\left(n_{q_i} + \frac{1}{2}\right) \tag{1.24}$$

so we can see that $E_0 = 0.5 \cdot \sum_{q_i} \hbar\Omega_{q_i}$ and not zero. Using the *Quasiparticle Method* created by the physicist L. D. Landau we can consider the oscillating system as a set of n_{q_i} quasiparticles, called *Phonons* or "sound quanta" each of energy $\hbar\Omega_{q_i}$. A quasiparticle is not a real particle in the usual sense but a convenient representation of an excited state (as photons are an excitation of the electromagnetic field). This concept allows us to deal with an easier model of collision between particles of two kinds: electrons and phonons.

The electron-phonon interaction leads to an attraction between electrons that in some materials (superconductors) can be larger then the Coulomb repulsive force if the two electrons are separated by a distance lower than the coherence length [see Section (1.4)]. This new particle formed by two electrons is called **Cooper Pair** and has a larger degree of order with respect to the single electron, explaining why the electrons in superconductors prefer to stay in pairs and do not dissipate energy interacting with the lattice. The **Energy Gap** Δ between a Cooper Pair and an electron is simply defined as the energy needed to separate the two electrons of the pair and as usual it depends on the temperature:

$$\frac{\Delta(T)}{\Delta(0)} = \left(1 - \frac{T}{T_c}\right)^{1/2} \qquad (1.25)$$

explaining the existence of a critical value for the temperature, at which the energy gap disappears.

The formation of such a pair is not sufficient for the superconductivity to emerge; this phenomenon requires a certain number of those new particles, that are formed at T_c.

(a) *Electron-phonon interactions can occur over long distances.*

(b) *Energy Gap between Cooper pair and crystal lattice levels.*
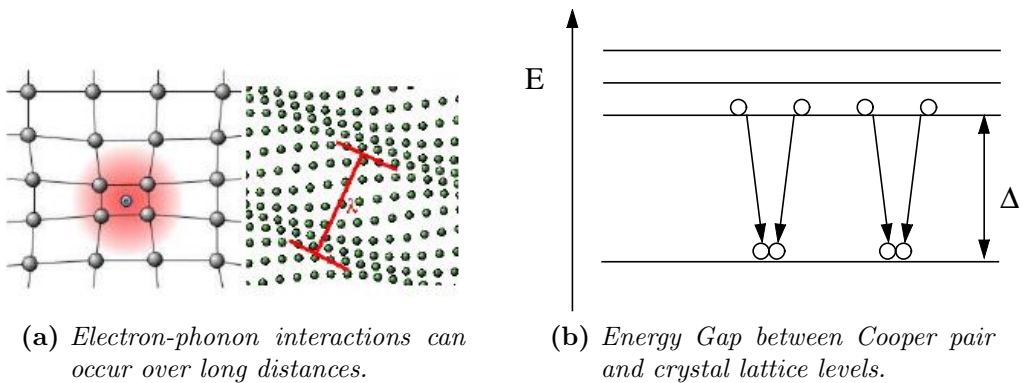
Figure (1.12) *Characteristics of the Cooper pairs.*

1.3 CRITICAL PARAMETERS

As already stressed superconductivity is a state of matter that can be seen below a certain temperature, called critical. But this is not the only parameter that can lead to a change from superconducting properties to normal conducting ones: we can see a transition to the normal conductivity state also at temperatures below T_c.

The other main parameters that characterize the superconducting state are:

- **Critical Field H_c;**

- **Critical Current Density J_c;**

- **Critical Frequency f_c.**

It is useful to define some experimental correlations that link the three most important parameters (T_c, H_c, J_c), in order to describe the so called *Critical Surface* which separates the state of superconductivity from the normal state [see Fig. (1.13)].
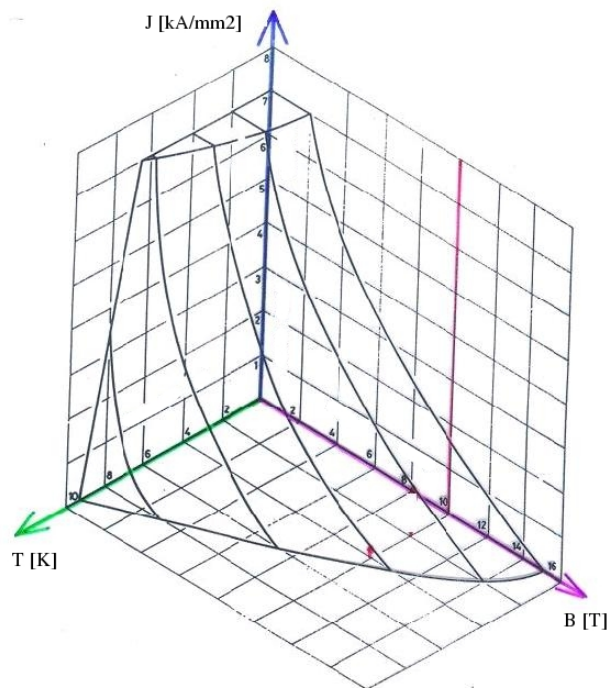
Figure (1.13) *Critical Surface.*

1.3.1   Critical Field

In the presence of an external field larger than H_c, the Meissner effect will disappear and the superconductor will lose its properties. In fact an external magnetic field could give to the Cooper pairs enough energy to excite them, splitting the electrons.

Considering a superconductor parallel to the external magnetic field, we can see the behaviour shown in Fig. (1.14). Superconducting materials exhibit a magnetisation that acts against the external applied field [Eq. (1.8)], until reaching the critical value H_c, where the magnetic field suddenly penetrates the sample. The value of this critical parameter is different in different materials, but it is, as usual, strictly linked to the temperature.

Experimental studies have shown that the dependence of H_c on the temperature could be approximatively expressed by the following relation:

$$H_c\left(T\right) = H_c\left(0\right) \cdot \left[1 - \left(\frac{T}{T_c}\right)^2\right] \qquad (1.26)$$

allowing the characterisation of a superconductor by only $H_c(0)$ and T_c.
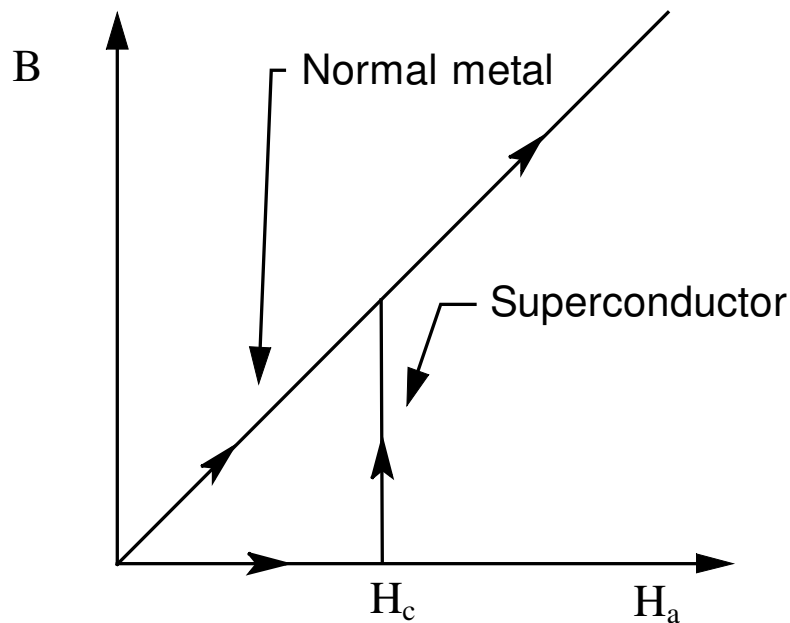
Figure (1.14)   *Magnetic behaviour of a superconductor.*
The arrows represent the reversibility of the process, true only in case of pure materials.
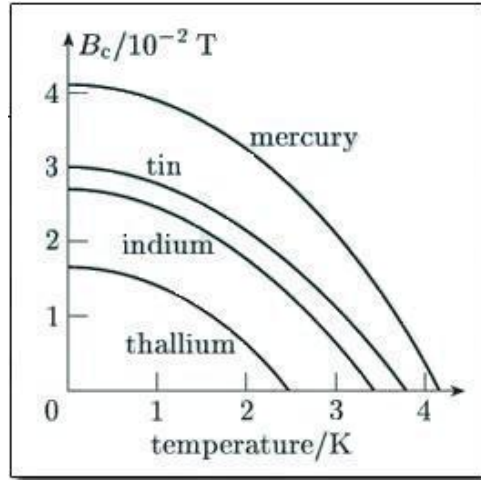
Figure (1.15)   *Phase Diagram $B_c(T)$ for various materials.*

1.3.2   Critical Current Density

The current flowing in a material is generally divided in two contributions:

- $\boldsymbol{J_t}$, the transport current;

- $\boldsymbol{J_s}$, the screen current (due to the presence of a change in the magnetic field applied).

The existence of the limitation in the current density is due to the fact that when $\boldsymbol{J} = \boldsymbol{J_s} + \boldsymbol{J_t}$ flows in a superconductor there will be a magnetic field H inside it, too (but not an induction field as for a superconductor $\mu = 0$). If the value of the resulting H is, in any point, larger than H_c then a local resistance will rise leading to a local transition to the normal state.

1.3.3   Critical Frequency

A superconductor, submitted to an electromagnetic field variable in time, loses its properties at frequencies larger than a threshold ($f_c \simeq 10^{11}$ Hz).

As already stressed the Cooper pairs are characterized by a lower energy state. However when the frequency of the applied field is high enough ($h\nu = \Delta$), the produced photons could have the energy to excite the pairs, bringing them to a higher level (usual electrons).

In usual applications of superconductivity the frequency of the applied magnetic fields is always much lower than the critical value, so this phenomenon is not very important.

1.4 Type I and Type II Superconductors

Superconductors are also divided into two classes depending on their behaviour in the presence of a magnetic field. In fact, thanks to the non-uniform distribution of the field lines in a superconducting sample of generic shape, the intensity could exceed the critical value also for $H < H_c$ in some regions leading to a local transition.

This particular contemporary presence of macroscopic "normal" and superconducting zones, shown in both classes, is called *Intermediate State* and could be explained only assuming the presence of a superficial tension between the two phases, that is a force that holds those phases balanced.

The behaviour of the sample will vary with the sign of this energy. For positive values in fact the formation of few large zones will be preferred while for negative values the sample will form many little normal zones, in order to minimize the free Gibbs energy of the body.

To understand the meaning of the superficial tension we must introduce a new physical concept. The density of Cooper pairs n_s decreases to zero near a superconducting/normal-conducting interface with a characteristic length ξ, proportional to the mean free path of the conduction electrons, called *coherence length*. As a consequence the boundary between the two zones is not sharp.
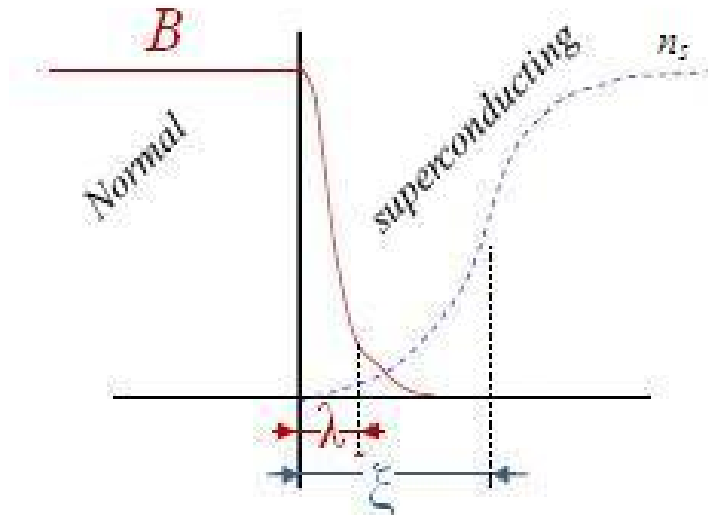
Figure (1.16) *Penetration Depth and Coherence Length at the boundary between normal and superconducting zone.*

A good approximation of the superficial tension energy is:

$$E_s = \frac{1}{2}\mu_0 H_c^2 \left(\xi - \lambda\right) \tag{1.27}$$

Type I superconductors have $\xi > \lambda$ so $E_s > 0$, for that reason the formation of local normal zones is not energetically favoured and the material tends to remain in the superconducting state until the magnetic field reaches the critical value H_c.

Type II superconductors, on the other hand, have $\xi < \lambda$, so the formation of normal zones could be favoured if the negative contribution of the superficial tension is greater than the positive one held by these normal zones. The transition from the superconducting state to the normal conductive state is not as sharp as in Type I superconductors. When the magnetic field reaches a value, specific of every material, called *Lower Critical Field H_{c1}* it may penetrate inside the sample. This state is called **Mixed State** in order to differentiate it from the so called Meissner State, characterized by the absence of any magnetic field.

In the Mixed State the normal zones (normal cores) are surrounded by supercurrents which shield them from the superconducting material so that they are crossed by fixed flux quanta called *fluxoids*. Those Fluxoids repel each other so they arrange themselves into regular hexagons, in order to minimize their free Gibbs energy. As the external field increases, their density grows until the transition of the whole material to the normal state at the *Upper Critical Field H_{c2}*.
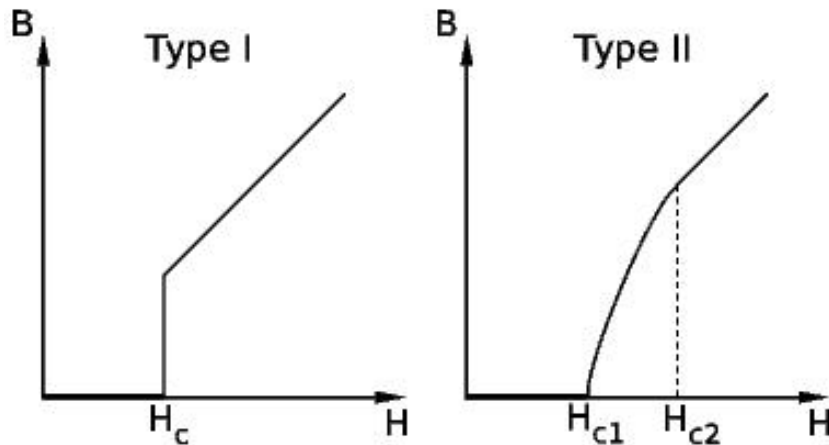
Figure (1.17) *Different behaviour of the magnetic induction in Type I and Type II superconductors.*

Although similar we must not confuse the Mixed State with the Intermediate State. The latter one in fact will appear in Type I superconductors due to the non-uniform distribution of the flux line of the magnetic field for a sample of any geometry and it is not energetically favoured. The first one instead is a peculiar characteristic of Type II materials and it is energetically favoured.

Defining the **Ginzburg-Landau constant** [4]

$$\chi = \frac{\lambda}{\xi} \tag{1.28}$$

it was established that the magnetic behaviour of the superconducting materials changes at the value of $1/\sqrt{2}$:

- $\chi < 1/\sqrt{2} \quad \Rightarrow \quad E_s > 0$ Type I;

- $\chi > 1/\sqrt{2} \quad \Rightarrow \quad E_s < 0$ Type II.

Pure metals usually have $\chi < 1/\sqrt{2}$ so they belong to Type I materials except for Niobium, Vanadium and Technetium. Impure metals and alloys have a much higher value of χ and so they belong to Type II materials.
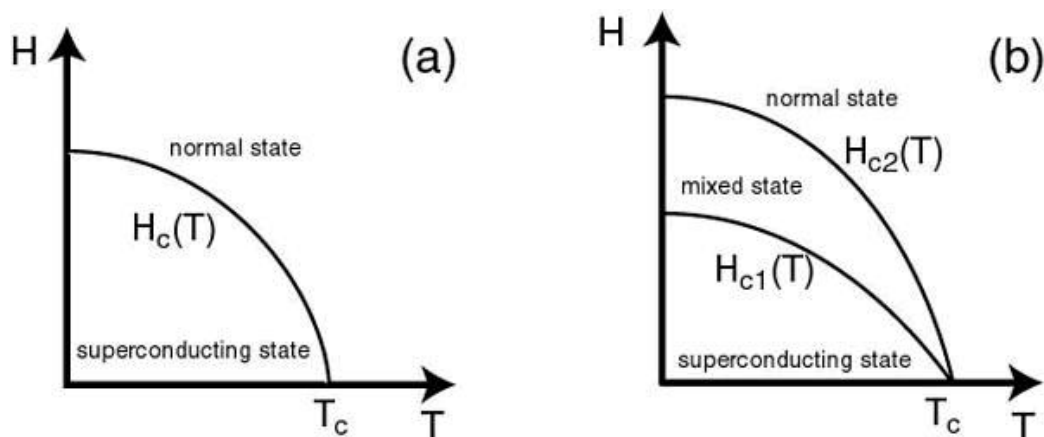
Figure (1.18)   *Differences in the Phase Diagrams H(T) between a Type I and a Type II superconductor.*

1.5 REAL SUPERCONDUCTORS AND PINNING

The flow of superconducting currents does not generate heat and therefore one of the first ideas of application of those materials was to use them to obtain strong magnetic field. However the value of such a field could not exceed the critical value H_c. To estimate its magnitude we can start from the following formula:

$$\frac{H_c^2}{8\pi} = E_b$$

where E_b is the energy needed to destroy the Cooper pair which is proportional to $v\Delta$ (with v number of electronic states per unit energy interval).

Remembering that the highest value of the magnetic field is reached for $T = 0$ and that from BCS theory $\Delta(0) = 1.76\, T_c$, we obtain:

$$H_c(0) \sim v^{1/2}T_c \tag{1.29}$$

Thus, for ordinary superconductors $H_c \approx 10^2 \div 10^3$ G; it is not sufficient for practical applications.

Element	T_c [K]	H_c [G]	Element	T_c [K]	H_c [G]
Al	1,196	99	Re	1,698	198
Cd	0,56	30	Ru	0,49	66
Ga	1,091	51	Sn	3,72	305
α-Hg	4,15	411	Ta	4,48	830
β-Hg	3,95	339	Th	1,368	162
In	3,4	293	Ti	0,39	100
Ir	0,14	19	Tl	2,39	171
α-La	4,9	798	α-U	0,68	-
β-La	6,06	1096	γ-U	1,8	-
Mo	0,92	98	W	0,012	1
Os	0,655	65	Zn	0,875	53
Pb	7,19	803	Zr	0,65	47

Table (1.2)   *Critical temperature and field of Type I superconductors.*

As we can see from Table (1.2) Type I superconductors have a small critical field. The situation in Type II superconductors is different because those compounds can exist in the so called mixed state where the field is not completely expelled. This makes it possible to obtain strong magnetic fields as we can see from Table (1.3). It is important to notice that a Type I

material could be turned to Type II simply by doping it with some impurities; this is precisely the reason why most alloys are Type II SC. The doping process in fact leads to a decrease in ξ and a corresponding rise in χ [see Eq. (1.28)].

Element	T_c [K]	$\lambda(0)$ [nm]	$\chi(0)$ [nm]	H_{c2} [T]
Nb-Ti	9.5	240	4	13
Nb-N	16	200	5	15
Nb$_3$Sn	18	65	3	30
MgB$_2$ (dirty)	32-39	140	6	35
YBa$_2$Cu$_3$O$_7$	92	150	1.5	>100
Bi-2223	108	200	1.5	>100

Table (1.3) *Critical temperature and field of Type II superconductors.*

However an ordinary Type II superconductor has a very low value of the critical current density. The magnetic field inside the vortex cores, present in the mixed state, will interact with the transport current generating a Lorentz force that will start moving the normal zones. Strong losses will arise associated with this movement and therefore a voltage drop will be observed at the ends of the sample.

The picture changes if the sample contains large inhomogeneities, due for example to plastic deformations, dislocations of the crystal lattice or inclusions of other phases. Those defects, called **Pinning Centers**, attract the vortex cores, fixing them and thus, preventing the heat losses.

Such materials termed "hard" superconductors, in opposition to "soft" SC possess large critical currents and are therefore suitable to be used in high power applications. Their critical current density depends on the size of the inhomogeneities and on the magnitude of the field.

The Lorentz force

$$\boldsymbol{F}_L = \boldsymbol{J} \times \boldsymbol{B} \tag{1.30}$$

pushes the vortex to move in a direction perpendicular to both the current and the magnetic field, with a fixed velocity u. For constant current and applied field, voltage and dissipated power will be constant too:

$$V = \frac{d\Phi}{dt} = \Phi_0 \, n_v \, h \, u \tag{1.31}$$

$$P_d = i \, \Phi_0 \, n_v \, h \, u \tag{1.32}$$

The constant velocity of the vortices implies the existence of a braking force F_P in the opposite direction with respect to the Lorentz force: the pinning force. Until $F_L < F_P$ there will be no movement of the fluxoids and therefore no dissipation.

There are different mechanisms that push the fluxoids to motion:

- **Flux-Flow**: a collective motion of all the normal zones;

- **Flux-Creep**: the fluxoids can jump from a pinning center to another due to energy released by the thermal motion (negligible for the traditional superconductor but important for the HTS where the thermal energy is higher);

- **Flux Jump**: a collective but discontinuous movement due to mechanical, electrical or thermal stresses.

However the pinning phenomenon is not only a positive characteristic of hard Type II superconductors because an irreversibility of magnetism is associated with it, as we can see from Fig. (1.20). The fluxoids are in fact anchored to the pinning centers and therefore they are not free to move and to reply quickly to any variation of the magnetic field.
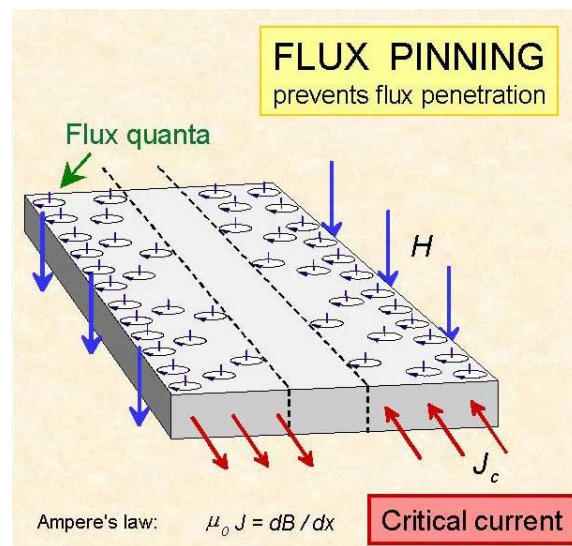
Figure (1.19) *Sketch of the Pinning.*
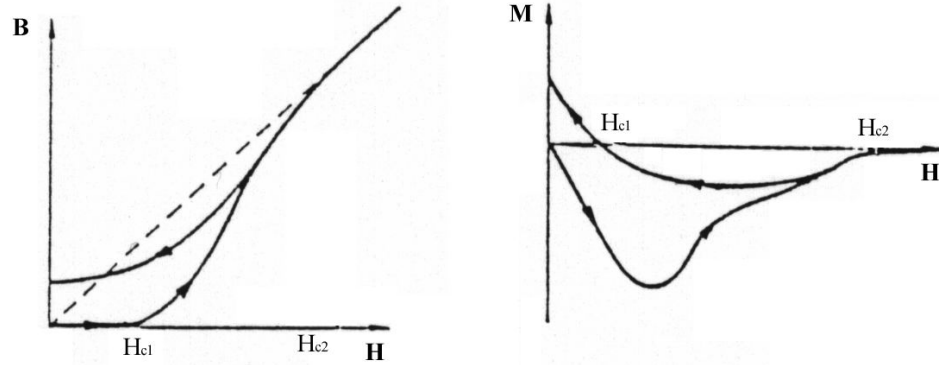
Figure (1.20)   *Irreversible magnetization curves for hard Type II supercon-ductors.*

Hysteresis is a cause of dissipation of energy for a superconductor sub-mitted to a time variable magnetic field. The magnitude of those losses is larger than that due to the flow of normal electrons, always present, as the-orized by the two fluids model, and it is proportional to the area behind the magnetisation curve:

$$W_d = \oint H \cdot dB \qquad (1.33)$$

1.6 APPLICATIONS

Many applications of superconductivity were realized in the past century, thanks to their peculiar and unique properties, both small scale, for electronics, and large scale, for conduction of large currents, power applications and energy storage [5].

Magnetic confinement of hot deuterium-tritium plasma is for example the most promising route towards the commercial production of power from controlled thermonuclear fusion. Superconductivity is needed in the reactor in order to contain the power consumption, which will probably exceed the electrical output of the station with conventional magnets. In the figure below we can see the design of **ITER** (International Thermonuclear Experimental Reactor) to be built in Cadarache, France, to demonstrate the scientific and technological feasibility of fusion power production as well as its potential environmental benefits.

Superconductivity is also essential for High Energy Physics applications [6], which need magnetic fields not achievable with conventional technology in order to accelerate, focus, manipulate and analyze the beams of energetic charged particles used to investigate the fundamental structure of matter. Superconducting magnets are therefore needed, since they are cheaper, more compact and can produce higher fields. Those magnets are built into a cryostat, in order to achieve the operating temperature, and the coils are in the form of cylindrical solenoids, often split into two halves to allow better access to the magnet bore.
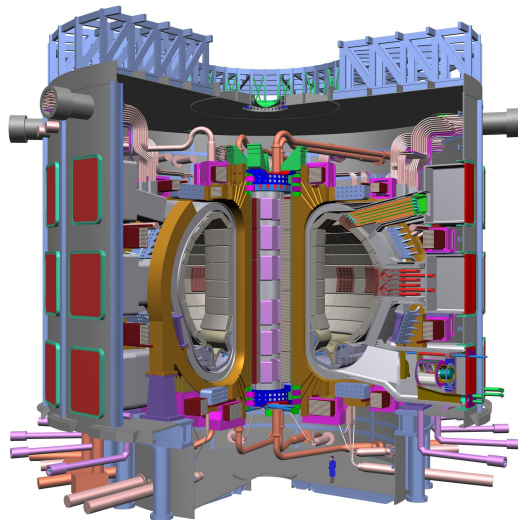
Figure (1.21)   *Conceptual design of the ITER tokamak.*
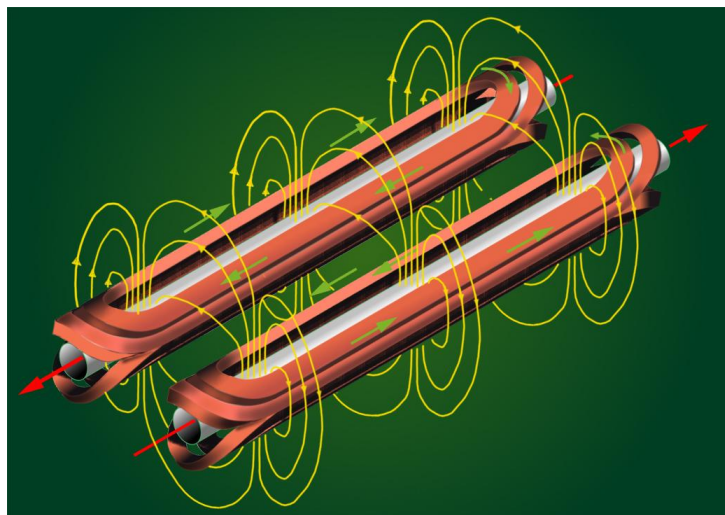
Figure (1.22) *Superconducting windings design of the LHC main dipole magnets.*

ITER is based on the tokamak principle: the plasma is confined into a toroidal volume by a toroidal (TF) and a poloidal field (PF) while it is heated by plasma currents, induce to flow in the longitudinal direction by the changes in the central solenoid field (CS). All magnet coils so far foreseen are superconducting.

Magnetohydrodynamic (MHD) generation is a technique for the direct conversion of thermal energy to electric energy. It uses directly hot combustion gases as working substance making significant savings in the use of fossil fuels by improving the efficiency of electrical power generation. The gases must be made electrically conducting by doping them with an easily ionized seed material. They are then forced to flow into a transverse field. The dynamo effect causes an e.m.f. to be induced and so D.C. electric power could be extracted.

Superconducting electric motors can be more efficient, smaller and much lighter than conventional ones. For this reason many prototypes, both D.C. and A.C., were designed and tested, especially in marine propulsion. But the most important application in the transport section is the **Magnetic levitation**. The so called **Maglev** is a train which can reach speeds up to about $600 \, km \, h^{-1}$. The stable levitation can be achieved using superconducting magnets at the bottom and on the side of the train, very close to the normal conductive rails. As the vehicle accelerates, eddy currents are induced in the rails thus, producing a magnetic field in the opposite direction to the field

Figure (1.23) *A Magnetic levitation train.*

produced by the superconducting magnets, giving levitating and stability forces. There are no moving parts to wear out or make a noise, the ride is smooth and high speeds may be reached safely.

Other interesting applications of superconductivity are the **Energy Storage** inside circuits called SMES, the **Magnetic Separation**, used to purify steel or in processes of mineral extraction, water purification and removal of sulphur from coal, and the **Magnetic Resonance Imaging (MRI)**, which is the most important commercial application.
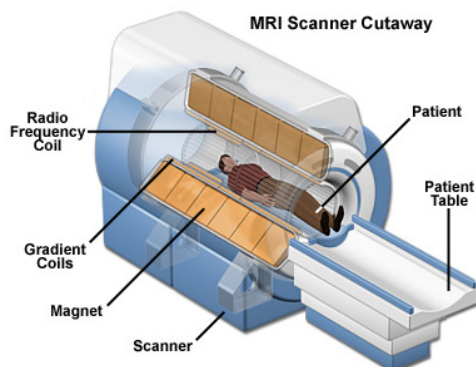
(a) *Design of an MRI machine.*

(b) *Scan of a human head using the MRI process.*

1.7 HTS SUPERCONDUCTORS

Since the discovery of superconductivity great efforts have been undertaken in order to find new superconducting materials with critical temperatures as high as possible. The scientist dream was, and still it is today, the occurrence of superconductivity at ambient temperature, thus solving the cryogenic needs and costs.

A revolutionary series of discoveries were made in the "80s" of the past century after the publication of the Alex Müller and Georg Bednorz paper entitled "*Possible High T_c Superconductivity in the Ba-La-Cu-O System*" [7]. The new material was a copper oxide, a La_{2-x}-Ba_x-Cu-O_4 compound with the superconducting properties strongly dependent on x. The fact that this material displayed High Temperature Superconductivity (HTS) came as a surprise since previous research had been indicating that the progress in T_c was connected with improvements in niobium-based materials, as indicated by Fig. (1.24). The superconducting phase of this new type of superconductors is a layered perovskite with a strongly anisotropic crystal structure.

Several months after the achievement of a transition temperature of 40 K in the $La_{1.85}$-$Ba_{0.15}$-Cu-O_4 material, a 95 K superconductor consisting of a mixed phase of yttrium, barium, copper and oxygen was discovered, thus allowing the superconductivity to occur in liquid nitrogen.
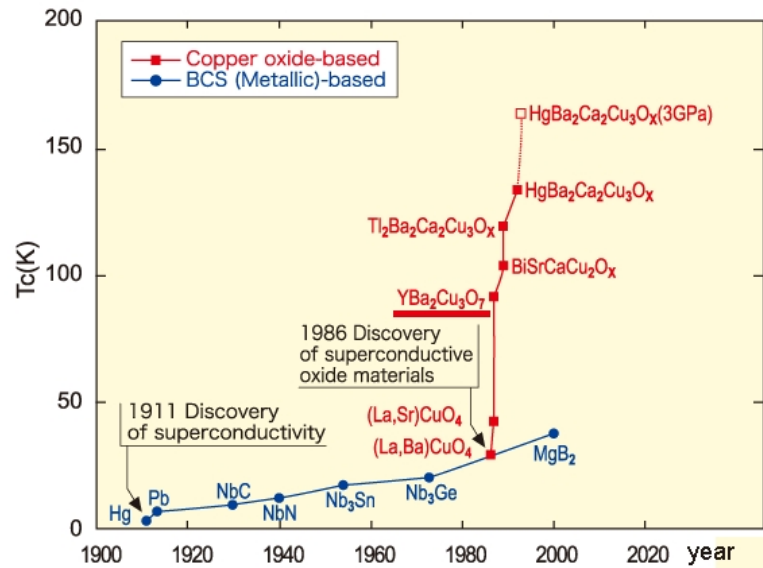
Figure (1.24) *Critical temperature increase with time.*

This superconductor has the stoichiometry $Y_1Ba_2Cu_3O_7$ and its crystal lattice structure is reported in Fig. (1.25). This structure is an oxygen-defect cubic perovskite where the yttrium and barium are on the corner sites and alternate between them. Moreover, there are strategic oxygen vacancies with no oxygen in the yttrium plane and two oxygen missing from the Cu-O layer between the barium planes. The crystal anisotropy affects the electrical transport properties, which are also anisotropic, with the high-conductivity direction parallel to the planes and due to conduction in the planes.

Soon it was found that most of the rare-earth elements could be substituted for yttrium without significant effects on critical temperature. Bi-Sr-Ca-Co-O (BSCCO), Tl-Ba-Ca-Cu-O and Hg-Ba-Ca-Cu-O raised the upper limit of the critical temperature up to 125 K.

This thesis deals with the electro thermal characterization of YBCO Coated Conductor tapes. Since their discovery, hard work has been done to improve their fabrication techniques and their use in application devices. Nowadays current leads and small magnet for MRI largely employ this material, but a deep knowledge is mandatory for the substitution of the widely used LTS in large magnets for research as well as in motors and in cables for the transport of current.
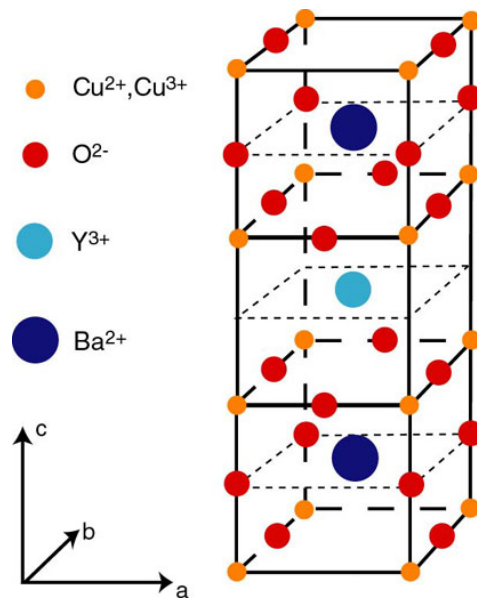
Figure (1.25)   *Crystal structure of the $Y_1Ba_2Cu_3O_7$.*

Chapter 2

Experimental facility

One of the most challenging tasks during my PhD. research was the development of a facility for measurements at cryogenic temperatures. The achievement and maintenance of temperatures needed for superconductivity to occur is in fact difficult and the engineering knowledge required covers a broad range of aspects, from the mechanical, thermal and electric properties of metals at cryogenic temperatures to the correct use and monitoring of vacuum technology, and low temperature acquisition system. Many handbooks have already dealt with this topic [8], [9], [10] but I can say from experience that nothing can prepare you to frustration and inevitable mistakes as the personal practice and reasoning, especially with experts in the field of superconductivity as those with whom I had the pleasure of working.

The facility with which I have obtained the experimental results presented in this thesis, through which I could validate the numerical code developed and presented in Chapter 3, consists of many different parts:

- a Cryostat;

- a Cryocooler;

- a Vacuum System;

- resistive and superconducting Current Leads;

- Signal Feedthrough.

Some of the parts were already present at the beginning of my research while others had to be designed and bought, as in the case of the superconducting current leads, or designed, developed and manufactured, as the voltage measurements system. However, the entire facility had to be assembled and tested before observing the first superconducting transition.

Moreover, I designed and developed the data acquisition system and the software for critical current and quench measurements in a LabVIEW environment. In this Chapter every part of the facility, as well as the LabVIEW code, will be described and explained.

2.1 CRYOSTAT

The cryostat is a device able to maintain the cryogenic temperatures of samples and devices mounted inside it. The cryostat tested and used during my research, visible in Fig. (2.1a), is a volume enclosed into three Stainless Steel shields which protect the environment from radiation heat transfer, designed and manufactured by Alca Technology Srl.

Inside the measurement chamber two copper plates are present and thermally anchored to the refrigeration machine, the cryocooler, thus providing heat sinks at two different temperatures. An internal view of the cryostat is reported in Fig. (2.1b). As can be seen, the superconducting samples are usually mounted on the top copper plate, the 2nd stage of the cryostat, which is characterized by the lower temperature, set to 4 K as it will been explained later in Section (2.2).
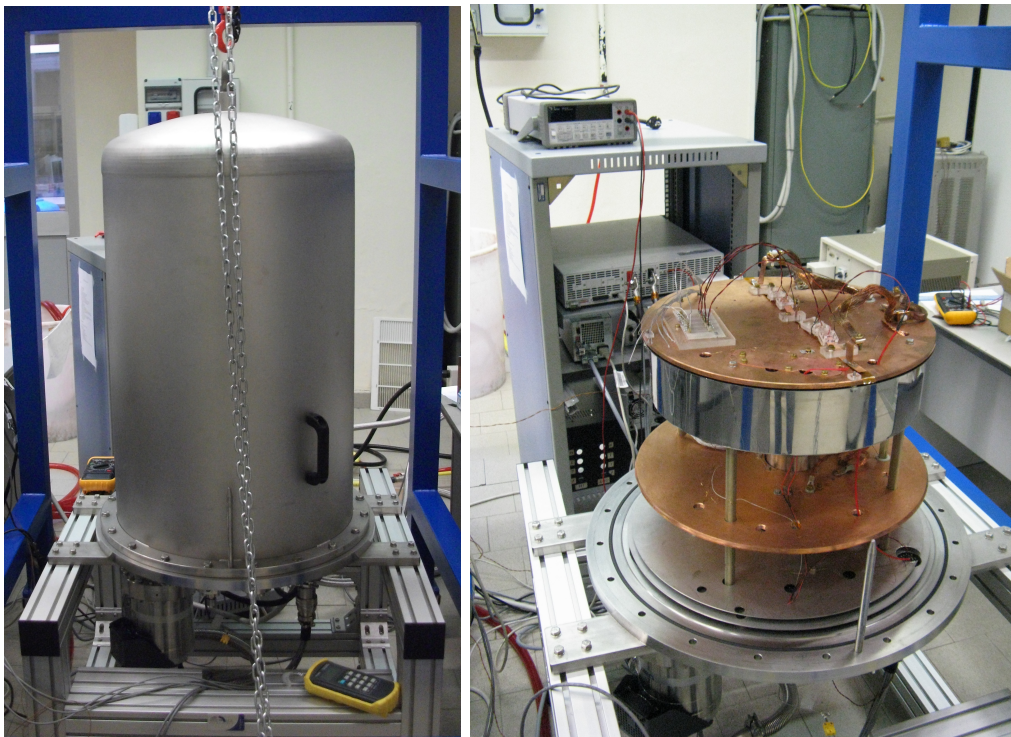
(a) *Photo of the cryostat used for the superconducting measurements.*

(b) *Internal view of the cryostat. The two copper stages as well as a Stabilizer Free YBCO sample are visible.*

Figure (2.1) *External and internal view of the cryostat used for superconducting measurements.*
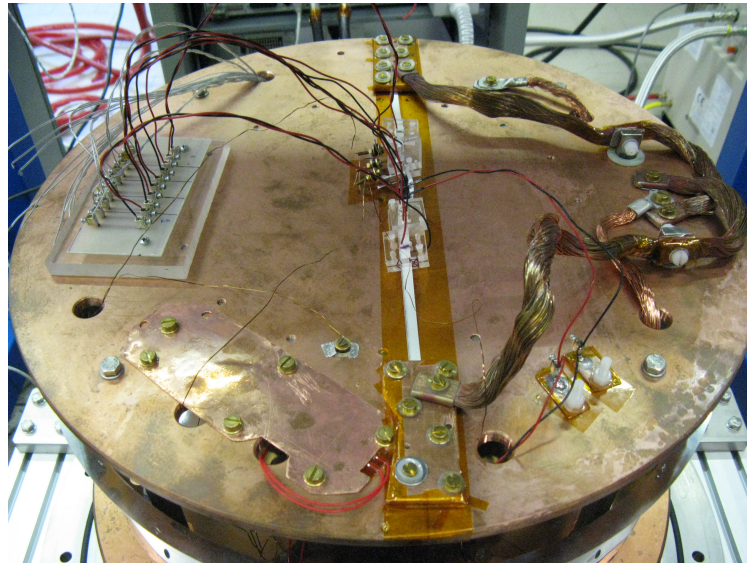
Figure (2.2) *Photo of a YBCO sample mounted on the second stage of the cryocooler.*

In Fig. (2.2) a photo of a Stabilizer Free YBCO sample instrumented and mounted on the cryostat is reported. From this picture all the equipment necessary to perform critical current and quench measurements are visible, in particular:

- two current leads, electrically isolated but thermally anchored to the copper plate;

- the voltage and temperature signals;

- the heater for the deposition of the heat inside the sample;

- two copper pieces used to press the ends of the tape to the cold plate, thus ensuring thermal anchoring.

Moreover, a Kapton Film Insulated Flexible Heater [11], whose design is visible in Fig. (2.3), is mounted on the second stage of the cryostat. The heat provided by this heater is controlled with a Lake Shore Cryotronics, Inc. Model 335 Cryogenic Temperature Controller [12]. This instrument, thanks to a controlled feedback loop temperature measurement, is able to maintain the 2nd stage copper temperature at a fixed value, thus allowing measurements to be performed different temperatures, from 5 to 90 K.

More details about each equipment summarized in this section will be reported later in this Chapter with focus on their mounting procedures.
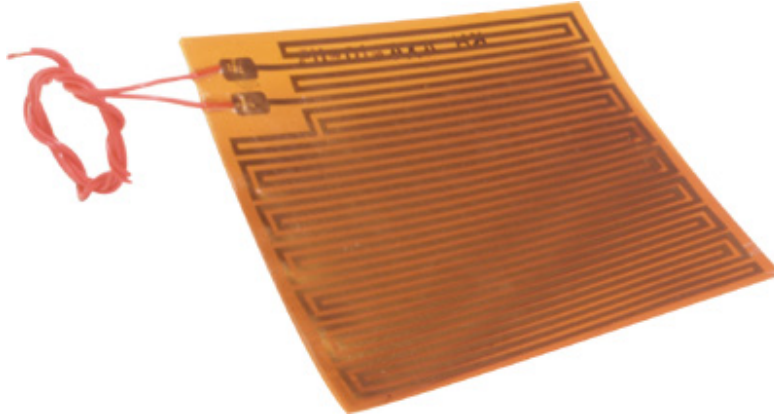
Figure (2.3) *Omega® Kapton Film Insulated Flexible Heater used to control the 2nd stage temperature and perform superconductivity measurements at different temperatures.*

2.2 CRYOCOOLER

The cryocooler is the device which provides the necessary refrigeration power to reach cryogenic temperatures. In our facility this machine, mounted under the stainless steel shields enclosed chamber, is a 4 K Gifford-McMahon regenerative heat exchanger RDK-408D [13], produced by Sumitomo Heavy Industries, Ltd.

The technical drawings of the selected device and a graph which shows the refrigeration heat power as a function of temperature for both stages are reported in Fig. (2.4). The nominal heat loads are about 34 W at 40 K from the 1st stage and 1 W at 4 K from the 2nd stage.

The regenerative coolers are characterized by the presence of a regenerative heat exchanger [8] in which the working fluid, gaseous helium, flows alternately cold and heated depending on the phase of the thermodynamic cycle. Therefore, the regenerative matrix must be able to store heat during the passage of the hot fluid, and subsequently to transfer it to the cold fluid recirculating in the opposite direction. This need of heat storage becomes a thermodynamic limit for this type of cycle, since the thermal capacity of all crystalline solids tends to zero as the temperature approaches absolute zero. To reach temperatures close to absolute zero with these devices, materials with a different heat storage mechanism, such as magnetic phase transitions, are necessary, for example erbium or gadolinium.

The cooling process of a Gifford-McMahon (GM) Cryocooler, whose cycle and scheme are shown in Fig. (2.5), can be described as follows:

1. the displacer is initially located at the bottom of the cylinder, the inlet valve is opened and the fluid starts to circulate in the regenerator, process $1 \rightarrow 2$.

2. During the process $2 \rightarrow 3$ the displacer is lifted up on top of the cylinder, this causes the movement of the gas, originally in the upper area of the expander, through the three-way valve until reaching the lower expander area. Since the volume of the gas being cooled in the regenerator decreases, the inlet valve remains open to maintain a constant pressure throughout the system.

3. The gas content in the lower part of the expander is expanded in the process $3 \rightarrow 4$ up to the initial pressure of the system by closing the inlet valve, redirecting the three-way valve, and opening the exhaust valve. During this expansion the gas temperature decreases.

4. The displacer moves downward in the process $4 \rightarrow 5$, forcing the residual gas in the bottom of the cylinder to exit and pass through the heat exchanger, where it absorbs heat from the region to be cooled.

5. Finally, in process $5 \rightarrow 1$, the gas is heated up to about room temperature by sending it back through the regenerator.

The problems due to the presence of impurities within the working fluid are mitigated by the presence of the regenerative matrix. The GM refrigerator requires a small motor for moving the displacer and it is characterized by low losses around the expander, since it works with a low compression coefficient.

The gaseous helium which flows inside the cryocooler requires in turn to be cooled after each thermodynamic cycle. A compressor unit CSW-71, produced once again by Sumitomo Heavy Industries Ltd., is connected to the cold head in order to maintain the temperature of the helium gas in the safe operating range. The cooling water supplied to the compressor must have a temperature between 4 and 28 °C for an effective cooling of the helium. In order not to waste large amounts of water (the achievement of the temperatures necessary for the superconducting measurements requires up to 10 hours in our facility) a chiller was inserted between the inlet water and the compressor unit. The chiller, reported together with the cold head and the compressor in Fig. (2.6), is an air-water heat exchanger which receives in input the hot water outlet from the compressor and cools it to the starting water temperature. Since the mass flow of the chiller differs from the compressor one, the design of a tank at ambient pressure was necessary in order to allow the two devices to work in series.
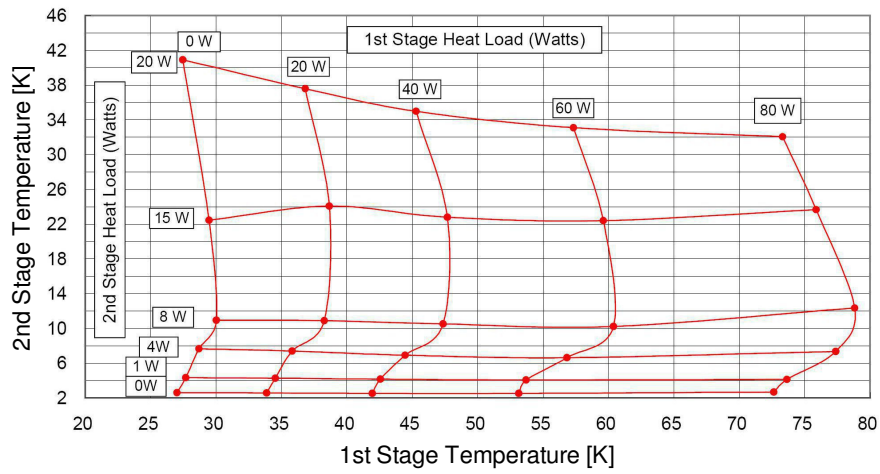
(a) *Graph of the heat power that can be extracted from the two stages of the cryocooler as a function of temperature.*
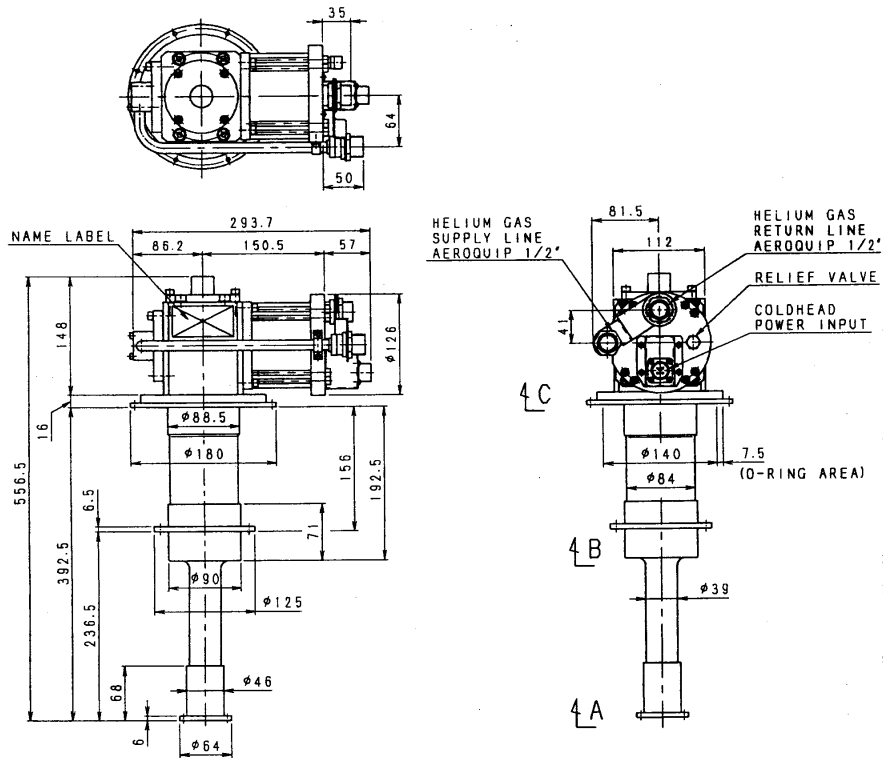
(b) *Outline view of cold head model RDK-408D.*

Figure (2.4) *Performances and technical drawing of the cryocooler mounted under the cryostat.*
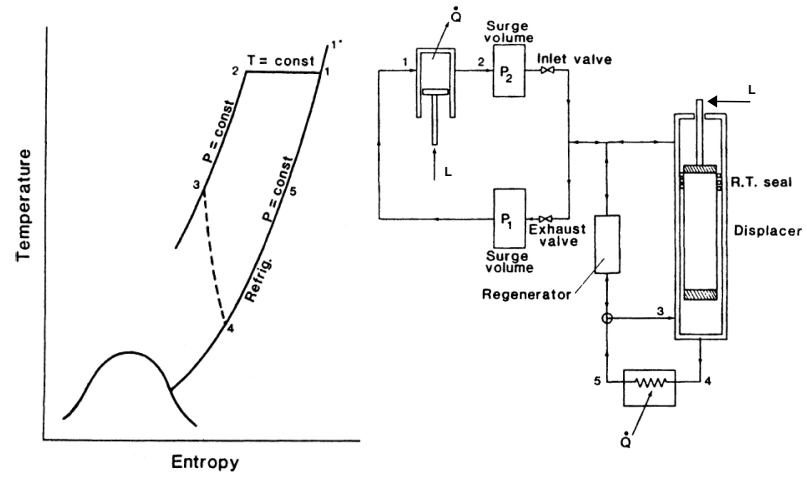
Figure (2.5) *Thermodynamic cycle and scheme of a Gifford-McMahon refrigrator system.*
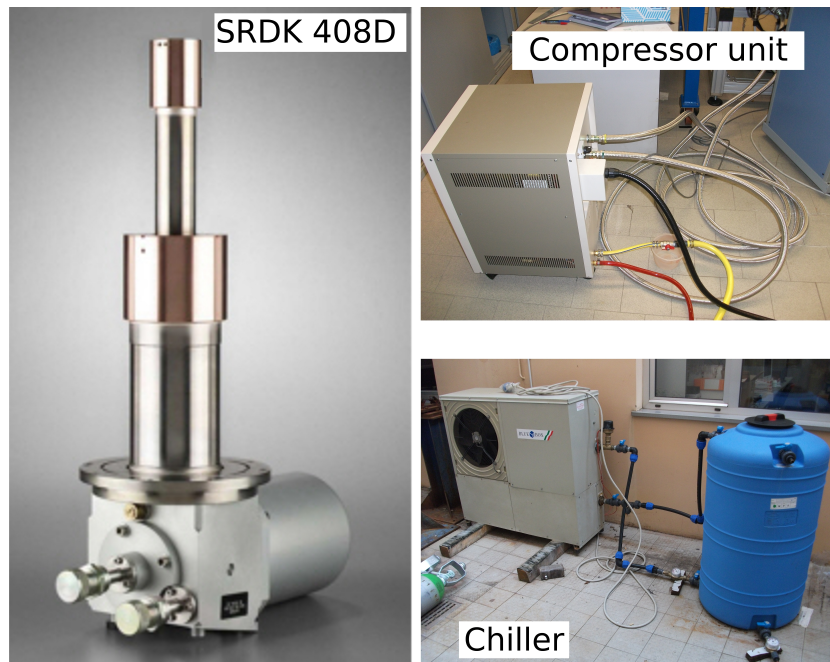
Figure (2.6) *Gifford-McMahon regenerative heat exchanger used to achieve cryogenic temperature inside the cryostat. The compressor unit CSW-71C and the Air-Water Chiller for the refrigeration of the He_{gas} cycle are also shown.*

2.3 VACUUM SYSTEM

The convective heat transfer is another mechanism of heat exchange to be reduced in order to approach temperatures close to absolute zero. A vacuum system is thus required to decrease the number of particles inside the cryostat. These particles in fact would be free to move inside the measurement chamber, transferring heat during each interaction with matter.

The vacuum level required for reaching the superconducting cryogenic temperatures is of about 10^{-6} mbar. In order to reach these values a rotary vane pump acts in series with a turbomolecular pump, both of them visible in Fig. (2.7). The rotary vane pump is a 2010 I pump produced by Adixen, characterized by a 10 m^3/h flow rate and by a nominal ultimate pressure of about $1.0 \cdot 10^{-3}$ mbar. The turbomolecular pump, produced by Adixen too, is an ATH 300 equipped with an ACT 200 controller able to reach the vacuum required thanks to the high speed reached by its rotor, that is 42000 rpm.

Moreover, the vacuum system includes a vacuum sensor, a Pfeiffer Vacuum Compact Cold Cathode Gauge, connected to a Single Gauge, Single-Channel Measurements and Control Unit to measure and monitor the vacuum level during the experiments.

Figure (2.7) *Photo of the vacuum system assembled. A rotary vane pump (white) and a turbomolecular pump (grey) act in series to ensure the vacuum level required.*

2.4 CURRENT LEADS

The operative current is fed into the samples by a Lambda Genesys™ GEN8-400 Single Phase Power Supply, able to supply up to 400 A on a load with a voltage drop up to 8 V.
The current leads are divided into two parts:

- the ambient temperature current leads, located outside the cryostat;

- the cryogenic current leads, located inside the cryostat.

The latter are again divided into two parts, in order to minimize the costs and the power introduced by heat conduction in the samples. Between the flange of the stainless steel chamber and the 1st stage of the cryostat, the cryogenic current leads are made of copper, while they are superconducting in the area between the 1st and the 2nd stage.

The design of the cables at ambient temperature is standard, the only requirement is a suitable conducting cross section in order to carry the maximum current, 400 A, without an excessive overheating due to Joule effect. A rubber insulated cable with a copper cross section of about 1.13 cm^2 was chosen to connect the power supply to the current leads outcoming from the cryostat.

While the normal conducting cryogenic current leads have been designed and mounted by the company which built the cryostat, the superconducting parts were missing and it was necessary to optimize, to mount and to test them. The thermodynamic optimization of these devices is based on the definition of the ratio between the length of the conductor and its conducting cross section, as reported in [14]. Several publications about the use of the HTS current leads inside a cryostat can be found in literature, for example [15] and [16].

To meet the requirement of maximum current with a minimum thermal conduction, within the available space, two BSCCO superconducting current leads manufactured by LOT-Quantum Design Srl were selected. In particular model CS050030, able to carry up to 500 A with a conductive heat leak of 145 mW per pair, was chosen. The characteristics of the available current leads are summarized in Fig. (2.9), while a photo of the whole cryogenic current leads circuit, mounted inside the measuring chamber, is reported in Fig. (2.8).

The superconducting current leads are a critical part of the power supply circuit and accurate care should be taken during their assembly. The ends of the current leads must be adequately thermally anchored, but electrically
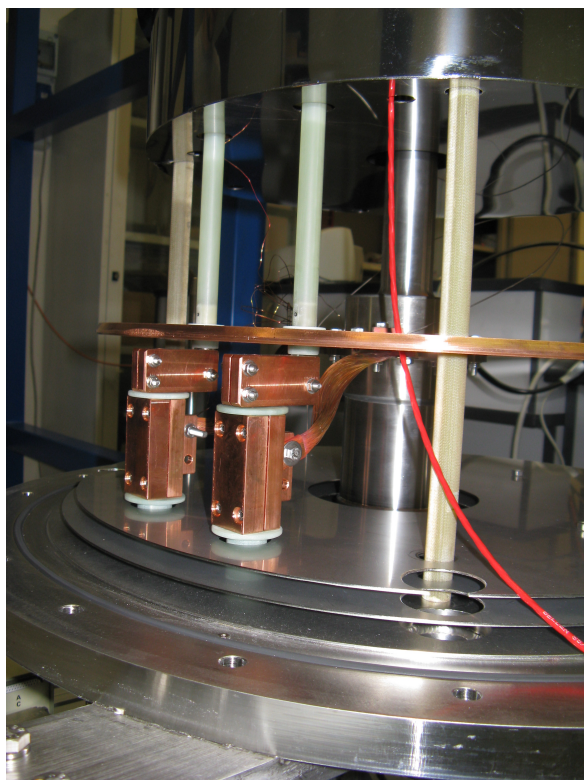
(a) *Photo of the current leads assembled inside the cryostat.*
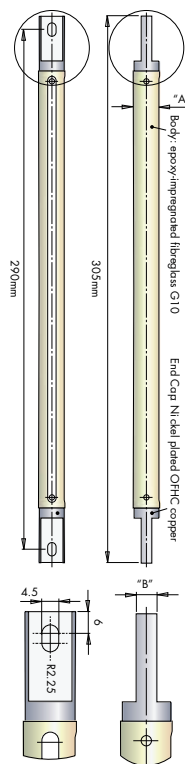
(b) *BSCCO superconducting current leads technical drawings.*

Figure (2.8) *Cryogenic current leads.*

Product	Body Diameter A		Dimension B		Operating Current at 64K	Conductive Heat Leak at 64K-4.2K (per pair)
	inches	mm	inches	mm		
CS010030	0.375	9.53	0.13	3.30	100A	32mW
CS025030	0.438	11.13	0.25	6.35	250A	76mW
CS050030	0.563	14.30	0.25	6.35	500A	145mW
CS100030	0.750	19.05	0.375	9.53	1000A	285mW
CS200030	1.00	25.40	0.438	11.13	2000A	480mW

Figure (2.9) *Superconducting BSCCO current leads characteristics.*

insulated, to both the copper plates, to control the temperature and ensure their operation in the superconducting regime.

Moreover, the ambient temperature current leads are immersed in liquid nitrogen in a tank designed in our laboratory, to minimize the heat introduced in the samples by conduction during measurements.

2.5 SAMPLE MOUNTING AND INSTUMENTATION

The mounting and instrumentations of the samples to characterize is a complicated and fine process. In particular great care must be taken in the sensors installation, not to damage the YBCO tapes during their assembly, and in the thermal anchoring to the 2nd stage of the cryostat.

As can be seen in Fig. (2.2) the thermal anchoring is achieved thanks to two pieces of copper (bus bars) which press the ends of the samples to the cold copper plate. However, the electrical insulation between the sample and the cooling machine must be guaranteed in order to avoid the flowing of the current in the metal parts of the cryostat. For this reason two layers of Kapton tape are inserted under the sample to be measured. The two bus bars are pressed on the cold copper plate with a series of through screws, tightened with a torque of 5.5 N·m with a torque wrench. The scheme of the thermal anchoring developed and used for sample mounting is reported in Fig. (2.10). The six stainless steel screws are surrounded by insulating heat shrink sheaths in order to assure the electrical insulation.
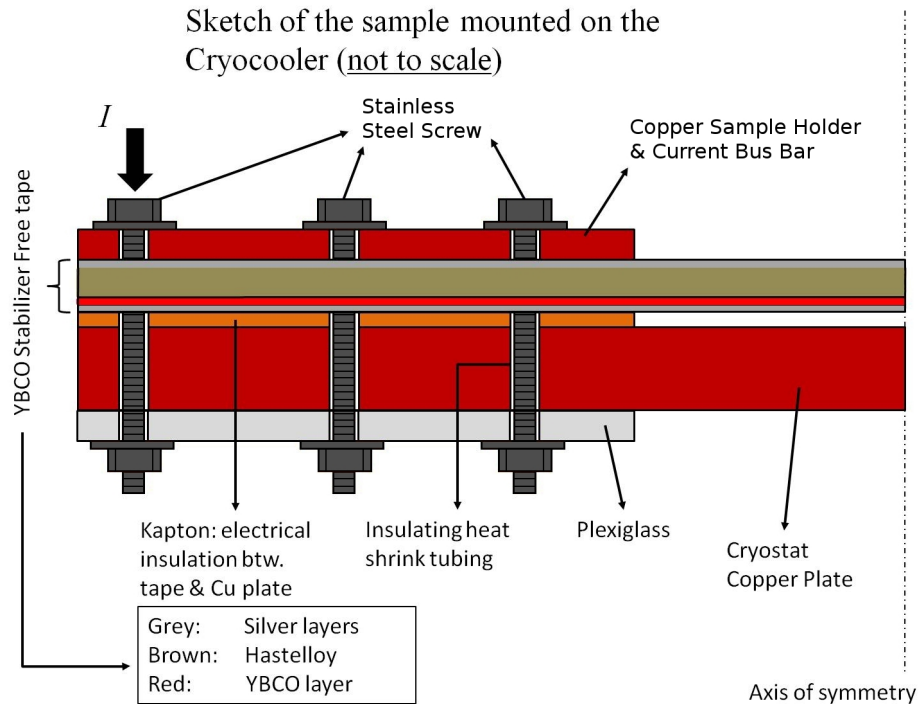
Figure (2.10)   *Sketch of the thermal anchoring of a YBCO CC tape on the 2nd stage of the cryostat.*

Figure (2.11) *Thermal anchoring improvement with different samples and mounting procedure.*

The improvements in thermal connection obtained with this anchoring method appear clear analyzing the graph of Fig. (2.11). The red and the green curves refer to the first measurements made to test the facility. In the first case an MgB$_2$ coil was simply posed on the 2nd Stage of the cryostat without any tightening; the temperature decrease monotonically but the samples was not able to cool down under 200 K. In order to improve the thermal contact between the coil and the cold copper plate, the samples was then tighten with a screw and an Indium foil was inserted in the contact area. The temperature decreases to a value slightly higher than 100 K, value not enough low to reach the superconducting transition. The same mounting procedure just described was applied to an YBCO coated conductor (CC) tape, whose temperature once again decreases low to an almost stationary temperature of about 100 K. However, with the introduction of the torque control the YBCO CC tape reaches a maximum temperature lower than 50 K. The last two measurements clearly indicate that a control on the tightening is necessary in order to reach the temperature values required, below 92 K for the YBCO tape and below 39 K for the MgB$_2$. Therefore, a torque
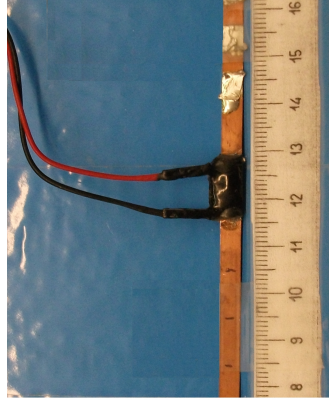
(a) *NiCr heater attached on a YBCO CC tape.*
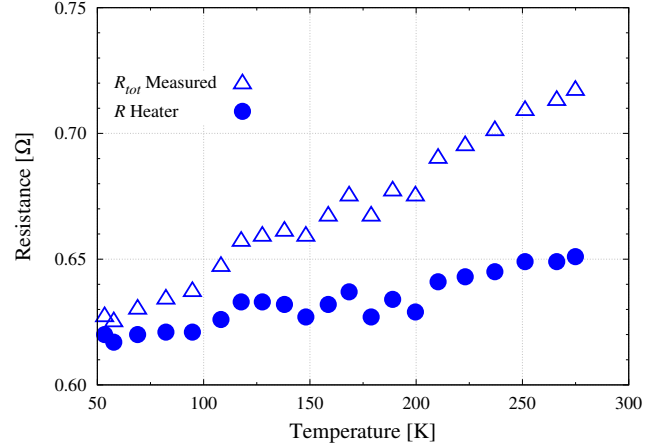
(b) *Resistance measured on the heater, including its copper wires, and heater resistance estimated as a function of temperature.*

Figure (2.12) *Heater for the deposition of heat power into the sample.*

wrench is necessary to measure the torque and to guarantee a clamp capable of withstanding also at very low temperature.

A W-shaped heater, manufacture in situ with a NiCr wire, is attached to the YBCO tape with an epoxy resin called Stycast® 2850FT, as can be seen in Fig. (2.12a). Stycast® is the most commonly used nonconductive epoxy resin system for cryogenic use. Its primary use is for vacuum feedthroughs and permanent thermal anchors, thanks to its ability to conduct heat (thermal conductivity equal to 1.25 W/m · K) but to be both an electrical insulator. Aim of the heater is the deposition of heat power inside the sample to simulate possible disturbances and characterize the behaviour of the superconductors during the transition to the normal conducting state. The values of the resistance which maximizes the heat deposited in the tape is computed with the maximum power transfer theorem. The optimal value is therefore equal to the total resistance of the wires which connects the heater to the voltage power supply, thus of about 0.7 Ω. However, this resistance varies with temperature, as reported in Fig. (2.12b), and it has to be monitored during measurements in order to have a better estimation of the heat produced during quench measurements.

Finally the voltage taps and the temperature sensors should be attached to the samples for recording the voltages and temperatures evolution during critical current and quench measurements. More details about their mounting procedures will be given in the following subsections.

2.5.1 Voltage Measurements

The voltage measurements circuit, as well as the current leads one, is composed of an ambient temperature part and a cryogenic part. The wires located outside the cryostat are standard copper cables rubber insulated, twisted with each other in order to reduce the electromagnetic noise due to self and mutual inductances. One of the ends of the measurement wires is connected to a NI PCI-6281 DAQ acquisition system, while the other one is connected to the signals feedthrough, as visible in Fig. (2.13a).

Inside the cryostat the wires are made of stainless steel in order to reduce the heat introduced into the vacuum environment by thermal conduction. This material is in fact characterized by a thermal conductivity up to three orders of magnitude lower than that of copper. However, for the same reason the soldering of this material on the copper layer of the YBCO tape is not possible without damaging the sample. A printed circuit board, manufactured in our laboratory, was mounted on the 2nd stage for this reason. As can be seen in Fig. (2.13b) the stainless steel wires are connected to the terminals on the left, while 15 cm long copper wires are used at the end of the board. The final copper wires are soldered to the samples with a low melting point solder, named Ostalloy®, an eutectic alloy of bismuth, tin, lead, and cad-
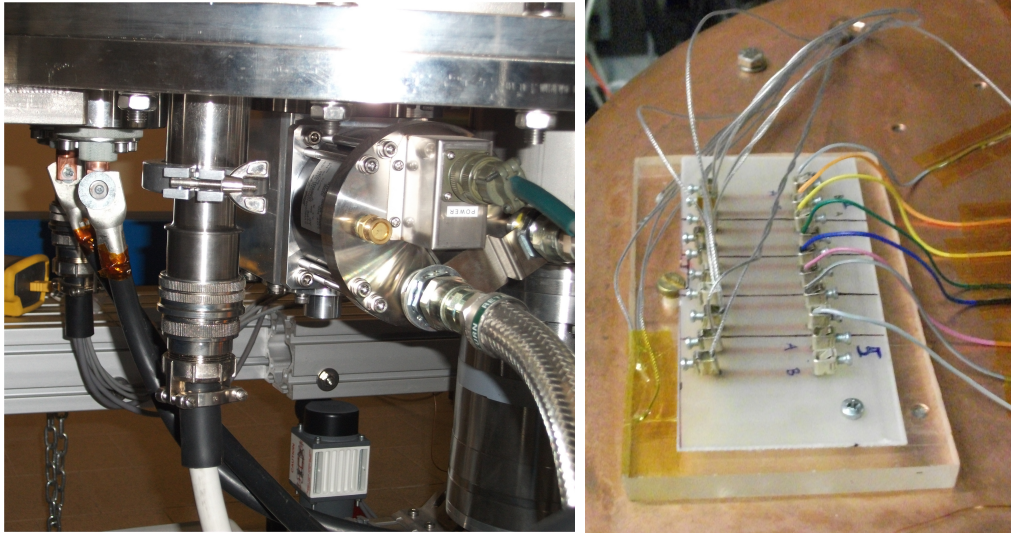
(a) *Photo of the devices located under the cryostat. From the left the current leads, the signal feedthrough and the cryocooler are visible.*

(b) *Printed circuit board connecting the stainless steel and the final copper wires.*

Figure (2.13) *Details of the voltage measurements circuit.*
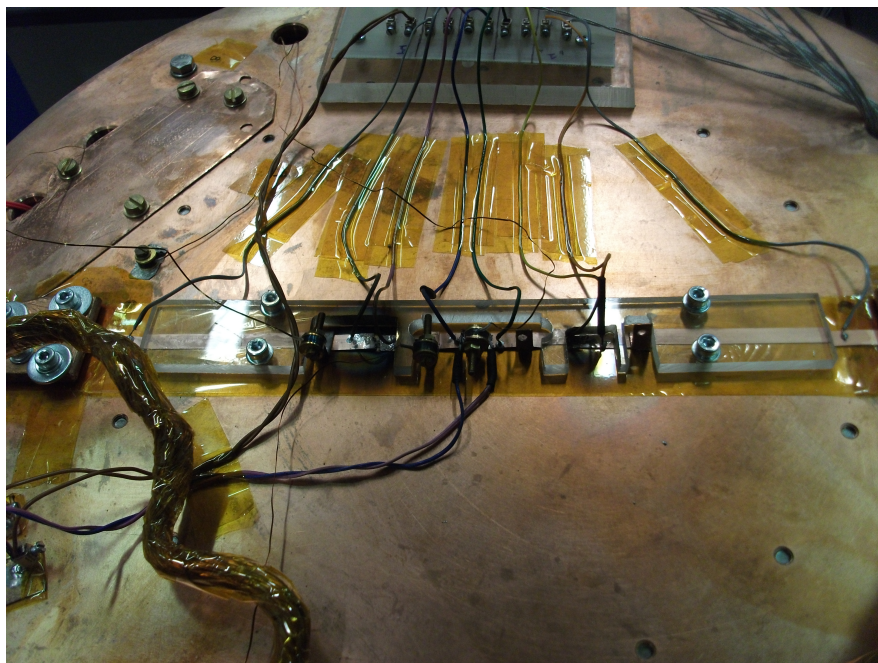
Figure (2.14) *YBCO CC sample mounted and instrumented.*

mium with a melting point of 343.16 K [17]. The low temperature melting point is crucial not to damage the thin YBCO tapes, usually only 0.1 mm thick, thus solving the welding problems.

All the wires installed inside the measurement chamber are thermally anchored to both the cryostat stages gluing them to the copper plates, once again to reduce the heat introduced into the samples and to achieve lower temperatures.

2.5.2 Temperature Measurements

The temperatures inside the vacuum environment are measured with DT-670A-CU silicon diodes, whose specification are reported in [18]. In particular one sensor is located on the second stage of the cryostat and it is connected to the Temperature Controller to set the cold plate temperature to the desired value. The remaining three diodes are used to monitor and record the temperatures evolution on the samples during measurements.

For this purpose three thin copper strips are soldered on the YBCO tape in different positions, with the same procedure followed for the voltage taps welding. The diodes are then mounted on these strips with #4-40 screws, thanks to the gold-plated copper mounting bobbin supplied with the sensor.

The lead wires of the temperature sensors are connected to a Model 211 Temperature Monitor [19] manufactured by Lake Shore Cryotronics, Inc. to measure temperatures from 1.4 K to 800 K in a high vacuum and high magnetic field environment. These sensors are easy to install and very accurate throughout the whole temperature range of interest, ± 0.5 K with no calibration needs, but their thermal response is quite slow for single tape measurements and their replacement with K-type thermocouples is being evaluated.

Fig. (2.14) shows the final YBCO CC tape mounting configuration. The voltage taps, the temperature diodes, as well as the NiCr heater used to induce the quench are visible. The sample is held in place with a machined PMMA Thermoplastic piece which makes the sensors arrangement possible and prevents sample movements.

2.6 Superconducting Measurements Software

Every instrument necessary to the experiments, a current generator, a vacuum sensor, a power supply to generate pulses in the heater resistor as well as the data acquisition system, is connected to a PC which controls them and records all data. The PC is able to perform a real time control on all the different devices via a LabVIEW code [20] completely developed during my research period.

The same software is able to fulfill critical current or quench measurements thanks to a simple panel interface, which allows the choice of the desired measurements type.

The software interface, reported in Fig. (2.16), is divided into four main areas. In the left section of the panel a frame for the measurement type choice is present together with the NI PCI-6981 controls. This area allows the selection of the desired voltages channels to be measured, called DAQmx Physical Channels, which are connected to the voltage taps soldered on the YBCO sample inside the cryostat. Moreover, the channels dedicated to the measurements of the operative current and of the heater voltage pulse fed into the tape are present. The operative current is measured by a current clamp located outside the cryostat on the ambient temperature current leads, while the heater is driven by the circuit reported below. A DC power supply is connected to the heater and its voltage drop is recorded during the heat pulse by the *Heater Voltage Physical Channel*. The current fed into the heater is measured with a current shunt which returns a voltage signal of 1 mV/1 A connected to the *Heater Current Physical Channel*.
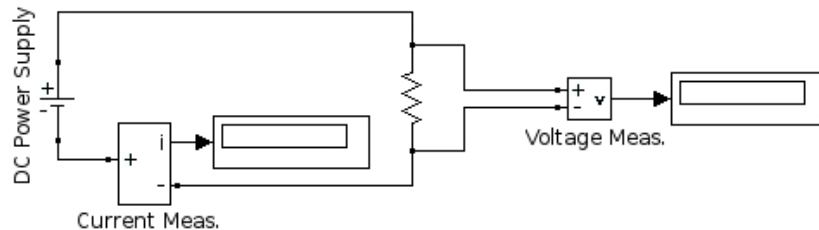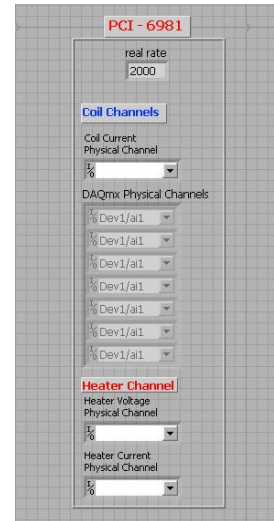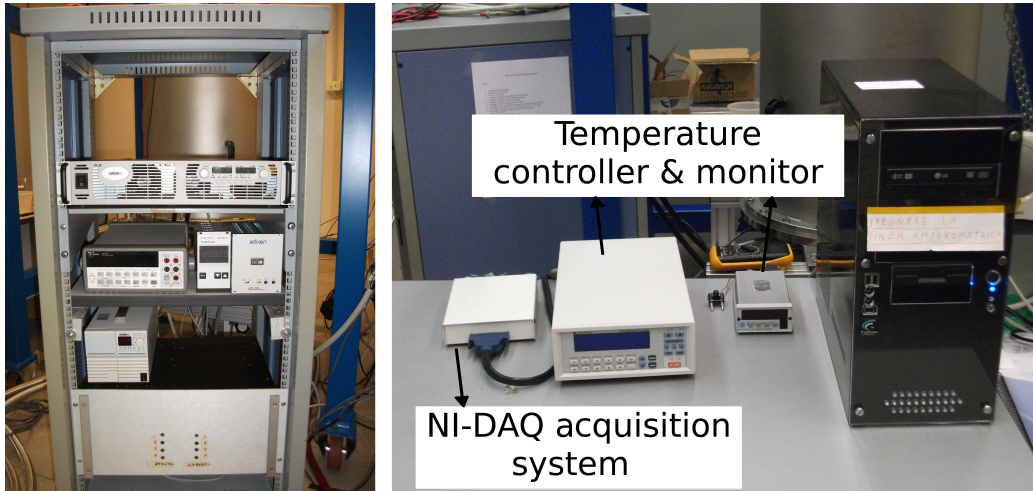
Figure (2.15)   *Instruments and data acquisition system used for supercon-ductors characterization.*
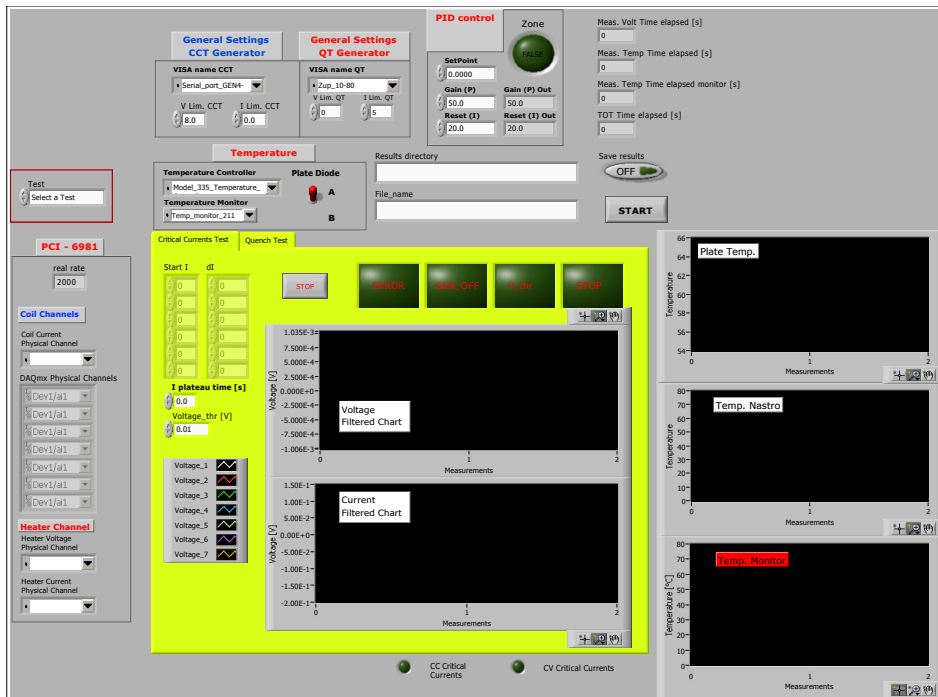
Figure (2.16)   *Sketch of the Superconducting Measurements Software front panel.*

On the top of the front panel the sections concerning the communication with the devices to be control is located. In the frames dedicated to the generators the voltage and current limit controls could be setted. These parameters allow the control of the generator in the desired mode: current mode for the operating current power supply and voltage mode for the pulse voltage power supply connected to the heater resistor.
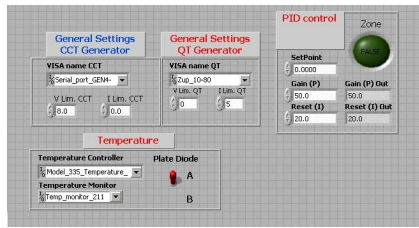
Below, the frame called Temperature allows the communication with the Temperature Monitor and the selection of the diode which measures the cold plate temperature. At last, on the right, all the parameters necessary to set the Temperature Controller are located. The *SetPoint* refers to the temperature value to be reached by the cryostat 2nd stage, while *Gain* and *Reset* are the PID controller parameters. The PID controller is the control loop feedback mechanism which drives the heat to be fed in the heater mounted on the copper plate visible in Fig. (2.2).

In the third part of the panel the definition of the path and of the name of the measurement file is possible. The start bottom triggers the data acquisition procedure, before its activation the plate temperature signal could be checked but nor current nor heat pulse would be fed into the sample and no voltage would be acquired.
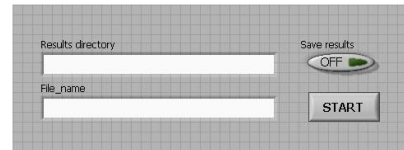
Finally the measurement begins and the voltages and temperatures on the sample are displayed in real time in the dedicated graphs. Since the voltage signals are noisy, they are filtered with a smoothing moving average filter and their displaying on the front panel would not stat before having subtracted the offset values at zero current. However, this signal processing is performed only for a visual check of the signals and all the recorded data are saved in their raw form and reprocessed with a dedicated post-processor software after the end of the measurements campaign.

2.6.1 Critical Current Measurements

During a critical current measurement the operating current is incremented by steps which are long enough to reach the steady state. The desired current profile is obtained thanks to two arrays to be defined in the critical current test tab, located in the middle of the front panel of the LabVIEW interface, reported in Fig. (2.17). The array called *Start I* defines the current values at each step, after the first zero current step, while the array called *dI* refers to the current increase between the actual current value and the following one. The current is then maintained constant during a user defined time window, usually 3 to 5 s long.

A typical voltage evolution during a critical current measurement is reported in Fig. (2.18). The current supply is switched off and the measurement ends when a safe value called *Voltage_{thr}*, defined by the operator, is reached. This quench protection system based on maximum voltage detection is necessary to protect the samples from damaging during fast quenches. Furthermore, a STOP button, which forces the shutdown of the current generator, is located in the front panel to provide an alternative protection method in case of problems in the measurement of the voltage signals.
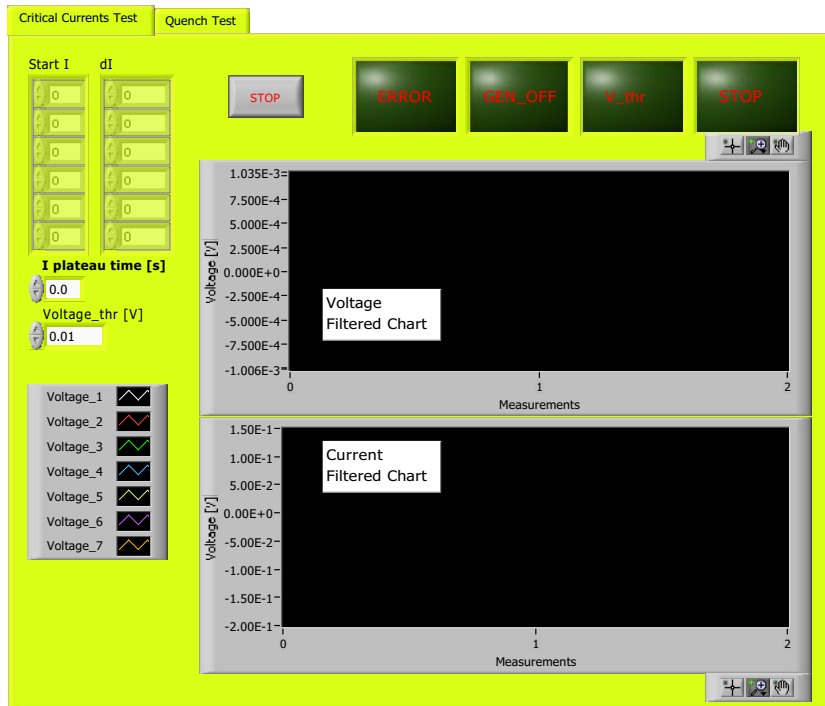
Figure (2.17)   *Critical current measurement LabVIEW interface tab.*
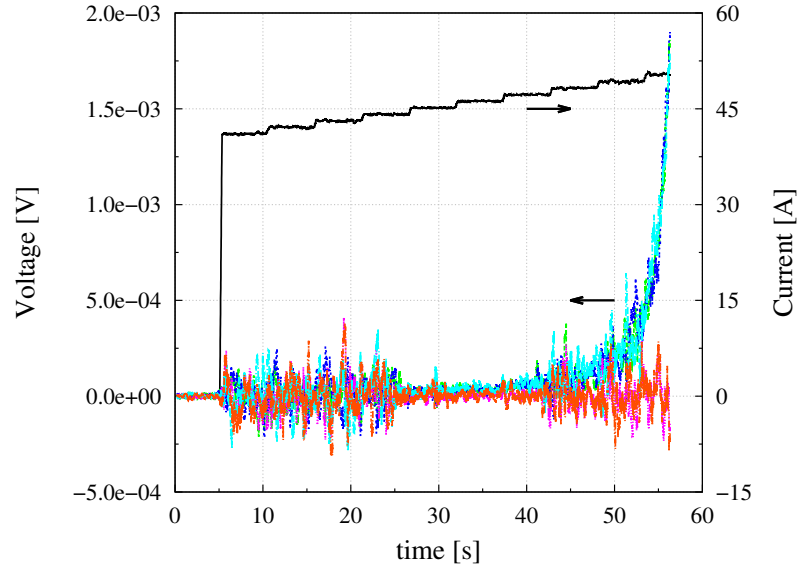
Figure (2.18) *Typical evolution of voltages during a critical current measurement.*

Once the measurement is finished the raw data are processed by a GNU Octave code [21]. At first the voltage signals are filtered through a moving average, then the code computes a single value for each current step performing the average value on a user defined time windows. The offset, corresponding to the value on the first zero current step, is subtracted to each voltage signal. The critical current is then computed with a linear interpolation between the voltage data points just below and just above the critical voltage:

$$V_0 = E_0 \cdot l$$

Fig. (2.19a) summarizes the procedure described: the voltage filtered trace is reported in blue while the red dots refers to the voltages average values on each current step. The critical current computed is then compared with the one obtained by the fit of the critical current density and of the *n-value* of the power law:

$$E = E_0(J/J_c)^n$$

(a) *Post-processed voltage trace.*

(b) *E-I characteristic fitting.*
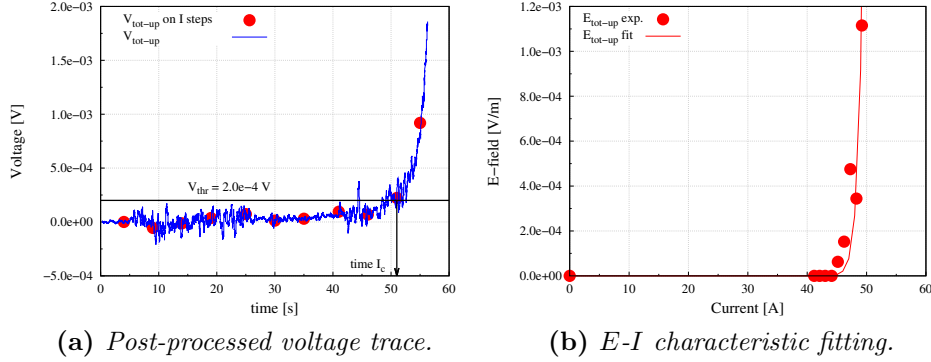
Figure (2.19) *Procedures for the computation of the critical current.*

2.6.2 Quench Measurements

The quench measurements involve the control of the pulse voltage generator to deposit heat inside the sample, thus inducing the transition to the normal conducting state, while the transport current is kept constant.

The quench measurement LabVIEW interface tab is similar to the critical current one with the introduction of the pulse parameters, which replace the current profile settings. As reported in Fig. (2.20) the voltage pulse is defined by three values:

- the Voltage Pulse;

- the Pulse Duration;

- the Pulse Wait Time.

The first refers to the voltage power supply output, which in turns drive the current fed into the heater as a function of the total load. The second value is the time duration of the pulses, usually 0.25 to 0.5 s long, and the Pulse Wait Time defines how long after the start of the measurement the pulse triggers.

When the external heat propagates from the NiCr heater to the YBCO CC tape, parts of the sample under the resistor may overcome the critical temperature at the fixed operating current. These sections undergo the transition from the superconducting to the normal state and measurable voltages start to rise. However, if the cooling power is high enough to extract all the internal heat from the tape, due to normal sections Joule effect, the sample could recover the superconducting state and the voltages return not to be measurable. In this case the normal zone is not able to propagate through
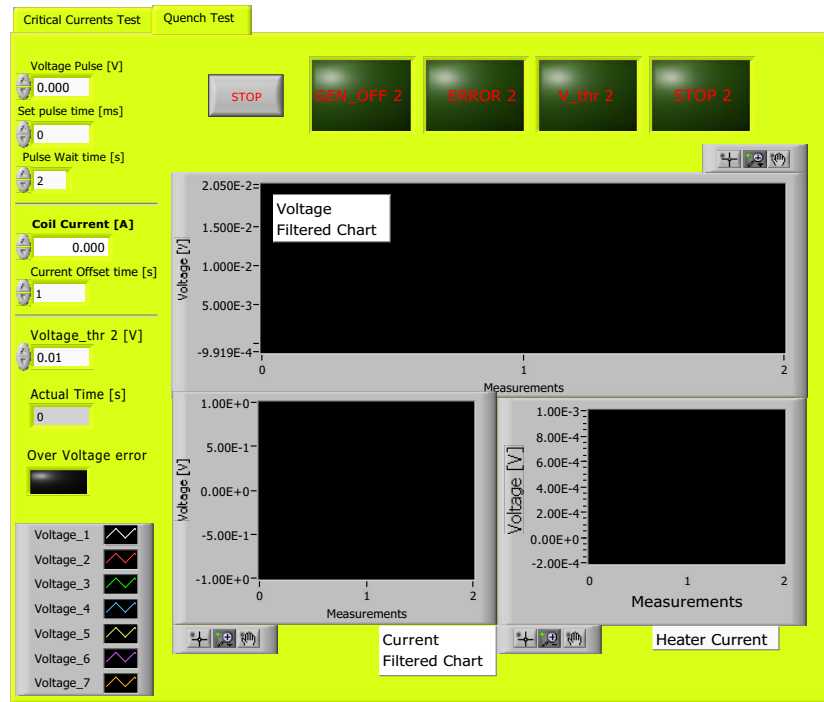
Figure (2.20) *Quench measurement LabVIEW interface tab.*

the tape, the transition is not irreversible, and the phenomena is called *Recovery*. A typical recovery voltage and temperature measurement is reported in Fig. (2.21).

If the cooling power is not sufficient, the sample is not able to drain the internal power produced and the temperature starts to rise monotonically until reaching possibly dangerous values, which may compromise the sample integrity and merge it. To avoid the excessive rise of the temperature the quench protection system is activated, as described previously, and the operative current is switched off. The voltage and temperature evolution of a *Quench* run is reported in Fig. (2.22).

The measurements are usually performed increasing the energy deposited into the sample until the quench is reached, or alternatively increasing the operating current at fixed energy. The definition of the minimum energy which triggers the quench, described in grater detail in the following Chapters, is one of the main parameters characterizing the superconducting wires and tapes as far as the thermal stability is concerned.
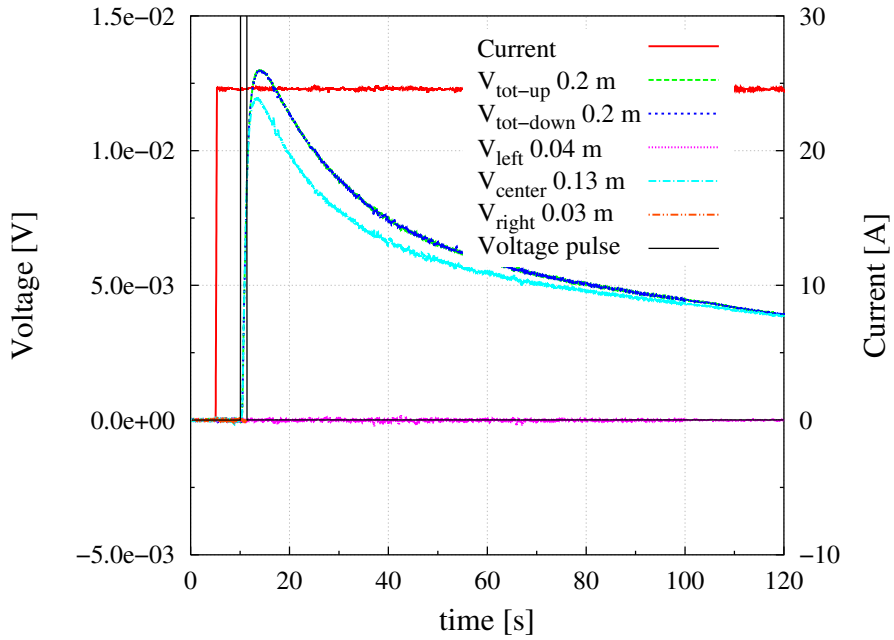
(a) *Voltages evolutions during a recovery.*
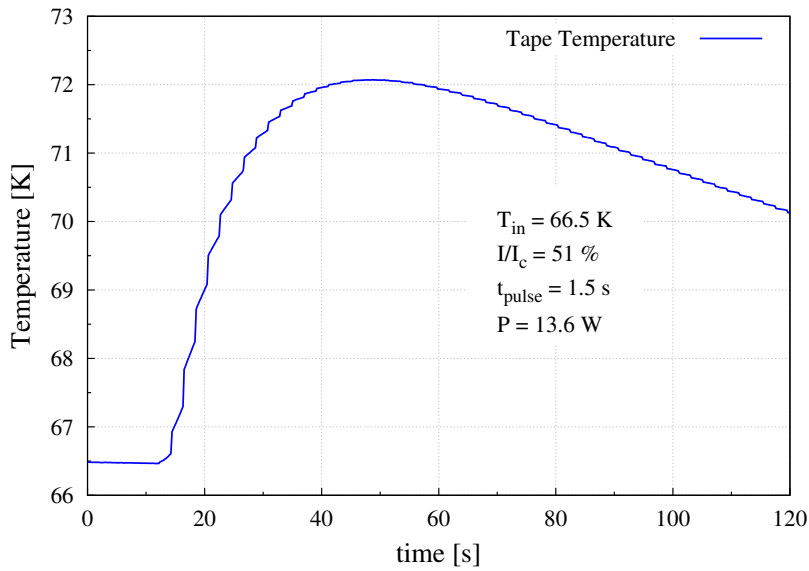
(b) *Temperature evolution during a recovery.*

Figure (2.21) *Typical recovery measurement evolution.*
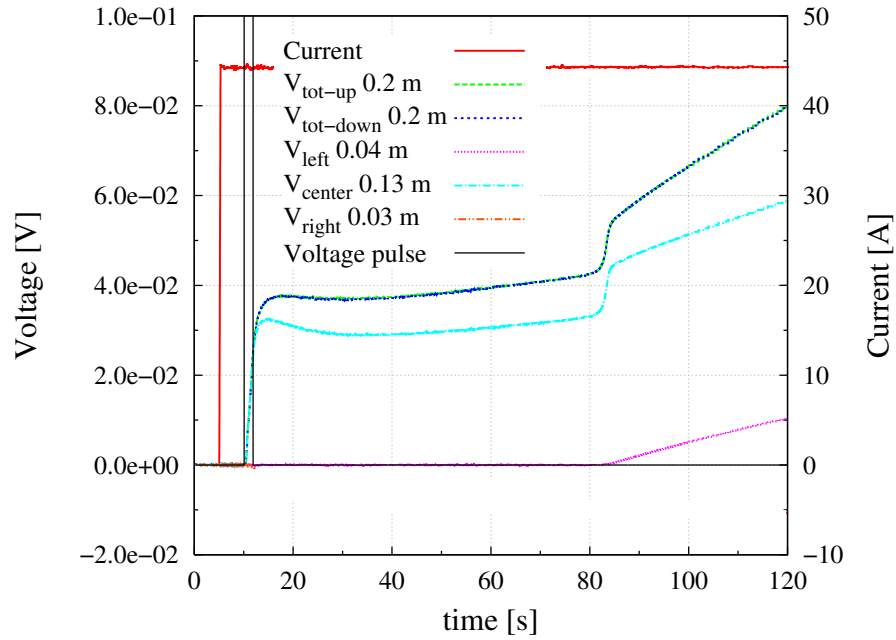
(a) *Voltages evolutions during a quench.*
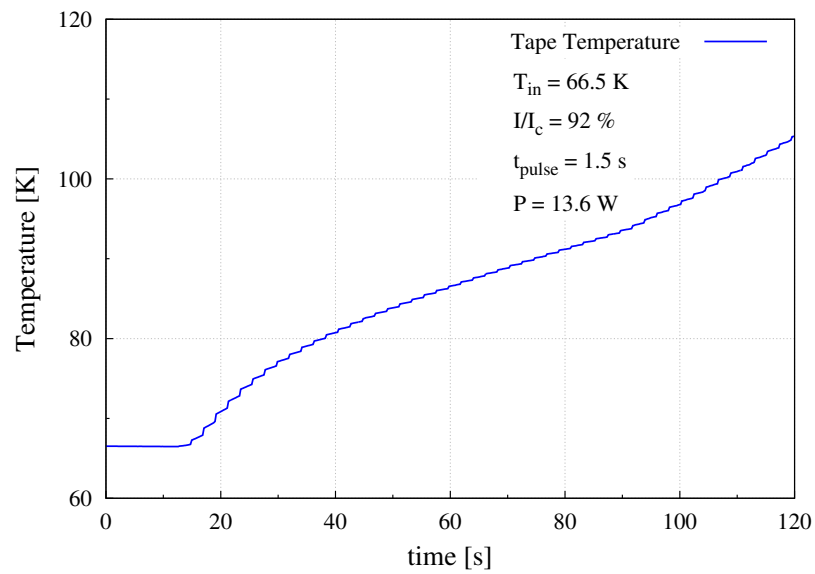
(b) *Temperature evolutions during a quench.*

Figure (2.22)   *Typical quench measurement evolution.*

Chapter 3

A 2D Anisotropic Model for YBCO Coated Conductors

The quench characteristics of second generation (2 G) YBCO Coated Conductor (CC) tapes are of fundamental importance for the design and safe operation of superconducting cables and magnets based on this material. Their ability to transport high current densities at high temperature, up to 77 K, and at very high fields, over 20 T, together with the increasing knowledge in their manufacturing [22, 23], which is reducing their cost, are pushing the use of this innovative material in numerous system applications, from high field magnets for research to motors and generators as well as for cables.

The YBCO CC is composed of different layers. A cross section of a tape manufactured by SuperPower® inc.[24] is reported, not to scale, in Fig. (3.1). The superconducting layer, usually 1 μm thick, is deposited on a resistive one called buffer layer, which facilitates its proper orientation. On the bottom of the buffer layer a substrate material is introduced to provide mechanical support. Best materials for this function are NiW, stainless steel and Hastelloy® C-276 [25]. On top of the YBCO layer and on the bottom of the substrate two silver layers, 2 μm thick, are soldered with particular care [10, 26] in order to provide electrical contacts. The tape in this configuration is called Stabilizer Free. Depending on the function of the tape the Stabilizer Free configuration should be enclosed by two copper layers, 50 or 100 μm thick, called Stabilizer layers which increase the ability to transport current in the normal state. Stabilizer Free tapes are preferred in applications which requires low void fraction and small dimension as for Fault Current Limiter (FCL) and current leads. Stabilized tapes are used where the most important issue is stability as in the case of cables, coils and magnets, transformers and
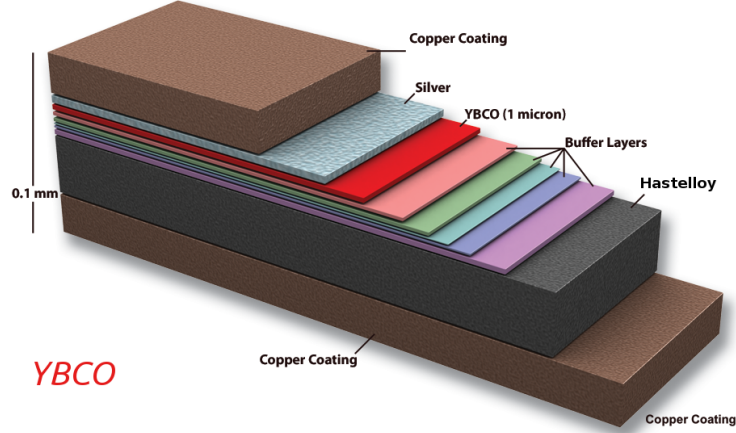
Figure (3.1)   *Exploded view of an YBCO tape (not to scale).*

rotating machinery [27].

The thermal properties of the materials which compose the YBCO CC lead to higher temperature margins and minimum quench energies (MQE) with respect to more widely used low temperature superconductors (LTS) like NbTi and Nb$_3$Sn [28]. This behaviour is due to the very high specific heat of the YBCO tapes in the high operating temperature conditions (60 - 77 K). The MQE is in fact proportional to the specific heat according to the following formula:

$$MQE \propto c_p \cdot \sqrt{k/\rho} \qquad (3.1)$$

where ρ is the electrical resistivity, c_p is the specific heat at constant pressure and k is the thermal conductivity. However, on the other side, the high specific heat causes a reduction of the normal-zone propagation velocity ($NZPV$), which is inversely proportional to it:

$$NZPV \propto \frac{\sqrt{k/\rho}}{c_p} \qquad (3.2)$$

Stability and protection of the superconductor are therefore in contrast, the higher the first the lower the second and vice versa.

An accurate study of the quench behaviour is mandatory for a better understanding and for a more efficient use of the YBCO CC. Their electromagnetic and thermal characterization is of fundamental importance for the design and safety use of cables and magnets manufactured with this ceramic superconducting material.

A 2D FEM numerical quench model, in the COMSOL Multiphysics®
environment, was developed for this purpose. Many approaches have been
already developed for modelling quench behaviour of CC tapes including ana-
lytical equations [29, 30], equivalent electric circuits with lumped parameters,
1D and 2D homogenized models [31, 32, 33] and 3D models [34, 35, 36, 37, 38].
One of the most difficult issues in the modelling of the YBCO tapes with fi-
nite element method is the very high aspect ratio value, 10^4 considering a
10 cm long YBCO layer 1 μm height. In the model developed the problem of
the high aspect ratio of the tape is tackled by multiplying the tape thickness
by a constant factor and then compensating the heat and electrical balance
equations by introducing material anisotropy. The FEM model is validated
by comparison with experimental data and with a 1D quench model based
on a non-linear electric circuit coupled to a thermal model of the tape.

Section (3.1) presents a detailed explanation of the model applied to the
study of a single YBCO CC tape, in Section (3.2) the material properties
of the materials which usually compose the superconducting tapes are intro-
duced while in Section (3.3) a convergence study and the mesh type selected
are reported. Finally Section (3.4) deals with the extension of the model for
the study of coils and windings.

3.1 Tape Model Description

The 2D FEM model developed is a thermo-electric model which solves the differential heat balance Eq. (3.3) strongly coupled with the stationary electrodynamics equations Eq. (3.4):

$$\rho_i c_{p_i} \frac{\partial T}{\partial t} - \boldsymbol{\nabla} \cdot \left(k_i(T) \boldsymbol{\nabla} T \right) = Q \tag{3.3}$$

$$\boldsymbol{\nabla} \cdot \left(-\sigma_i\left(T, \left| \mathbf{E} \right| \right) \boldsymbol{\nabla} V \right) = 0 \tag{3.4a}$$

$$\mathbf{E} = -\boldsymbol{\nabla} V \tag{3.4b}$$

$$\mathbf{J} = \sigma_i\left(T, \left| \mathbf{E} \right| \right) \mathbf{E} \tag{3.4c}$$

where T [K] is the absolute temperature, ρ [kg/m^3] is the mass density, c_p [J/kg·K] is the specific heat, k [W/m·K] is the thermal conductivity, Q [W/m^3] is the Joule heating, σ [S/m] is the electric conductivity, E [V/m] is the electric field, V [V] the electric potential and J [A/m^2] is the current density. Every material property has a subscript i which refers to the different layers that compose the YBCO tape: $i \in \{$Cu, Ag, (NiW, Hastelloy C-276® or stainless steel), YBCO$\}$. Eq. (3.3) and Eq. (3.4a) are implemented in the COMSOL environment as a Coefficient Form PDE [39].

The superconducting behaviour of the YBCO tape is introduced with the non-linear power law:

$$\left| \mathbf{E} \right| = E_0 \left(\frac{\left| \mathbf{J} \right|}{J_c(B,T)} \right)^n \tag{3.5}$$

where E_0 is the critical electric filed equal to 10^{-4} V/m, n is the E-J power law n-value, B is the magnetic flux density and J_c is the critical current density calculated with the parametrization fitting law below [40]:

$$
\begin{aligned}
J_c(B,T) =& \frac{A}{B + \epsilon} \left[B_{irr_0} \left(1 - \frac{T}{T_c} \right)^\alpha \right]^\beta \left[\frac{B + \epsilon}{B_{irr_0}(1 - T/T_c)^\alpha} \right]^p \cdot \\
& \cdot \left[1 - \frac{B + \epsilon}{B_{irr_0}(1 - T/T_c)^\alpha} \right]^q
\end{aligned}
\tag{3.6}
$$

where ϵ is a fitting parameter used to extend the validity of the Eq. (3.6) to low magnetic fields, with reference to the experimental value at 77 K and self field. The lower boundary value at which the usual fitting formula is valid is in fact equal to 1 T. The complete set of parameters used in Eq. (3.6)

is reported in Table (3.1); a plot of the critical current as a function of temperature at different external magnetic fields is reported in Fig. (3.2).

The strong coupling between the thermal and the electromagnetic model is realized through temperature-dependent electrical properties of materials, in particular of the electrical conductivity and of the critical current, and the introduction in the thermal model of the Joule power calculated with the electromagnetic model:

$$Q = \mathbf{J}\big(T, \big|\mathbf{E}\big|\big) \cdot \mathbf{E} = \sigma\big(T, \big|\mathbf{E}\big|\big)\boldsymbol{\nabla}V \cdot \boldsymbol{\nabla}V \tag{3.7}$$
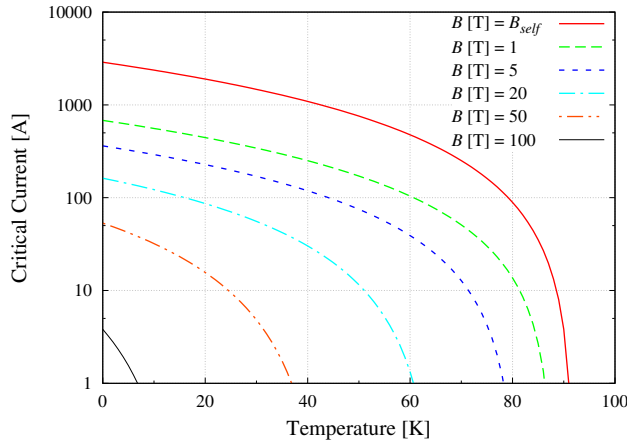
Figure (3.2) *Critical current as a function of temperature at different external magnetic flux densities.*

Parameter	Value
A [N/(m$^3\cdot$ T$^\beta$)]	5.2254e8
T_c [K]	92
B_{irr_0} [T]	132.5
p	0.653
q	2.568
α	1.5
β	1.789
ϵ	0.0168

Table (3.1) *Fitting parameters for the critical current of YBCO.*

3.1.1 Thermal Model

The modelling of the YBCO tape with a traditional FEM approach results challenging and time consuming due to the high aspect ratio of the tape. In the anisotropic model developed this computational problem is solved with the implementation of a rescaling of the y-coordinate, that is the height of the layers which compose the tape. The tape thickness is therefore multiplied by a constant factor N, usually equal to 50, in order to reduce the aspect ratio; more details are reported in Section (3.3). The heat and the electrical balance equations, respectively Eq. (3.3) and Eq. (3.4), must be compensated introducing material anisotropy due to the different treatments which the longitudinal and the transversal coordinate undergo.

The change of variable $y' = N \cdot y$, shown schematically in Fig. (3.3), translates mathematically into the following passages:

Ref$_1$:

$$\rho c_p \frac{\partial T}{\partial t} - \boldsymbol{\nabla} \cdot \Big(k(T) \boldsymbol{\nabla} T \Big) = \sigma\big(T, |\mathbf{E}|\big) \boldsymbol{\nabla} V \cdot \boldsymbol{\nabla} V \tag{3.8a}$$

$$\rho c_p(T) \cdot \frac{\partial T}{\partial t} - \frac{\partial k_x}{\partial T} \cdot \left(\frac{\partial T}{\partial x} \right)^2 - k_x \cdot \frac{\partial^2 T}{\partial x^2} - \frac{\partial k_y}{\partial T} \left(\frac{\partial T}{\partial y} \right)^2 + \tag{3.8b}$$

$$- k_y \frac{\partial^2 T}{\partial y^2} = \sigma_x \left(\frac{\partial V}{\partial x} \right)^2 + \sigma_y \left(\frac{\partial V}{\partial y} \right)^2$$

Ref$_2$:

$$\rho' c_p' \frac{\partial T}{\partial t} - \boldsymbol{\nabla} \cdot \Big(k'(T) \boldsymbol{\nabla} T \Big) = \sigma'\big(T, |\mathbf{E}|\big) \boldsymbol{\nabla} V \cdot \boldsymbol{\nabla} V \tag{3.9a}$$

$$\rho' c_p'(T) \cdot \frac{\partial T}{\partial t} - \frac{\partial k_x'}{\partial T} \cdot \left(\frac{\partial T}{\partial x} \right)^2 - k_x' \cdot \frac{\partial^2 T}{\partial x^2} - \frac{\partial k_y'}{\partial T} \left(\frac{\partial T}{N \partial y} \right)^2 + \tag{3.9b}$$

$$- k_y' \frac{\partial^2 T}{N^2 \partial y^2} = \sigma_x' \left(\frac{\partial V}{\partial x} \right)^2 + \sigma_y' \left(\frac{\partial V}{N \partial y} \right)^2$$

where $k(T)$ and $\sigma\big(T, |\mathbf{E}|\big)$ are diagonal tensors. The dependent variables of the new reference system are set equal to those of the first one and the differences between them are incorporated inside the new set of material properties, denoted by the superscript.

The change of variables adopted is sketched in Table (3.2). The equivalence between the two Reference Systems (Ref$_1$ and Ref$_2$) implies a choice
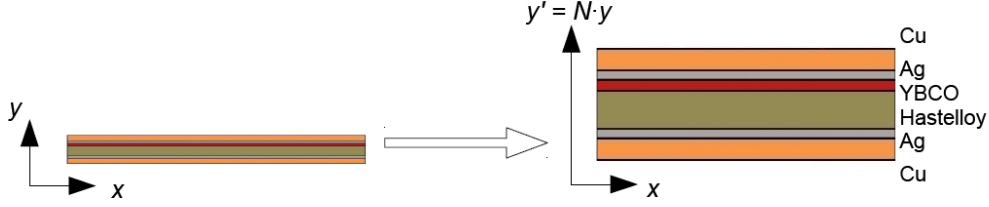
Figure (3.3) *Sketch of the anisotropic model.*

among infinite sets of anisotropic material property systems which satisfies the condition of equality term by term. In order to avoid operations of exponentiation, Eq. (3.9b) was multiplied by N at both sides before match one by one the equation terms. This operation leads to the set of anisotropic material properties reported in Table (3.3). Eq. (3.9b) is solved for every layer of the tape but the buffer layer. The buffer layer is modelled as an internal contact resistance between the superconducting YBCO layer and the substrate layer. The procedure for the implementation of the internal contact resistance in a general PDE model of the COMSOL environment is reported below:

1. create identity pairs for the interfaces which require contact resistance;

2. add a pair "zero flux" boundary condition to the identity pair;

3. add a normal "weak contribution" boundary condition for all of the boundaries in the identity pair;

4. insert the expression below for the "weak expression" in the "weak contribution":

$$if(src2dst\_P1, COND \cdot (src2dst\_P1(VAR) - VAR) \cdot test(VAR), 0)+$$

$$+if(dst2src\_P1, COND \cdot (dst2src\_P1(VAR) - VAR) \cdot test(VAR), 0)$$

where $P1$ represents the pair name, $COND$ is the interface conductivity divided by the interface thickness, VAR is the dependent variable, i.e. T for the thermal equation and V for the electric equation. The $src2dst$ and $dst2src$ variables map the distance from the destination and source of the pair. The equation solved is equivalent to the following equations, one for the thermal and the other for the electric parts of the model:

$$-\hat{n} \cdot \left(-k\boldsymbol{\nabla}T\right) = -k_{BL}\frac{(T_i - T_j)}{d_{BL}} \tag{3.10}$$

$$-\hat{n} \cdot \left(-\sigma\boldsymbol{\nabla}V\right) = -\sigma_{BL}\frac{(V_i - V_j)}{d_{BL}} \tag{3.11}$$

where k_{BL}, σ_{BL} and d_{BL} are respectively the thermal conductivity, the electrical conductivity and the thickness of the buffer layer while subscripts i and j refer to the layers between which the buffer layer is located, i. e. the YBCO and the substrate.

Reference System	Variables
Ref_1 $\left\{\vphantom{\begin{matrix}a\\b\\c\end{matrix}}\right.$	$(x,y);$ $T(x,y);$ $V(x,y)$
Ref_2 $\left\{\vphantom{\begin{matrix}a\\b\\c\end{matrix}}\right.$	$(x',y') = (x, N \cdot y);$ $T(x',y') = T(x,y);$ $V(x',y') = V(x,y)$

Table (3.2) *Change of variables between normal and anisotropic model.*

Equation	Material Properties
$\rho c_p \frac{\partial T}{\partial t} = N\rho' c_p' \frac{\partial T}{\partial t}$	$c_p'(T) = c_p(T)$ $\rho' = \rho/N$
$-\frac{\partial k_x}{\partial T}\left(\frac{\partial T}{\partial x}\right)^2 - k_x\frac{\partial^2 T}{\partial x^2} = -N\frac{\partial k_x'}{\partial T}\left(\frac{\partial T}{\partial x}\right)^2 - Nk_x'\frac{\partial^2 T}{\partial x^2}$	$k_x' = k_x/N$
$-\frac{\partial k_y}{\partial T}\left(\frac{\partial T}{\partial y}\right)^2 - k_y\frac{\partial^2 T}{\partial y^2} = -\frac{\partial k_y'}{N\partial T}\left(\frac{\partial T}{\partial y}\right)^2 - k_y'\frac{\partial^2 T}{N\partial y^2}$	$k_y' = k_y \cdot N$
$\sigma_x\left(\frac{\partial V}{\partial x}\right)^2 = N\sigma_x'\left(\frac{\partial V}{\partial x}\right)^2$	$\sigma_x' = \sigma_x/N$
$\sigma_y\left(\frac{\partial V}{\partial y}\right)^2 = \sigma_y'\left(\frac{\partial V}{\partial y}\right)^2\frac{1}{N}$	$\sigma_y' = \sigma_y \cdot N$

Table (3.3) *Anisotropic material properties implemented in the model. The relations result from a term to term matching.*

3.1.2 Electric Model

The thermal model is solved together with the stationary electrodynamics Eq. (3.4). The anisotropic change of variable leads to the following equations:

Ref_1:

$$\boldsymbol{\nabla} \cdot \Big(\sigma(T; |\mathbf{E}|)\boldsymbol{\nabla}V\Big) = 0 \tag{3.12a}$$

$$\frac{\partial \sigma_x}{\partial x}\frac{\partial V}{\partial x} + \sigma_x \frac{\partial^2 V}{\partial x^2} + \frac{\partial \sigma_y}{\partial y}\frac{\partial V}{\partial y} + \sigma_y \frac{\partial^2 V}{\partial y^2} = 0 \tag{3.12b}$$

Ref_2:

$$\boldsymbol{\nabla} \cdot \Big(\sigma'(T; |\mathbf{E}|)\boldsymbol{\nabla}V\Big) = 0 \tag{3.13a}$$

$$\frac{\partial \sigma'_x}{\partial x}\frac{\partial V}{\partial x} + \sigma'_x \frac{\partial^2 V}{\partial x^2} + \frac{\partial \sigma'_y}{N\partial y}\frac{\partial V}{N\partial y} + \sigma'_y \frac{\partial^2 V}{N^2\partial y^2} = 0 \tag{3.13b}$$

In order to avoid numerical problems the non-linear behaviour of the superconductor, defined in Eq. (3.5), is introduced in the electric conductivity of the YBCO layer, defined as a sum of two different components:

$$\sigma_{YBCO}\Big(T, |\mathbf{E}|\Big) = \frac{J_c(B,T)}{E_0}\left(\frac{|\mathbf{E}|}{E_0}\right)^{1/n-1} + \sigma_{NC}(T) \tag{3.14}$$

The first term is the superconducting electrical conductivity while $\sigma_{NC}(T)$ is the YBCO normal state electrical contribution. In order to avoid irregularity in Eq. (3.14) and in its derivative, and to guarantee convergence of the numerical model, a spline interpolation function is adopted to link the superconducting to the normal conducting electrical conductivity. The critical current density J_c is valid for $0 < T \le T_{lim}$ where T_{lim} is the temperature upper limit to avoid singularity in Eq. (3.6) and it is equal to:

$$T_{lim} = T_c \cdot \left[1 - \left(\frac{B + \epsilon}{B_{irr_0}}\right)^{1/\alpha}\right] \tag{3.15}$$

Due to the strong non-linearity of the critical current density a sudden drop from $J_c(T_{lim})$ to zero might appears. In order to assure continuity of the critical current density, and therefore of the electrical conductance, the following joint exponential function is introduced for $T > T_{lim}$

$$f(T) = a \cdot exp(b/T) + c \tag{3.16}$$

where a, b and c are parameters obtained from the boundary conditions below:

$$\begin{cases} \lim_{T \to \infty} f(T) = 0 \; \to \; 0 = a + c \; \to \; c = -a \\ \\ f(T_{lim}) = a \cdot exp(b/T_{lim}) + c \\ \\ f'(T_{lim}) = -ab \cdot exp(b/T_{lim})/T_{lim}^2 \end{cases}$$

Fig. (3.4) illustrates the smoothing effect introduced by Eq. (3.16). The error introduced is negligible since the electrical conductance of the YBCO is dominated by the normal contribution σ_{NC} in the temperature range considered. For a transport current of 300 A for example the superconducting electrical conductance σ_{SC} is equal to 6.44e-34 [S/m] at T_{lim} while the normal contribution is equal to 3.70e+5 [S/m]. The joint function has to be recalculated at every transport current since T_{lim} depends on B which in turn depends on I as discussed below.
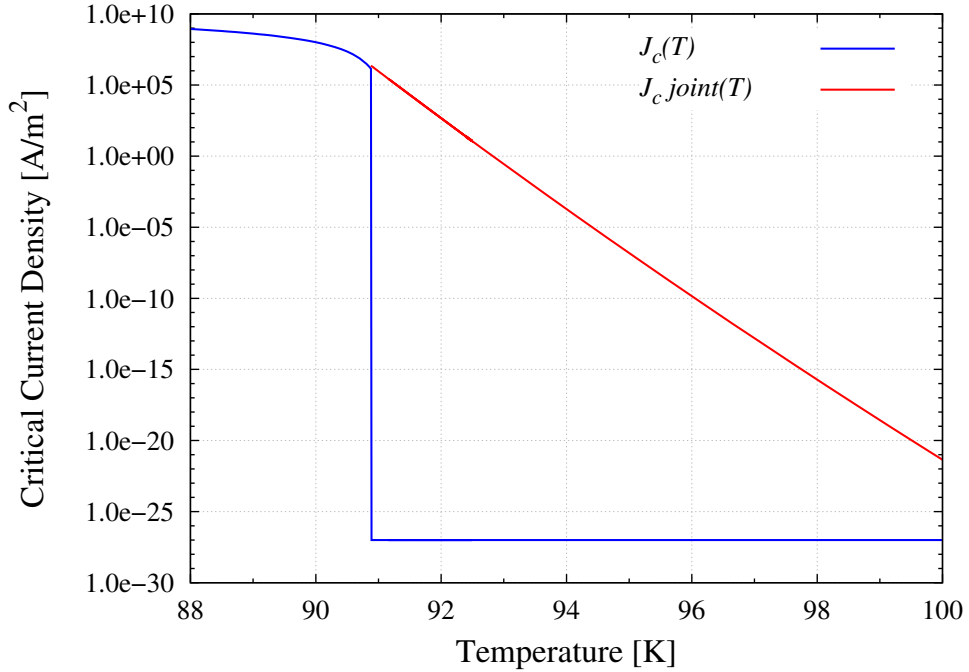
Figure (3.4)   *Critical current density as a function of temperature with (red line) and without (blue line) smoothing.*
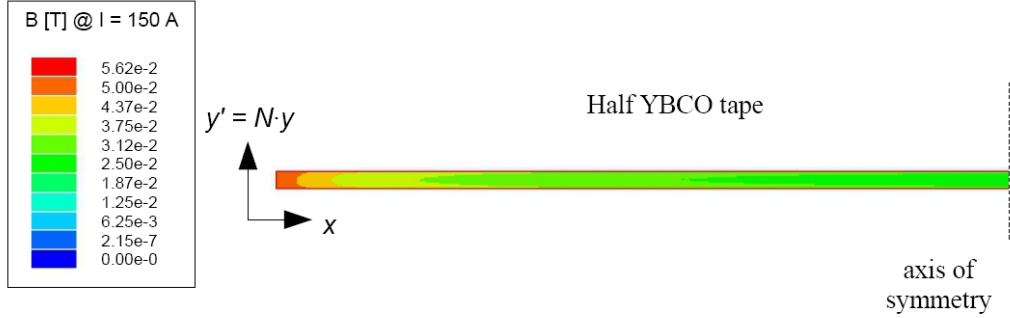
Figure (3.5) *Distribution of the magnetic flux density in half-section YBCO tape.*

The electric filed is defined as:

$$\left|\mathbf{E}\right| = \sqrt{(\partial V/\partial x)^2 + (\partial V/\partial y)^2} + e_0 \tag{3.17}$$

with $e_0 = 10^{-10}$ V/m is introduced to avoid the appearance of complex solutions in Eq. (3.14).

The magnetic flux density, which appears as an independent variable in the definition of the critical current density, is introduced as an external constant field and it is not solved during calculations. In order to minimize thermal stability overestimation, the external magnetic flux density adopted is the maximum self field produced by the YBCO layer in the superconducting state. In this case all the current is transported by the superconducting material and the maximum value is located in the middle point of the vertical boundary, as shown in Fig. (3.5). The maximum magnetic flux density is evaluated at different values of the transport current, ranging from 50 to 1000 A. The numerical data are then fitted by the linear function below:

$$B_{self} = 4.305 \cdot 10^{-4} \cdot I \quad \text{T} \tag{3.18}$$

where I is the transport current. As reported in Fig. (3.6) the linear interpolation is in perfect agreement with the numerical data.
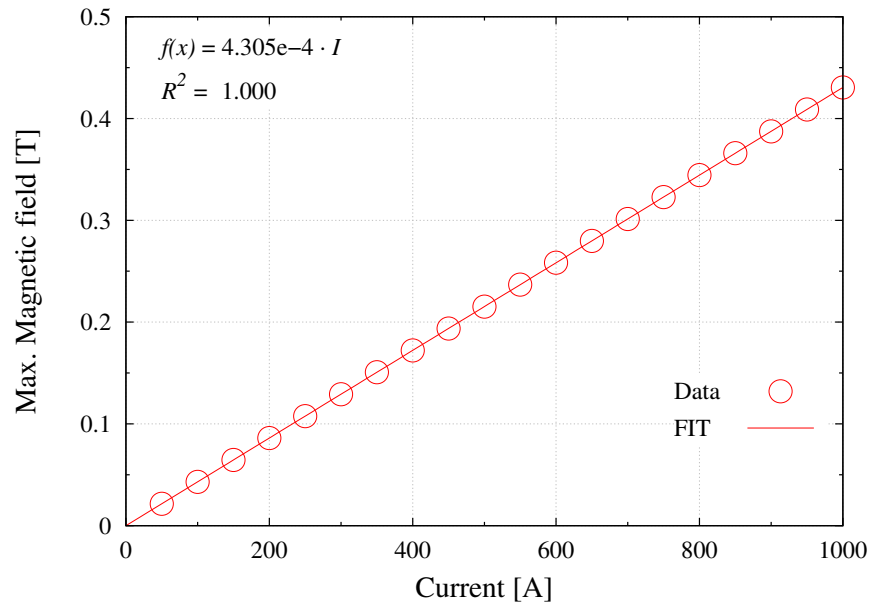
Figure (3.6) *Maximum magnetic flux density as a function of transport current.*

3.2 MATERIAL PROPERTIES

The availability of accurate material properties is of paramount importance to ensure high simulation reliability. The thermal and electrical properties, mainly the thermal conductivity, the specific heat and the electrical resistivity, are introduced in the FEM model as functions of temperature and, in some cases, like for the electrical conductivity of copper, of the magnetic field and RRR. The density values, reported in Table (3.4), are taken constant with temperature in the model.

The main issue in the definition of the material properties is their scarce availability especially in the low temperature range, below 200 K. For this purpose a deep bibliographic research was carried out [41, 42, 43, 44, 45].

The specific heat c_p is defined as the quantity of energy per unit mass required to change the temperature of an object by one Kelvin at constant pressure. The dependence of this property on temperature is reported, for materials that usually compose YBCO CC, in Fig. (3.7), sorted by decreasing values at ambient temperature, from stainless steel to silver.

The thermal conductivity k is the ability of a material to conduct heat defined by the Fourier's law:

$$\boldsymbol{q} = -k\boldsymbol{\nabla}T$$

Fig. (3.8) reports this parameter as a function of temperature for the materials considered, sorted by decreasing values at ambient temperature too. The y-axis is in logarithmic scale to better compare the different materials.

The electrical resistivity quantifies how strongly a given material opposes the flow of electric current. Its value as a function of temperature is visible in Fig. (3.9) with a logarithmic y-axis. The strong non-linearity of the YBCO electrical resistivity in the superconducting regime, under 92 K, appears clear.

Material	γ [kg/m^3]
Cu	8960
Ag	10630
Hastelloy®	8890
YBCO	6380
Stainless Steel	7900
NiW	10400

Table (3.4) *Density of the materials composing the YBCO CC tapes.*
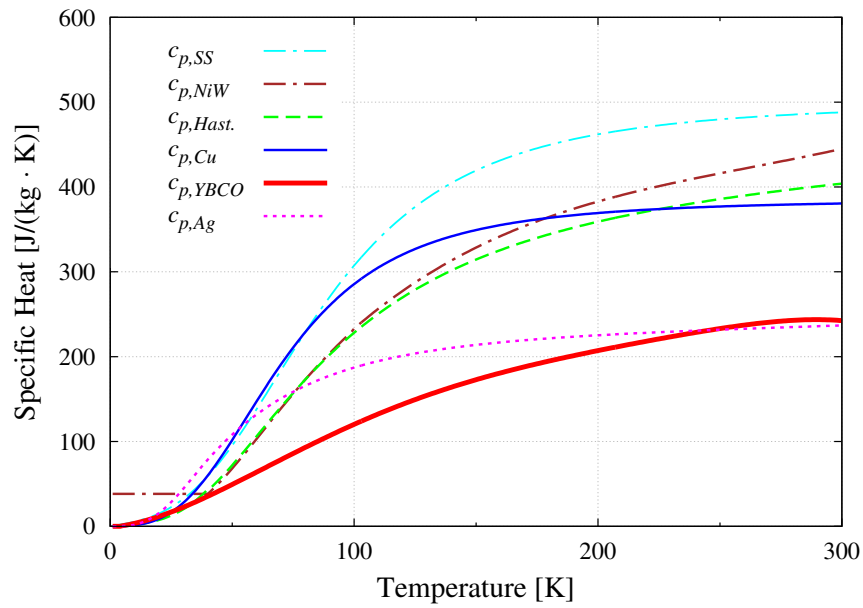
Figure (3.7) *Specific Heat as a function of temperature of the material composing the YBCO CC tapes.*
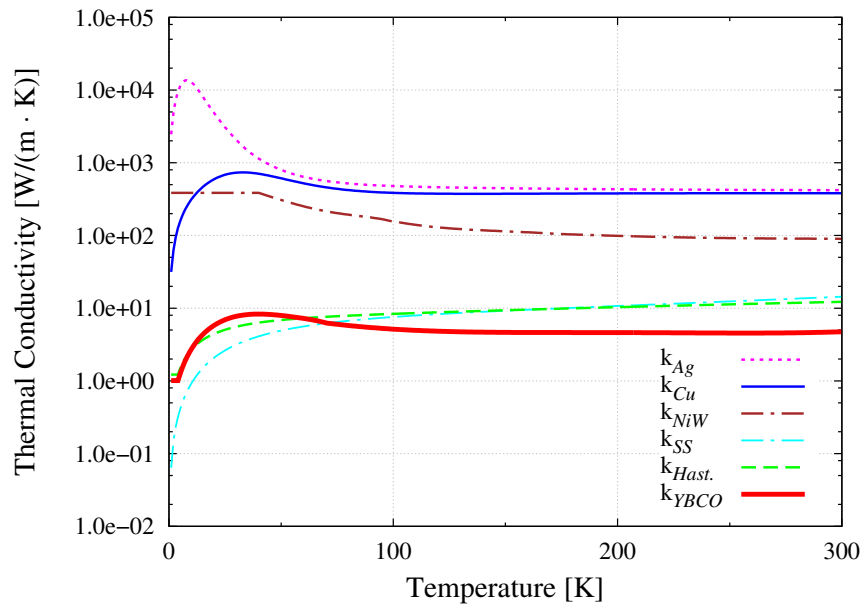
Figure (3.8) *Thermal Conductivity as a function of temperature of the material composing the YBCO CC tapes.*
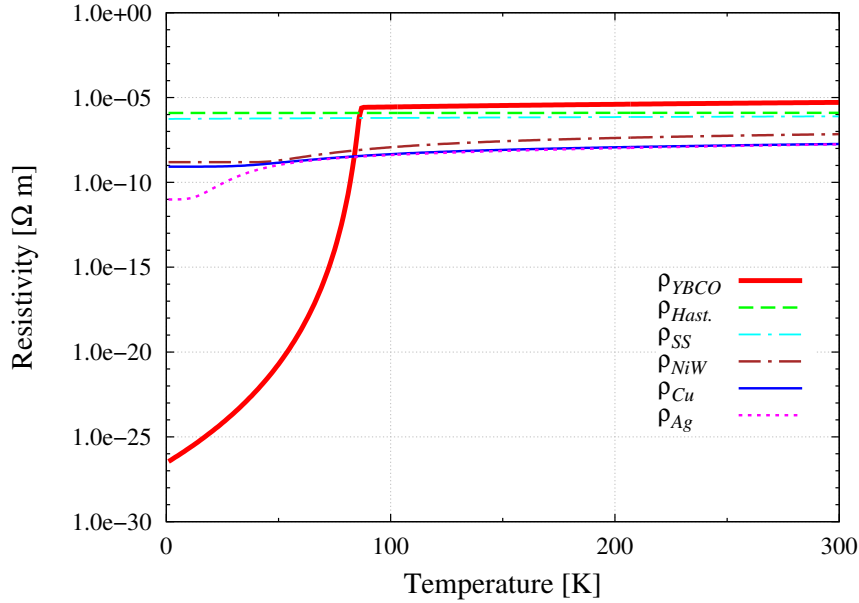
Figure (3.9) *Electrical Resistivity as a function of temperature of the material composing the YBCO CC tapes.*

The role of the different materials inside a YBCO CC tape can be guessed observing the graphs. The copper and the silver are characterized by the lowest electrical resistivity, once the superconducting regime has been exceeded, and by the highest thermal conductivity. For that reason they are called "stabilizers" thanks to their ability to carry current and heat with low heat generation. The substrate materials (NiW, stainless steel and Hastelloy®) are instead characterized by the highest specific heat as well as high mechanical strength, while they are poor heat and current conductors. Their primary role is to give mechanical stability to the tape. The YBCO is the superconducting material used to carry current without losses while the superconductivity state is maintained. However, as already anticipated at the beginning of this chapter, its thermal properties are poor. The numerical values of all the properties used in the simulations are reported in the tables of Appendix A.

3.3 STRUCTURED MAPPED MESH & CONVERGENCE

The automatic meshing of the YBCO tape leads to a very high number of elements, since traditional meshing techniques adopt elements with an aspect ratio close to unity [46]. For example more than $2 \cdot 10^4$ triangular elements are needed for and extremely fine physics controlled mesh in the simulation of a 5 cm long tape. As a result, the number of degrees of freedom gets very high value causing in turn long calculation times and memory requirements. However, the possibility and validity of the implementation of a structured mapped mesh has already been demonstrate for the simulation of thin film superconductors [47]. Every element of the model should be meshed apart with a structured quadrilateral mesh fine enough to reach convergence. A parametric study on the mesh size, whose results are reported below, shows that no more then two or four elements in the thickness dimension not shorter than 0.5 mm are needed to achieve convergence. Less than $2.5 \cdot 10^3$ elements are sufficient for the above mentioned example which means an order of magnitude elements reduction and consequently a large reduction of calculation time. Fig. (3.10) reports the automatic triangular mesh in comparison with the structured quadrilateral mesh, the advantage of the structured mesh is clear.

The convergence study has been performed taking into account three different parameters:

- the length of the elements in the longitudinal dimension, Δx;

- the length of the elements in the vertical dimension, Δy;

- the maximum time stepping, Δt_{max}.

The tape considered for this study was produced by American Superconductor Corporation [48] and its cross section is reported in Fig. (3.11). This sample is characterized by the absence of the silver layer between the substrate and the bottom copper stabilizer and a substrate made of nickel-tungsten. More details about this sample and experimental results performed on it are reported in [49]. The 10 cm length sample is anchored on the 2nd stage of a cryostat by means of a two cm length welding on two current leads. A set of voltage taps are soldered on the tape at a distance of 1 cm from each other and a thermocouple is fixed between them. The W-shaped heater, 0.5 cm long, is attached in the middle of the sample to the copper side on the top of the tape by epoxy. Therefore, the simulation domain is symmetric with respect to the midpoint of the heater, so that the experiment could be simulated taking the 5 cm tape length sketched in Fig. (3.12). The current is fed
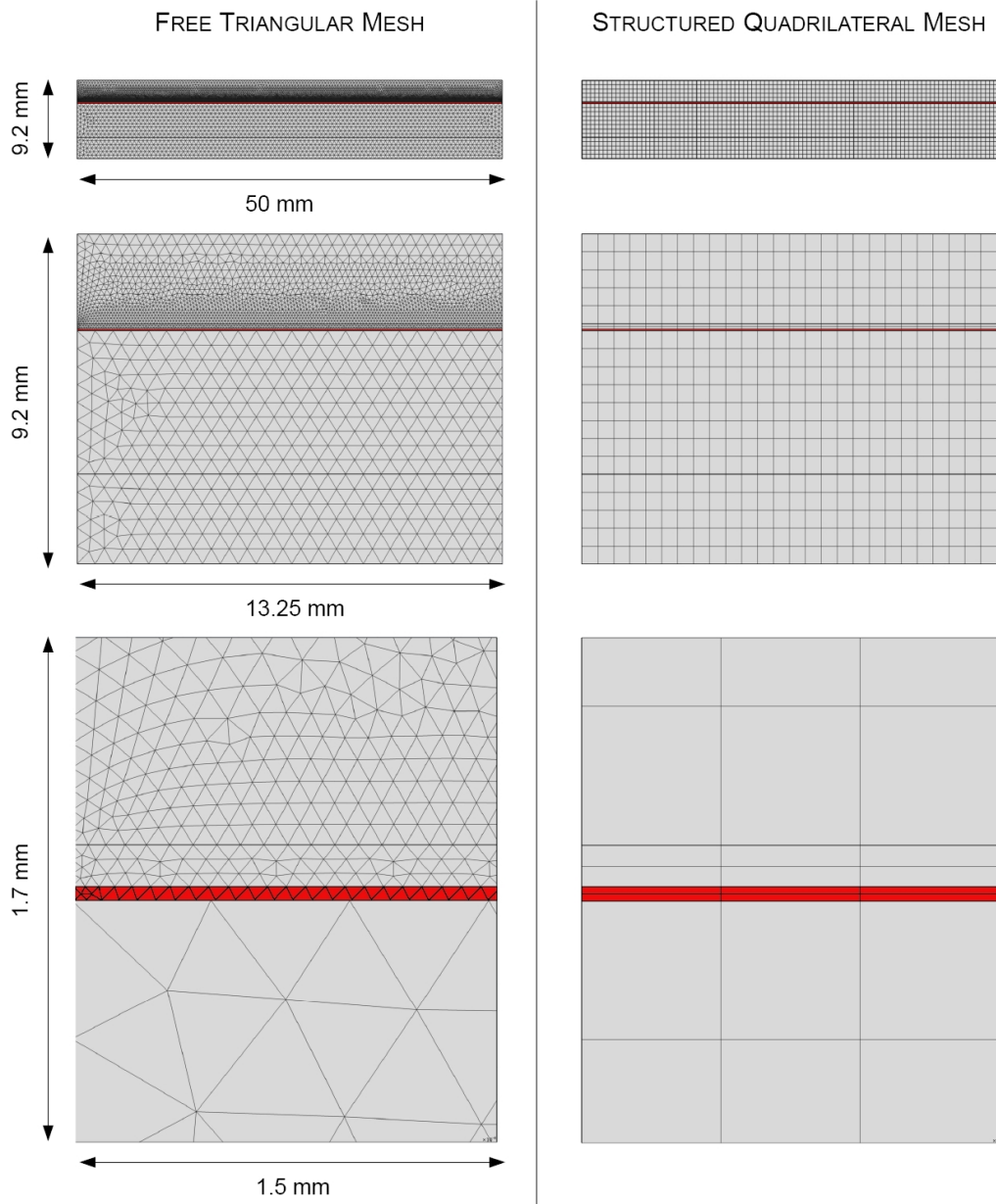
Figure (3.10)   *Consecutive zoom of the YBCO tape mesh. Left column adopts a free triangular mesh composed of more than $2 \cdot 10^4$ elements while right column adopts a structured quadrilateral mesh which requires only $2.5 \cdot 10^3$ elements. The 1 µm thick YBCO layer is highlighted in red.*
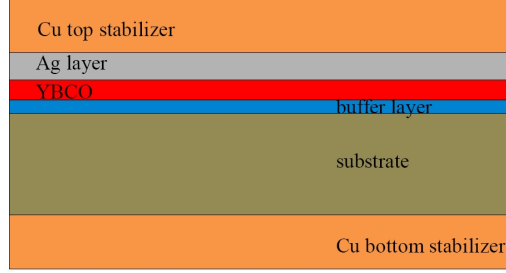
Figure (3.11)   *Schematic cross section of the YBCO conductor considered for the convergence study (not to scale). The width of the sample is* 4.3 mm *while the stabilizer layers and the substrate are respectively* 50 μm *and* 80 μm *height.*

into the tape on a 2 cm long length both from the bottom and the top copper stabilizer to simulate the welding of the real tape while the temperature is fixed only on the bottom surface where the current leads are clamped to the cryostat plate. The right side is characterized by an adiabatic boundary condition on temperature and by a Dirichlet boundary condition on voltage ($V = 0$). The heat is introduced from the top side on a length of 2.5 mm which represent half of the real heater. The pulse is 0.25 s long.

The convergence study was performed in the following operating conditions:

- $I = 200$ A; $T_{in} = 50$ K; $L = 0.01$ m;

- $P_{recovery} = 0.8$ W; $P_{quench} = 0.9$ W.

Fig. (3.13)-(3.16) report the results performed with the following set of parameters, both for the recovery case and the quench case:

1. High discretization $\Delta x = 0.5$ mm, $\Delta t_{max} = 0.001$ s;

2. Medium discretization $\Delta x = 1.25$ mm, $\Delta t_{max} = 0.01$ s;

3. Low discretization $\Delta x = 2.5$ mm, $\Delta t_{max} = 0.1$ s.

The comparison between results obtained with the three sets of values shows that using the first set of parameters is mandatory for convergence. The Low discretization set determines large differences in the recovery case and it is not able to reproduce the quench behaviour in the quench case. The average relative percentage error between the High and the Medium discretization is equal to 0.24 % and 5.96 % for temperature and voltage time
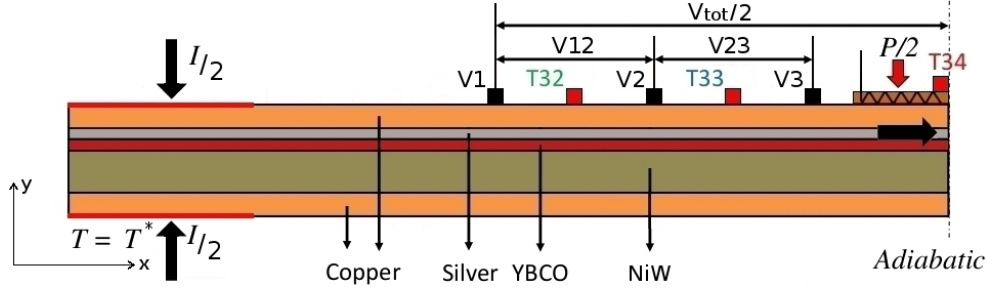
Figure (3.12) *Sketch of the simulated domain. The current is fed into the tape at the left side both from the top and from the bottom copper stabilizer. At the right side, that appears to be an axis of symmetry of the simulated domain, and adiabatic boundary condition on temperature and a Dirichlet boundary condition on voltage ($V = 0$) is provided.*

evolution respectively. However the maximum error on voltages is equal to 67.61 %, while it only reaches 3.11 % for the temperatures. This implies that also the Medium discretization set should be discarded.

A second convergence study was then performed at fixed time stepping, $\Delta t_{max} = 0.001$ s. This study shows only minimum differences varying the length of the elements in the longitudinal dimension. The length of the element must be a multiple of the heater length, 2.5 mm long, in order to allow the use a structured quadrilateral mesh. The result of this study, in terms of percentage relative error with respect to the High discretization set of parameters, is summarized in Table (3.5).

The results of these convergence studies shows that a maximum time step of 0.001 s is necessary and a length of the elements in the longitudinal dimension of 1.25 mm is sufficient for reaching convergence. Moreover, once these parameters have been set, the length of the elements in the vertical dimension, Δy, appears to have a negligible effect on results.

Δx	T_{avg} err. %	T_{max} err. %	V_{avg} err. %	V_{max} err. %
0.50 mm	0.00 %	0.00 %	0.00 %	0.00 %
1.25 mm	0.01 %	0.06 %	0.16 %	2.16 %
2.50 mm	0.04 %	0.58 %	1.26 %	18.49 %

Table (3.5) *Average and maximum relative percentage error at fixed time stepping: $\Delta t_{max} = 0.001$ s.*
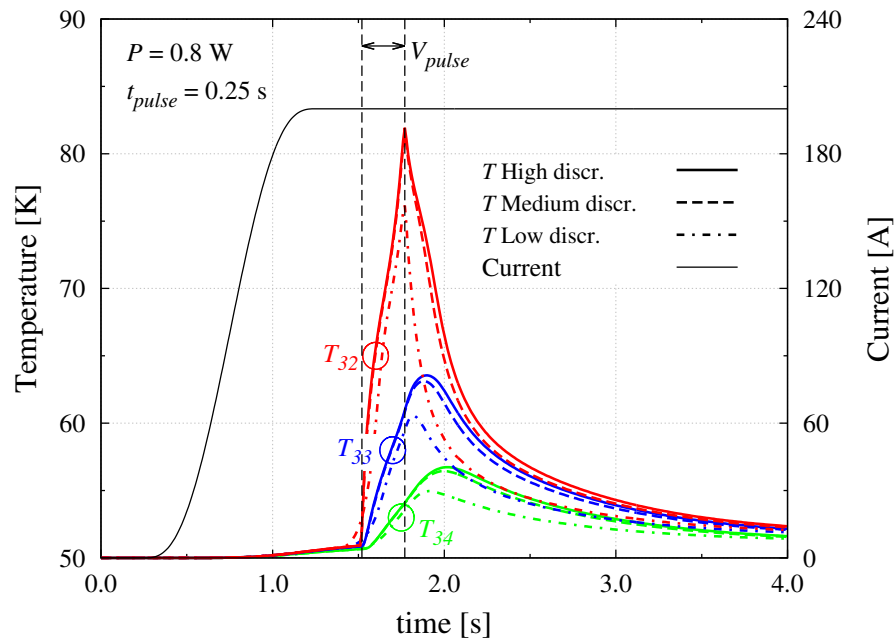
Figure (3.13) *First convergence test: recovery temperature evolution.*
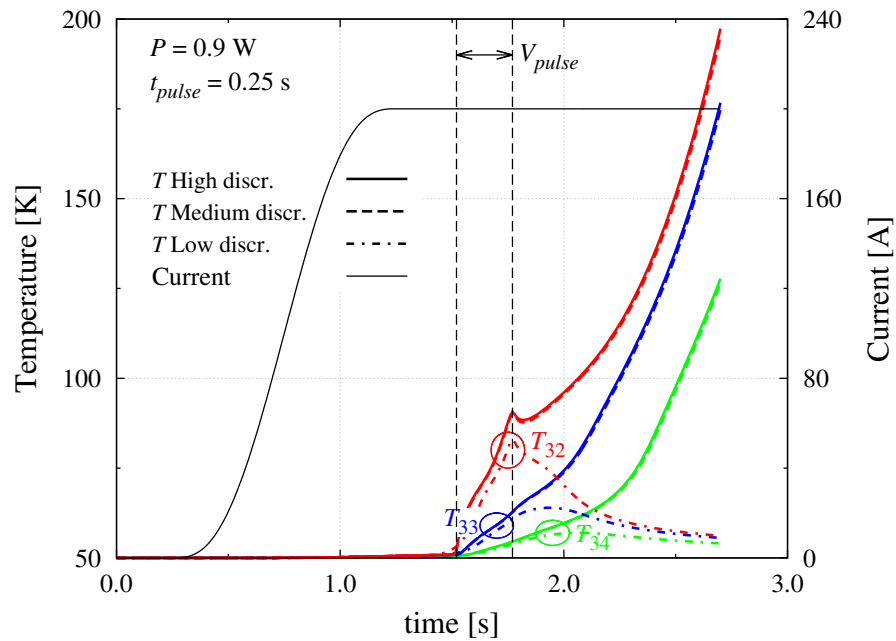
Figure (3.14) *First convergence test: quench temperature evolution.*
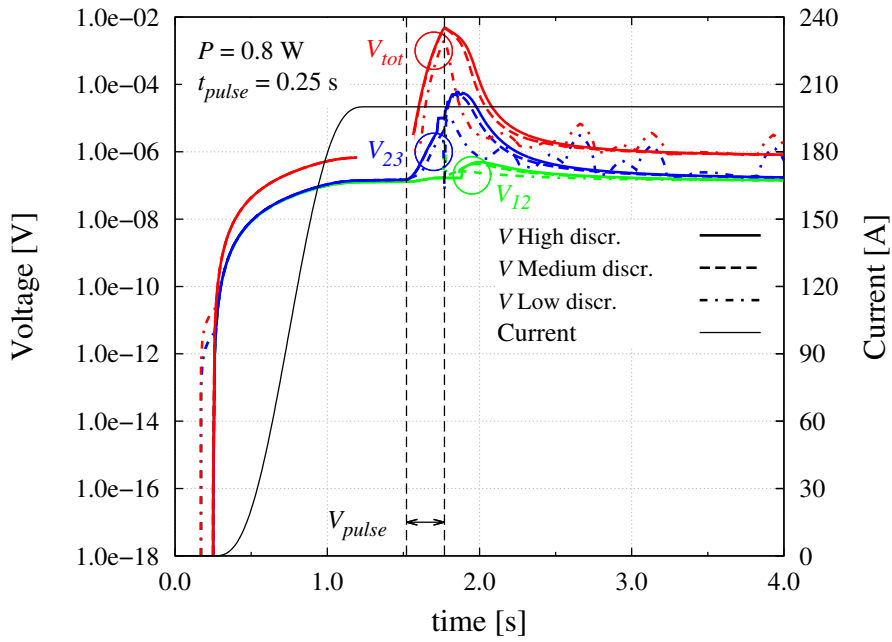
Figure (3.15) *First convergence test: recovery voltage evolution.*
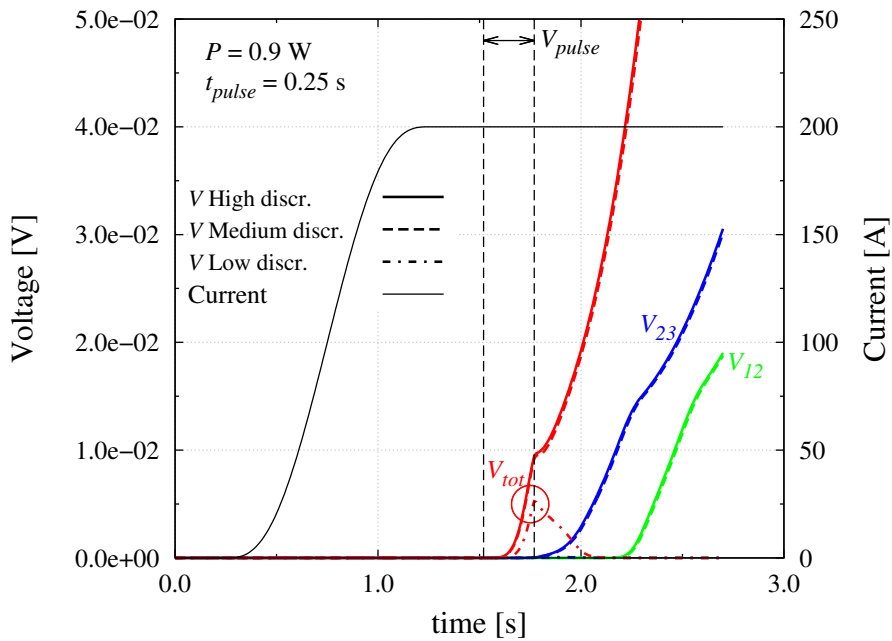
Figure (3.16) *First convergence test: quench voltage evolution.*

3.4 PANCAKE MODEL DESCRIPTION

The model described for the study of the YBCO tape was then extended to coils and windings.

The first step was the definition of the single tape homogenized properties for the modelling of the windings located far from the external heat deposition region. The whole tape was considered as a single element taking into account all the material properties of the layers which compose it, including the buffer layer. To determine both the thermal and electrical conductivities, the YBCO tape was modelled as a circuit consisting of a set of resistors per unit length while the specific heat was derived from an average weighted on the cross sections.

Afterwards, the same approach was used for the homogenization of a tape stack, composed by homogenized tape electrically insulated with each other from an insulating material.

3.4.1 Single Tape Homogenization

The homogenized tape conductivity changes in relation to the direction of heat or current flow. In case of a longitudinal flow the different layers of the YBCO tape should be modelled as a set of resistances linked together by transversal resistances as shown in Fig. (3.17). Since the aim of the equiv-
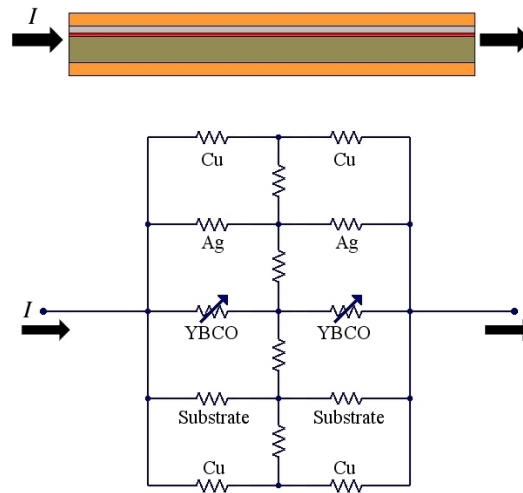
Figure (3.17) *Sketch of the resistance equivalent circuit in case of a longitudinal flow.*

alent circuit is the definition of material properties, which are independent of the geometry, hence of the length considered, the analysis is carried out with resistances per unit of length. Every resistance per unit length is then divided into two equal parts in order to accommodate the transversal resistances per unit height. The transversal resistances are computed considering half the thickness of the two materials in contact except for the one which connects the YBCO and the substrate which is dominated by the buffer layer. However, in this configuration the transversal resistances contribution to the total resistance of the circuit appears to be negligible.

The circuit turns into a set of parallel resistors and the total conductance can therefore be computed as the sum of the conductance of each layer. The thermal and the electrical longitudinal conductivities are therefore expressed by the following expression:

$$\sigma_{eq}^L = \frac{\sum_i \sigma_i \cdot d_i}{d_{tot}} \quad ; \quad k_{eq}^L = \frac{\sum_i k_i \cdot d_i}{d_{tot}} \tag{3.19}$$

where the subscript i refers to the ith layer of the tape and d is the thickness of the layer considered.

In case of a transversal flow the equivalent circuit turns into the one represented in Fig. (3.18). The resistances per unit height are in series and the equation for the transversal conductivity are:

$$\sigma_{eq}^T = \frac{d_{tot}}{\sum_i d_i/\sigma_i} \quad ; \quad k_{eq}^T = \frac{d_{tot}}{\sum_i d_i/k_i} \tag{3.20}$$
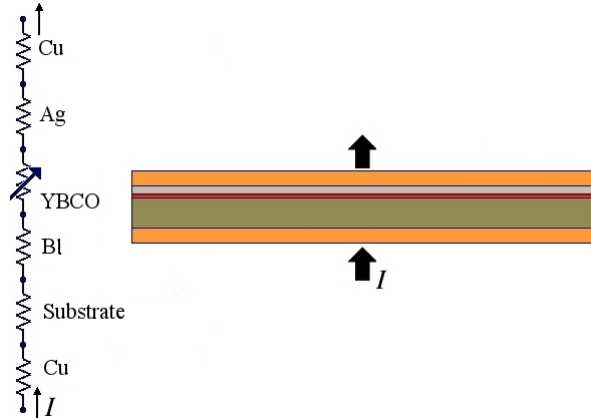
Figure (3.18)   *Sketch of the resistance equivalent circuit in case of a transversal flow.*
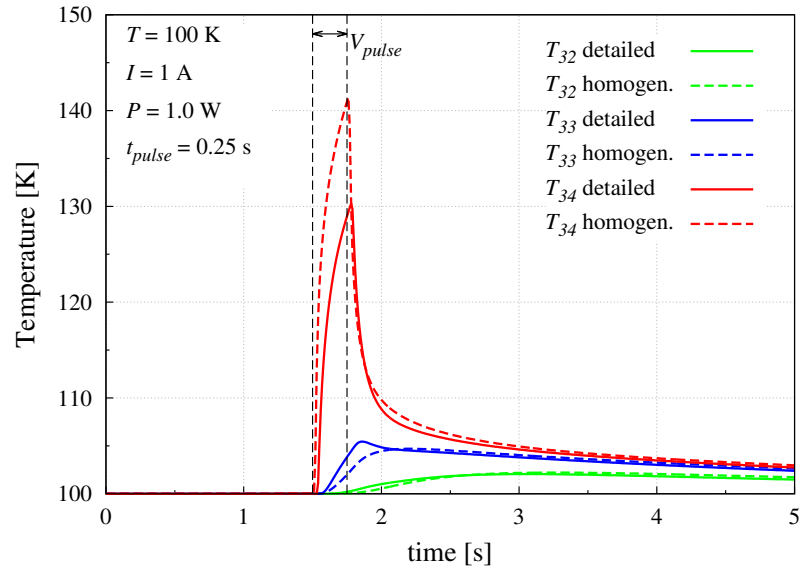
Figure (3.19) *Comparison between the tape detailed and homogenized models. Normal conducting tape: temperature evolution.*
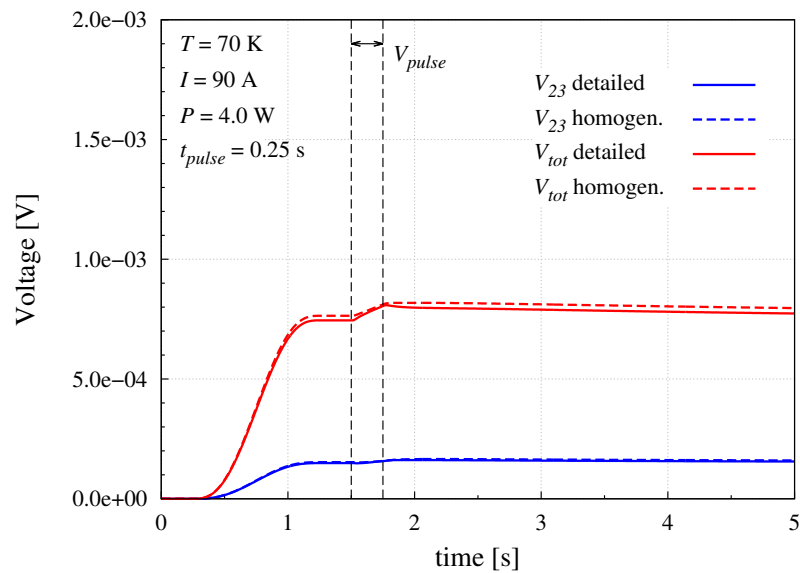
Figure (3.20) *Comparison between the tape detailed and homogenized models. Normal conducting tape: voltage evolution.*
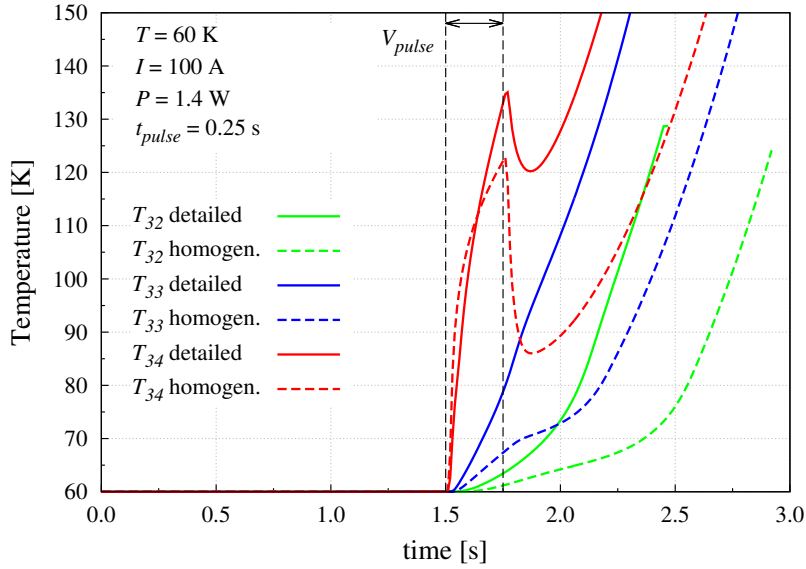
Figure (3.21) *Comparison between the tape detailed and homogenized models. Quench: temperature evolution.*
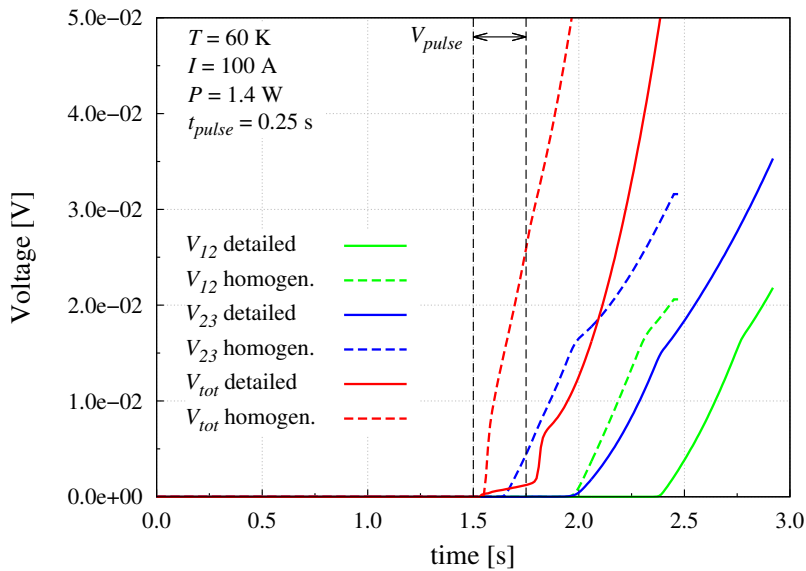
Figure (3.22) *Comparison between the tape detailed and homogenized models. Quench: voltage evolution.*

Fig. (3.19)-(3.22) shows the results of a comparison between the detailed model, which takes into account all the different layers of the tape, and the homogenized model of the tape. In a first case, one watt of heat power is deposited in a YBCO tape at 100 K, hence in the normal conducting state. The homogenized model is in excellent agreement with the detailed one, with only a slight underestimation of the maximum temperature achieved. The differences between the models appear larger in the second case where a quench behaviour is investigated. Both temperature and voltage evolutions are similar but with remarkable differences in the quench starting point.

The results shown suggest that the homogenized model is not able to catch the solution features in case of a quench but it is a good approximation of a tape in regions far enough from the heat source.

3.4.2 Tape Stack Homogenization

Following the same circuital approach just described, the tape stack homogenized properties were determined. Since in the tape stack considered every superconducting tape is surrounded by two Kapton layers, to ensure electrical insulation among them, the electrical conductivity in the transversal direction is neglected and its value is considered equal to that of the insulating material.

In order to validate the homogenized coil model the quench behaviour of a stack of nine tapes was investigated. Two levels of approximation were compared: in the first case the three central tapes are modelled in detail while in the second case only the central one, characterized by the presence of the heater, with the tape just above and just below modelled as a single homogenized tape. The central stack is then surrounded by two stacks of three tapes in both cases. A sketch of the models is reported in Fig. (3.23).

The comparison was performed both in a recovery case and in a quench case in the following operating conditions:

- $T_{in} = 50$ K;

- $I_{op} = 100$ A;

- $t_{pulse} = 0.25$ s;

- $P_{recovery} = 2.0$ W;

- $P_{quench} = 6.0$ W;

The tapes which compose the central stack, modelled individually in both models, are called Tape 1, Tape 2 and Tape 3, while the two stacks are

Figure (3.23) *Model studied to validate the stack homogenization. a) detailed, b) homogenized.*

defined as Bottom and Top Stacks. The heater, 0.5 mm long, is located on the right side on top of Tape 2. The simulation domain is once again symmetric with respect to the right boundary and the boundary conditions are the same already explained in Fig. (3.12). The only difference is that the operative current density has to be fed apart for every tape of the stacks: for the detailed tapes the current is introduced only in the YBCO layer while in the homogenized tape and stacks on all over the thickness of the element considered.

The results of this comparison are summarized in Fig. (3.24)-(3.27) where the temperature evolutions of Tape 1 and of Top Stack are reported. As can be seen the homogenized model implies a small overestimation of the maximum temperature in the recovery case and a time slowdown of the temperature drift in the quench case. However, the relative percentage error, with respect to the detailed model, is at most equal to about 18%, as confirmed by Table (3.6) and Table (3.7).

RECOVERY

Rel. err. %	Tape 1	Tape 2	Tape 3	Top Stack
avg.	-0.51 %	-0.74 %	-1.09 %	-0.30 %
max.	+0.53 %	+0.00 %	+0.79 %	+0.01 %
min.	-4.93 %	-13.29 %	-6.28 %	-1.02 %

Table (3.6)　*Average, maximum and minimum relative percentage error with respect to the detailed model in the recovery case.*

QUENCH

Rel. err. %	Tape 1	Tape 2	Tape 3	Top Stack
avg.	+0.51 %	-3.92 %	-12.00 %	-1.93 %
max.	+18.27 %	+0.43 %	+2.17 %	+0.03 %
min.	-3.19 %	-17.88 %	-17.69 %	-13.87 %

Table (3.7)　*Average, maximum and minimum relative percentage error with respect to the detailed model in the quench case.*
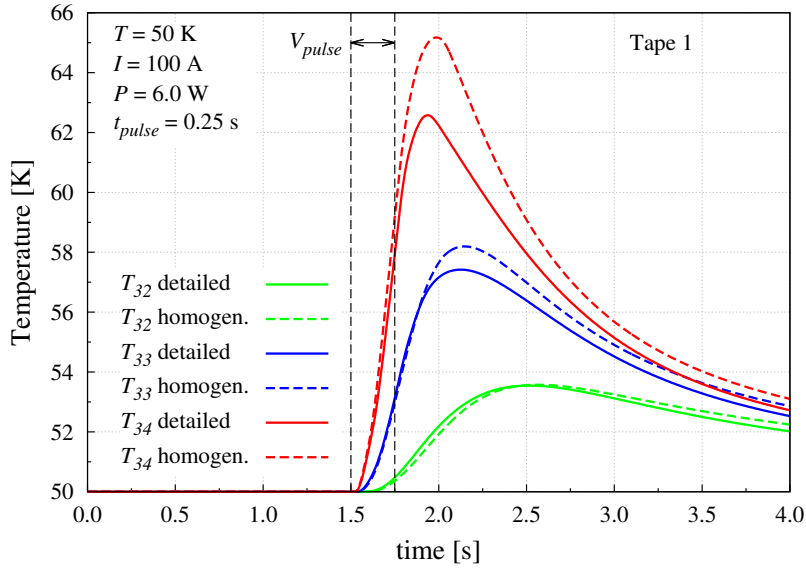
Figure (3.24) *Comparison between the stack detailed and homogenized models. Recovery: Tape 1 temperature evolution.*
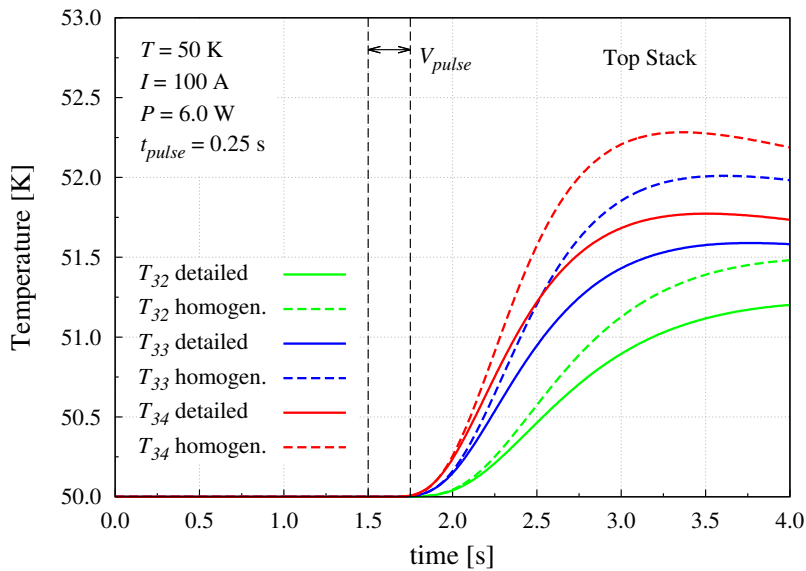
Figure (3.25) *Comparison between the stack detailed and homogenized models. Recovery: Top Stack temperature evolution.*
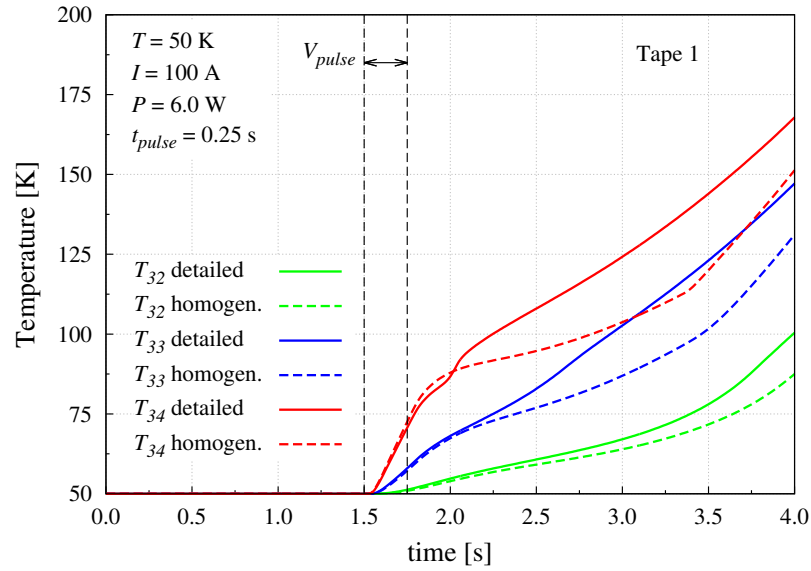
Figure (3.26) *Comparison between the stack detailed and homogenized models. Quench: Tape 1 temperature evolution.*
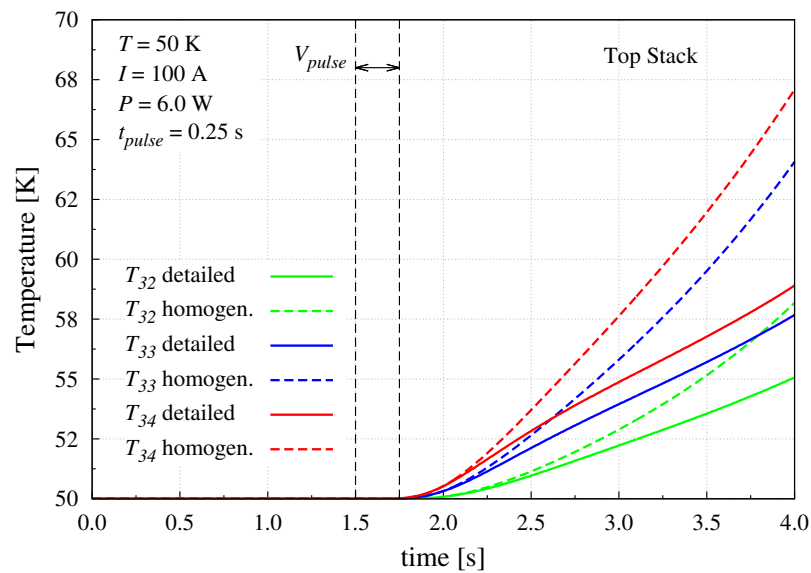
Figure (3.27) *Comparison between the stack detailed and homogenized models. Quench: Top Stack temperature evolution.*

Chapter 4

Measurements and Simulation Results

In this Chapter the main measurements data obtained on the YBCO coated conductor tapes are reported as well as the validation of the thermo-electric 2D FEM model developed and explained in Chapter 3.

In Section (4.1) the results of the anisotropic model are compared to those of a 1D quench model based on a non-linear electric circuit coupled to a thermal model of the tape. At first the analysis of a critical current case, where the operative current is incremented with a current ramp, is reported. Secondly the response to the introduction of heat in the central part of the simulation domain is evaluated both in case of a recovery and in case of a quench.

Section (4.2) summarizes the results of the model with respect to literature measurements. The agreement between measurements and simulations is rather good both for critical currents, minimum quench energies and normal zone propagation velocities. However, about 50% of the heat produced by the heater has to be considered dissipated in oder to match the minimum quench energies trends. This characteristic is well known and it is due to the difficulty of quantifying the real amount of energy from the heat pulse that is actually deposited into the tape.

Finally Section (4.3) reports the comparison of the simulations with respect to the in situ critical current and quench measurements made on a YBCO stabilized tape SCS6050-AP, manufactured by SuperPower® inc.

4.1 Comparison with 1D Circuit Model

The 2D FEM model developed was at first validated by comparison with a 1D quench model based on a non-linear electric circuit coupled to a thermal model of the tape. The analyzed case refers to a 20 cm long SF06050 tape manufactured by SuperPower® inc. characterized by a critical current of 120 A at 77 K and by a *n-value* equal to 10. As shown in Fig. (4.1) the electric field produced by the 2D model is in excellent agreement with the circuit model one except for the beginning of the current ramp. This behaviour is probably due to the fact that the one-dimensional model takes into account the inductive effects while the two-dimensional model neglects them. The critical current, estimated with a critical field of 10^{-4} V/m, is 130.5 A and 128.9 A, respectively for the 1D and the 2D models, which means a percentage relative error of 8.1% with respect to nominal value.

The comparison between the two models was then carried out for the study of the temperature evolution during an energy deposition due to an external disturbance. The external heat source was modelled as a 0.5 mm long resistive heater located in the middle of the tape, in agreement with the sketch reported in Fig. (3.12). The heat deposition is a pulsed release of energy, lasting 0.25 s. Two different cases, described below, were analyzed.

- Recovery case, Fig. (4.2): the temperature raises during the heater operation, indicated by the vertical black dashed lines, but after about 1.5 s it returns to its initial values, thus recovering superconductivity.

- Quench case, Fig. (4.3): the temperature continues to grow also after the heat pulse is exhausted, leading to values which can melt the tape.

In the first case, characterized by 0.3 W of deposited heat power, the two models show a perfect agreement with only a slight overestimation of the peak temperature regarding the 1D model. In the quench case, where the deposited energy is equal to 1.25 W, the difference is more pronounced all along the simulation. The temperatures start to grow together, but the growth rate is more pronounced in the circuital model. However, since the simulated phenomena is highly non-linear and very sensitive to parameter variations and since the two models differ in the superconducting regime definition[1], the result is remarkable. Fig. (4.4) reports the comparison of the minimum quench energy of the tape at 50 K as a function of the operating current. The two curves are almost overlapped, emphasizing the models correspondence.

---

[1]the 1D model defines the superconducting elements with a perfect parallel between the superconductor and a normal metal.
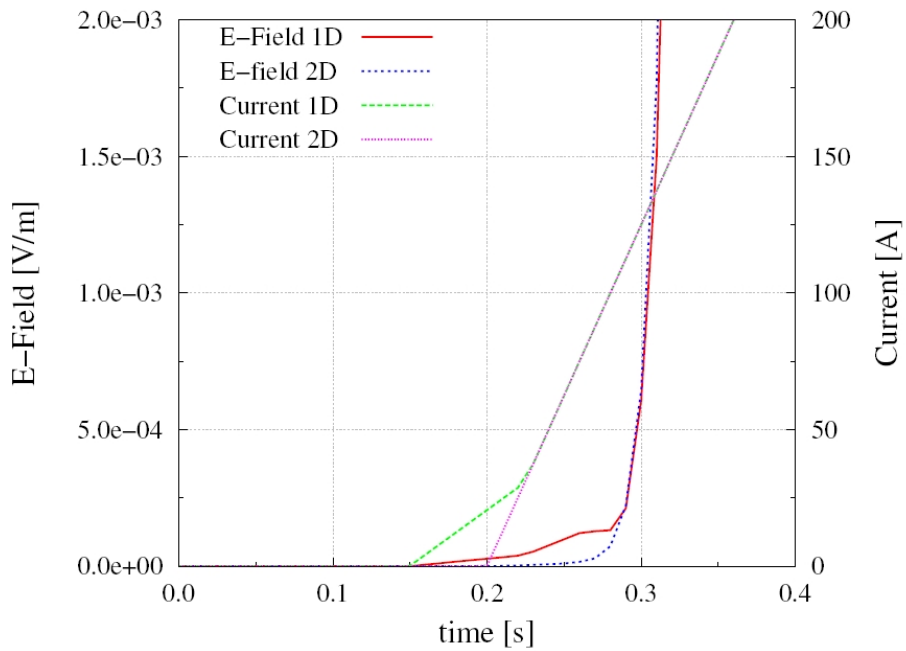
Figure (4.1) *Electric field comparison between the 1D and the 2D models.*
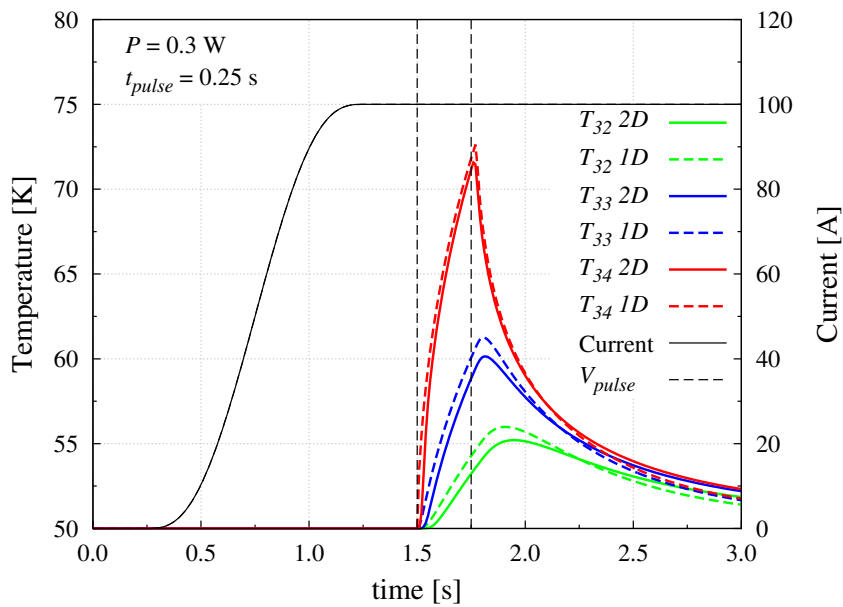
Figure (4.2) *Temperature vs time comparison between the 1D and the 2D models during a recovery.*
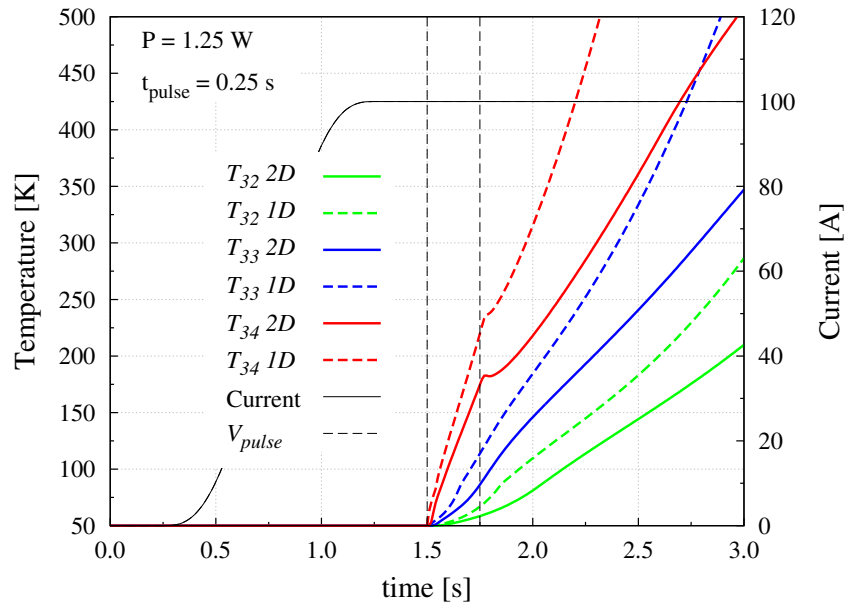
Figure (4.3)   *Temperature vs time comparison between the 1D and the 2D models during a quench.*
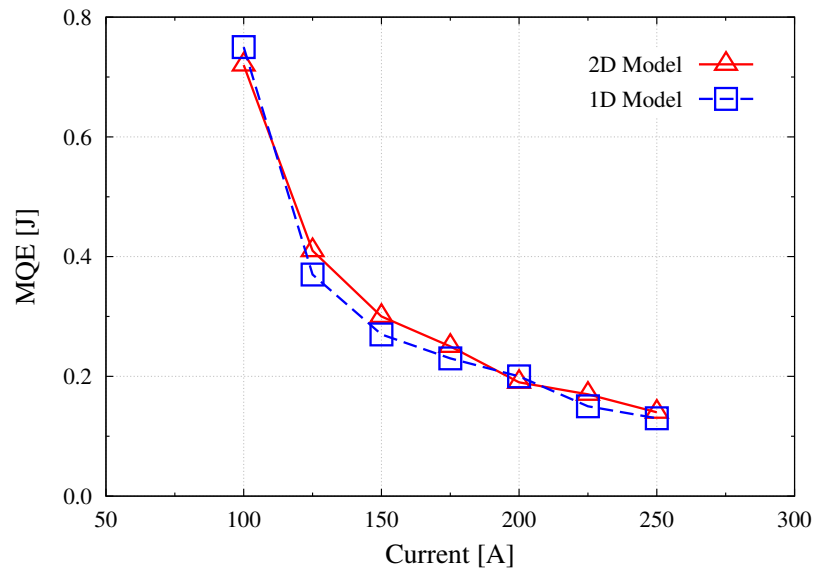
Figure (4.4)   *Minimum Quench Energy comparison between the 1D and the 2D models at 50 K.*

4.2 COMPARISON WITH LITERATURE MEASUREMENTS

The 2D FEM model was then compared to a set of literature measurements [49]. The tape considered and the geometry simulated are the same of the convergence study described in Chapter 3, Fig. (3.11) and Fig. (3.12) respectively. The model is able to reproduce the sample behaviour in terms of Critical Current (I_c), Minimum Quench Energy (MQE) and Normal Zone Propagation Velocity ($NZPV$).

The parameters which affect simulation results could be divided in three different categories:

1. the geometrical parameters like the thickness of the layers, the length of the thermally anchored area and the length of the heater;

2. the operating parameters like the initial temperature, the operating current and the energy deposited in the tape by the heater;

3. the material properties like the thermal and electric conductivity of the different layers and the superconducting parametrization set.

Among these different parameters two of them are hard to measure while having great impact on the results: the Residual Resistivity Ratio (RRR) of the copper and the electrical conductivity of the buffer layer.

The RRR is defined as the ratio of the resistivity of copper at 293 K to the resistivity at 4 K:

$$RRR = \frac{\rho(293 \text{ K})}{\rho(4 \text{ K})} \tag{4.1}$$

This parameter gives a first rough indication of the copper purity. A higher value of RRR means a better electrical conduction and a lower heat dissipation. Estimation of the copper RRR for different tape manufacturers are reported in [50]. From these informations a reference RRR value of 20 for the American Superconductor and a value of 40 for the SuperPower® inc. YBCO tapes was chosen.

The buffer layer is not considered as an element in the model. Its presence is simulated by the addition of an electric and thermal resistance between the YBCO and the substrate layers. Many studies have been performed on the influence of this layer of the tape [51, 52, 53]. While its high resistance is well established, proper values for both thermal and electric conductivity are not been found yet. In order to have a rough estimation of the electrical conductivity of the buffer layer a set of transversal voltage measurements at different temperatures, performed at the Frascati research center [54], were simulated. The measurements were performed on a 3 cm long Stabilizer
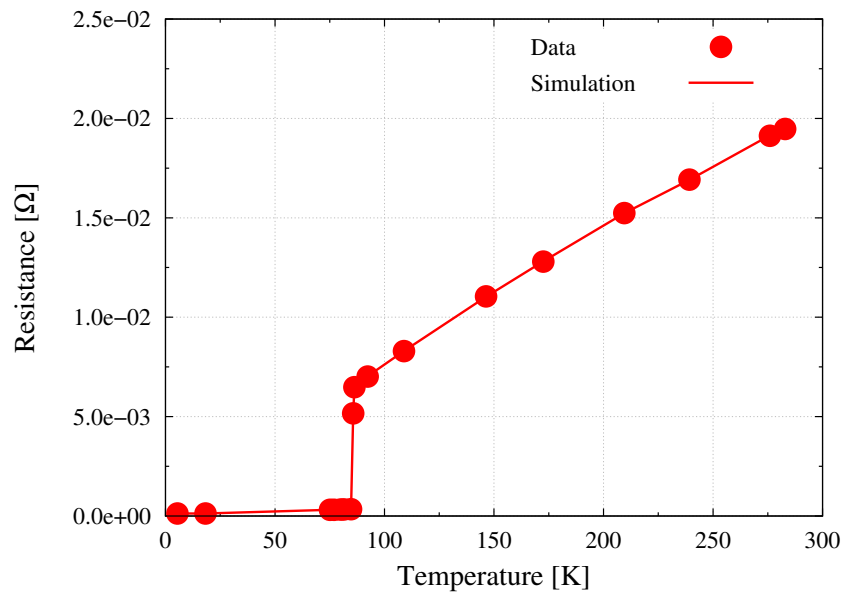
Figure (4.5)   *Resistance as a function of temperature of a 3 cm long Stabilizer Free YBCO tape. The dots refers to measurements while the line refers to simulations.*
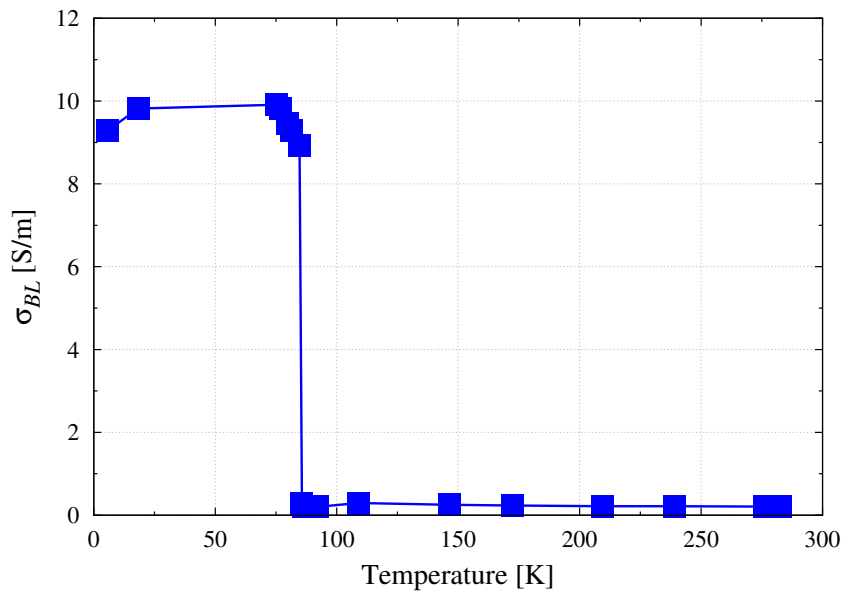
Figure (4.6)   *Buffer layer transversal electrical conductivity as a function of temperature.*

Free YBCO tape manufactured by SuperPower® inc. with a four terminal sensing. The current was fed into the tape at both ends, one on the upper face while the other on the bottom face of the tape. The voltage taps where soldered between the current leads on both faces too and at a distance of 2.2 cm. The numerical simulations of these measurements were carried out with the anisotropic finite element model developed. A parametric sweep on the buffer layer transversal electrical conductivity were performed for every temperature since the relative error with respect to measurement was less than 1 %, as shown in Fig. (4.5).

However, these measurements are not satisfactory for the determination of the buffer layer transversal electrical conductivity since it exhibits a discontinuity near the critical temperature, as shown in Fig. (4.6). This behaviour seems correlated to the transition from the normal to the superconducting state, suggesting that the longitudinal resistance measurement has a non negligible impact on the measurement campaign. Anyhow, the result of this
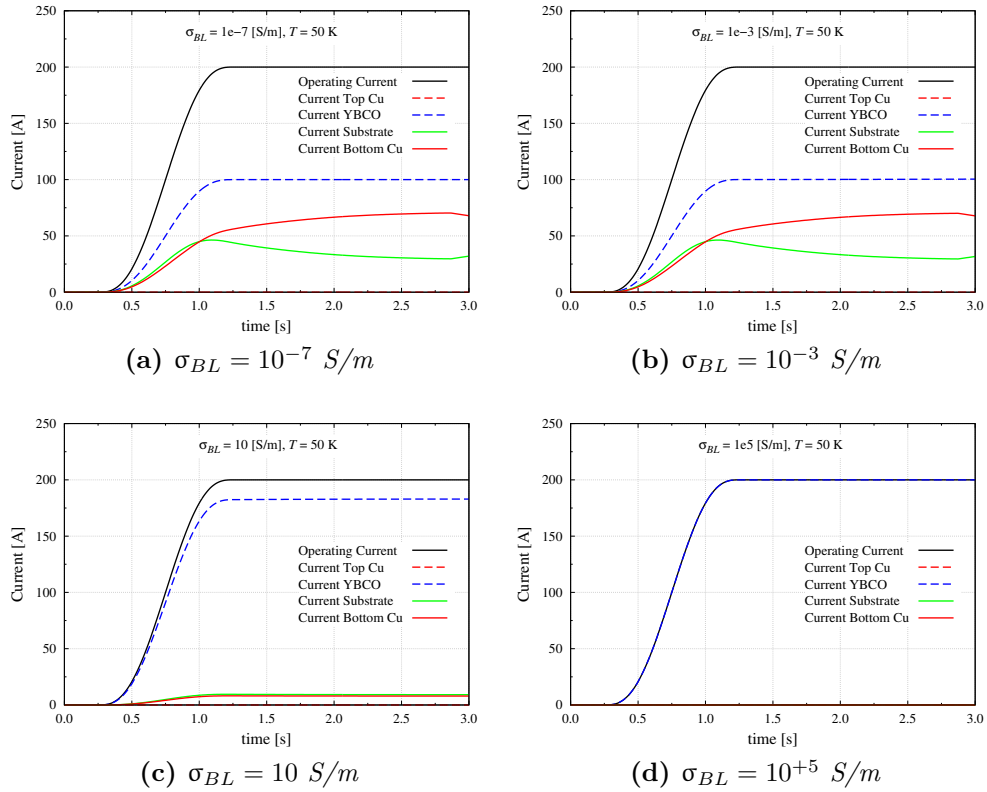
Figure (4.7) *Current distribution among the YBCO CC layers at different values of the buffer layer transversal electrical conductivity.*

study was taken as a rough approximation of the buffer layer transversal electrical conductivity. The value chosen for simulations was 10 S/m, that is the measured values in the superconducting regime, where the longitudinal resistance of the tape is negligible with respect to the transverse one.

The presence of the resistive layer inside the YBCO CC tape causes an asymmetry since the buffer layer is not placed in the middle of the tape thickness, as reported in Fig. (3.11). The value of this internal resistance also affects the current distribution inside the tape, dividing it into two parts characterized by different thickness. One part, the upper one, is dominated by the superconducting layer in the superconducting state and by the copper in the normal state. The bottom part always contributes to power dissipation since is mainly composed by copper and by the stabilizer material. The impact of the buffer layer resistance on current redistribution inside the tape is shown in Fig. (4.7). The higher the resistance, the lower the ratio between the current which flows in the superconducting layer and the operating current, even in the superconducting state.
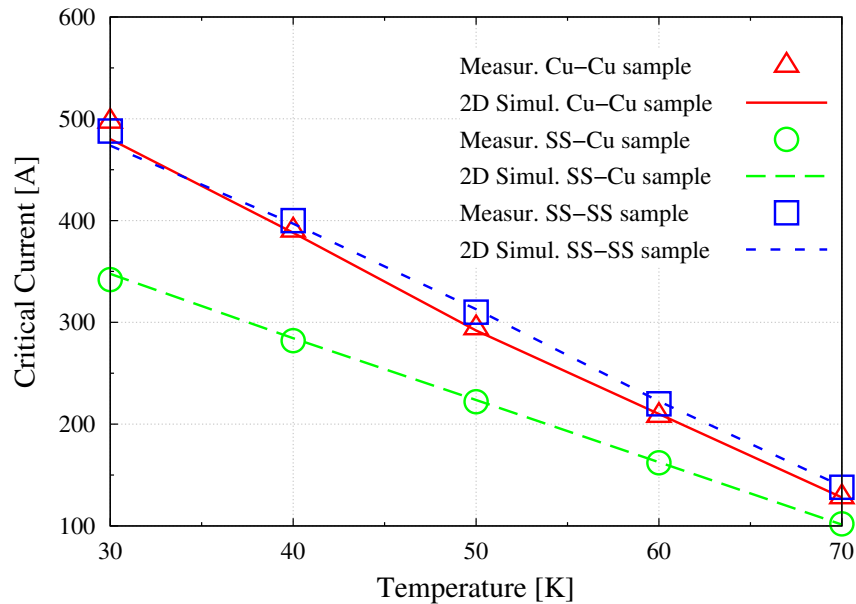
Figure (4.8)   *Critical current as a function of temperature for three different types of tape.*

4.2.1 Critical Current

Fig. (4.8) shows the measured end-to-end critical current (I_c) in comparison with the results predicted by the FEM model. The three curves refer to tapes with different stabilizers: the red curve has a copper layer for both top and bottom stabilizers, the blue one has a stainless steel layer for both top and bottom stabilizers while the green one has a copper layer for the top stabilizer and a stainless steel layer for the bottom stabilizer. The geometry of the three tapes considered are different since the copper and the stainless steel stabilizer layers have different thickness, respectively 50 μm and 26 μm.

The computed values are obtained considering a constant current and the relative self filed, calculated by Eq. (3.18). The critical current is defined as the minimum operating current able to generate an electric field greater than the critical filed: $E_0 = 10^{-4}$ V/m. It is important to underline that the variation of the copper RRR does not have a significant impact on the critical current computed.

4.2.2 Minimum Quench Energy

The results of the comparison between the measured and the calculated MQE for the Cu-Cu tape are reported in Fig. (4.9). The Minimum Quench Energies measured ranges from 0.29 to 1.02 J between 30 and 70 K and, as expected, decrease with increasing operating current density at constant temperature.

The simulation runs are performed with a parametric sweep on the power deposited in the tape, increased in steps of 0.05 W. As soon as the maximum tape temperature reaches 200 K the simulation is stopped and the Minimum Quench Energy is calculated by the following formula:

$$MQE = P \cdot t_{pulse} \qquad [\text{J}] \tag{4.2}$$

where P [W] is the total power generated by the heater and t_{pulse} [s] is the duration of the heat pulse which is equal to 0.25 s.

Fig. (4.9) clearly shows that the measured values are well above the predicted MQE for the tape considered, resulting in an excessively underestimation of its stability. However, it is well known the difficulty of quantifying the amount of energy from the heat pulse that is actually deposited in the tape. While in reality a heat dispersion is present, the numerical model is characterized by a perfect thermal contact between the heater and the tape. Hence, the whole heat generated is deposited in the tape and no heat leaks are simulated.
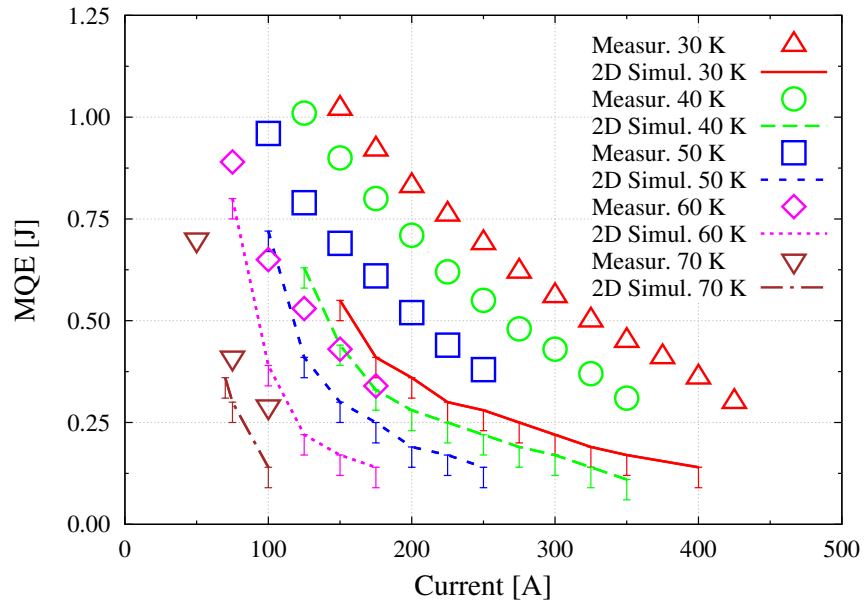
Figure (4.9)   *Minimum Quench Energy: Measured values versus Simulated values.*
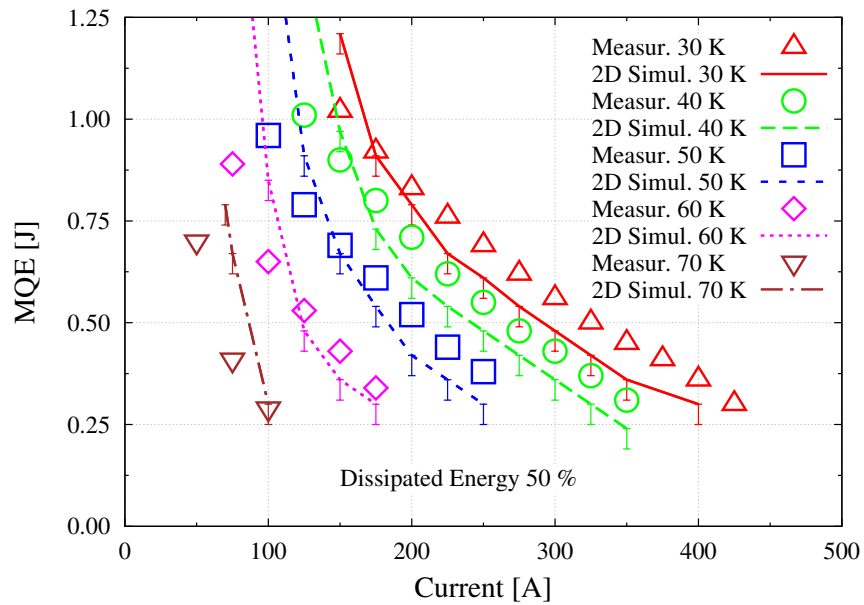
Figure (4.10)   *Minimum Quench Energy: Measured values versus Simulated values considering 50% of energy dispersion.*

Considering about 50% of heat pulse dispersion the measurements and calculated MQE are in excellent agreement, as reported in Fig. (4.10). The calculated curves have the same trend of the measured ones except at lower current where the model overestimates the tape stability. The uncertainty in the heat deposited could be due to different causes:

1. the difficulty of accurately measuring the heat capacity of wire and epoxy resin used to attach the heater to the tape;

2. the heat leak due to conduction through the wire;

3. the heat leak due to radiation towards the external environment.

4.2.3   Normal Zone Propagation Velocity

When the heat deposited inside the tape is greater then the MQE, the normal zone starts to propagate along the whole cable with a steady velocity called Normal Zone Propagation Velocity ($NZPV$).
The $NZPV$ is defined as

$$NZPV = L/\Delta t \qquad [\text{m/s}] \tag{4.3}$$

where L is the distance between the midpoints of two consecutive voltage tap pairs and Δt is the time difference between the achievement of a reference voltage at both voltage tap pairs ($V_{ref} = 1$ mV).

A typical time evolution of the differential voltage signals is reported in Fig. (4.11), indicating both the reference voltage and the time delay considered in Eq. (4.3). Fig. (4.12) shows the comparison between the measured and the simulated $NZPV$ with respect to voltage taps V_{21} of Fig. (3.12). The $NZPV$ is plotted as a function of the ratio between the operative transport current and the critical current at fixed temperature. The trend of the curves is almost linear with a rather good agreement between experiments and simulations in the range of temperature between 50 and 70 K. At lower temperatures the computed $NZPV$ are overestimated as the current ratio tends towards one. The $NZPV$ measured ranges from 8.00 to 82.00 mm/s between 30 and 70 K. The average relative percentage error between measurements and simulation is equal to 15.97% while the minimum and maximum errors are 0.34% and 75.76% respectively.

In Fig. (4.13) the $NZPV$ is reported as a function of the operative current. As can be seen, the model underestimate the Minimum Propagating Current (MPC) that is the maximum current at which the $NZPV$ is equal to zero. This behaviour is in agreement with the overestimation of the MQE at lowest current discussed above.
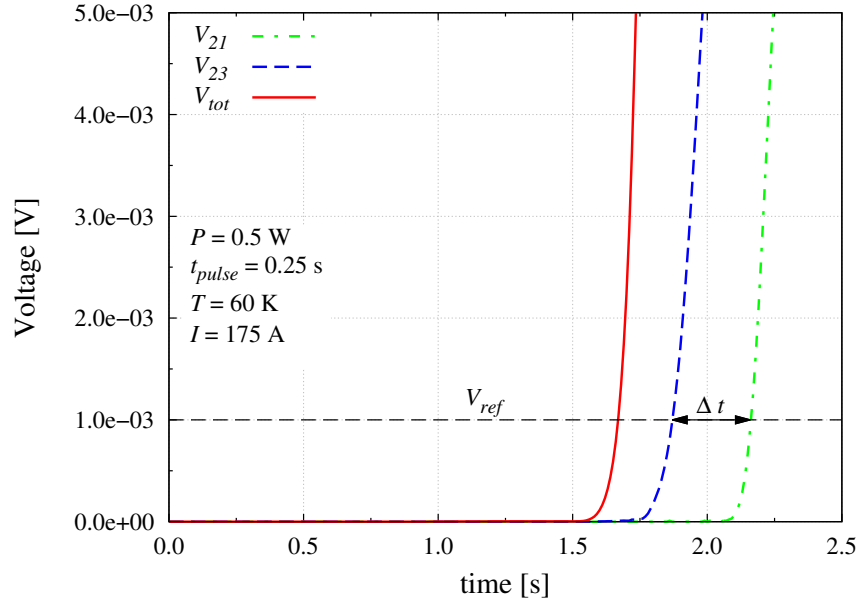
Figure (4.11)   *Time evolution of the differential voltage signals for a quench run. The dashed black horizontal line is used to underline the reference voltage $V_{ref} = 1\ mV$.*

Fig. (4.14a) and Fig. (4.14b) show the Hot Spot Temperature (T_{max}) and the Burn Out Time (t_{burn}) of the YBCO tape as functions of the operative current. The T_{max} is defined as the maximum temperature reached in the recovery characterized by the maximum energy, immediately before the MQE. The t_{burn} is the time required to achieve a fixed temperature, considered dangerous for the tape integrity; in this study fixed at 200 K. The selected temperature is not dangerous by itself but, since the quench is characterized by a short time constant, of the order of tens of milliseconds, a conservative value is more suitable.

In Fig. (4.15) a typical evolution of the temperature distribution along the tape is reported for a quench run at 70 K and 70 A with a heat power deposited of 2.0 W. The pulse heat starts after 1.55 s and lasts up to 1.77 s. In the top left box the time evolution of the maximum temperature, located in the middle of the heater, is reported. At different times, indicated by red dots, the temperature distribution is shown. As can been seen the temperature is constant before the heat pulse, since the operative current is less than the critical current. During the pulse the temperature increases, reaching a maximum immediately after the end of the pulse. Then the temperature decreases due to the absence of the external heat source. However, a certain
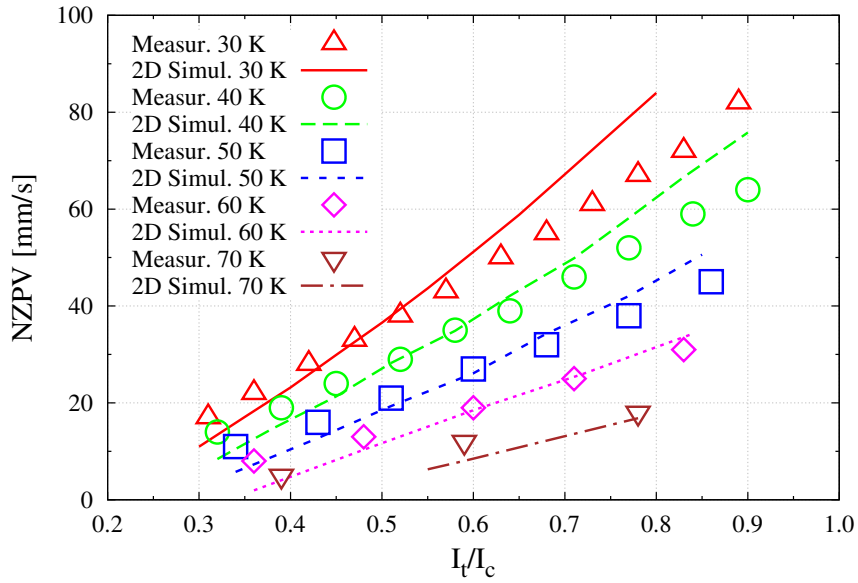
Figure (4.12) *Normal Zone Propagation Velocity as a function of the ratio between the operative and the critical current at different temperatures.*
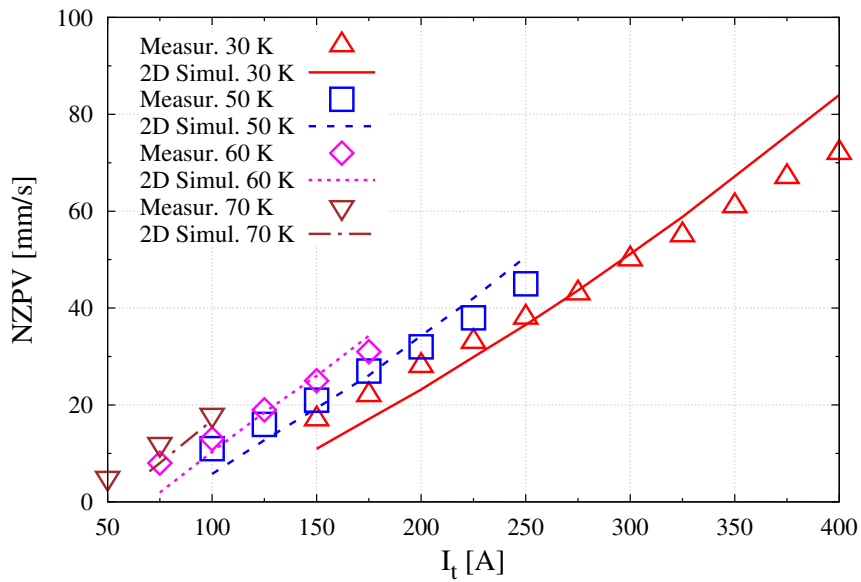
Figure (4.13) *Normal Zone Propagation Velocity as a function of the operative current at different temperatures.*

length of the tape has undergone the transition to the normal state, thus an internal Joule heat source is present. When the heat produced by the resistive zone is grater than the heat extracted by conduction cooling, as in the selected case, the temperature rises again, this time irreversibly.
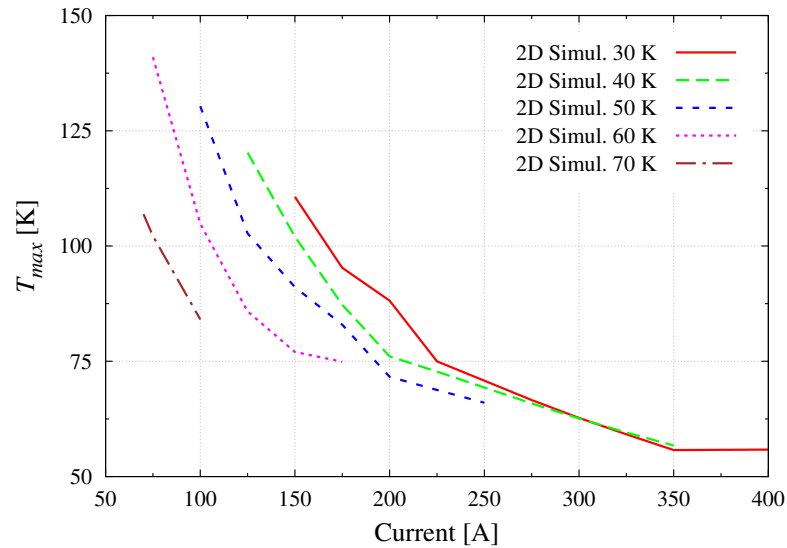
(a) *Hot Spot Temperature as a function of the operative current at different temperatures.*
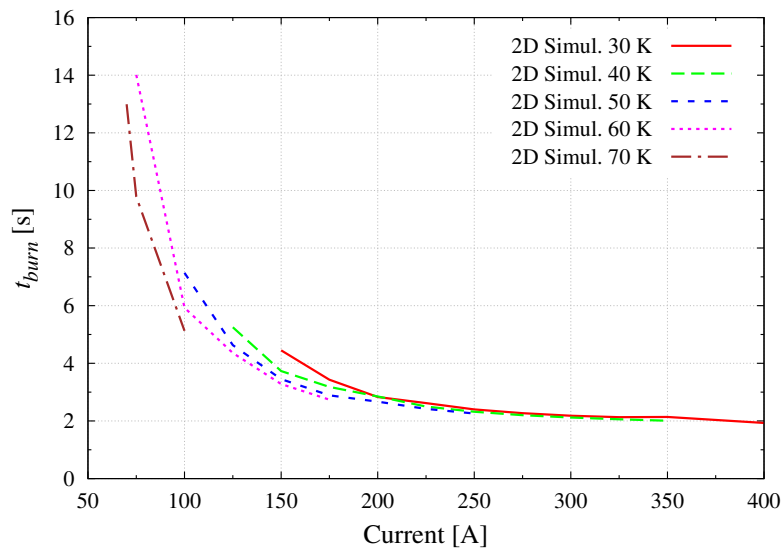
(b) *Burn Out Time as a function of the operative current at different temperatures.*

Figure (4.14)
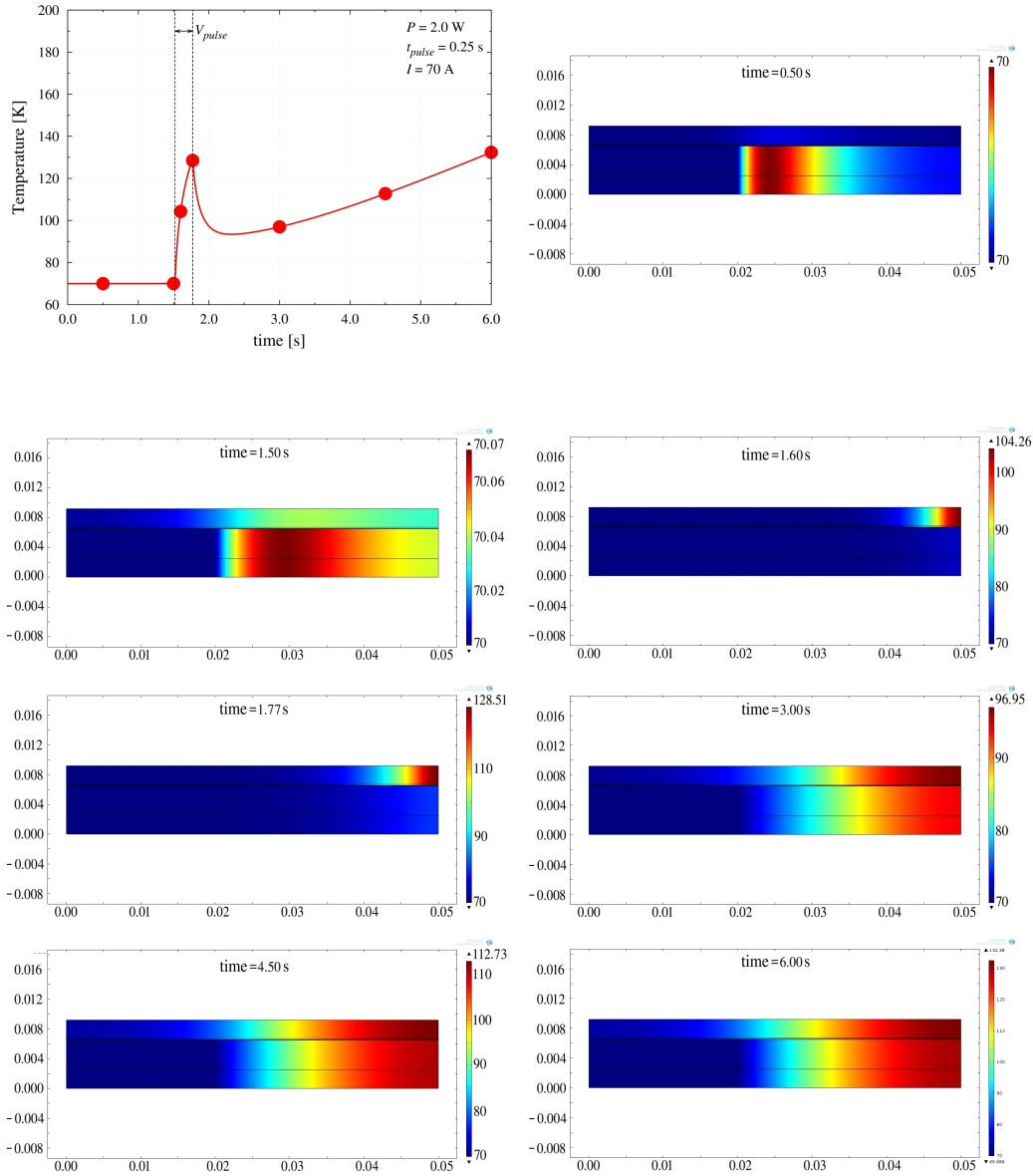
Figure (4.15) *Temperature distribution evolution along the tape during a quench run.*

4.3 COMPARISON WITH IN SITU MEASUREMENTS

In this section the numerical model developed is compared to the measurements obtained inside the cryogenic facility. The resistance of the tape as a function of temperature as well as the critical current and quench measurements are described and the agreement with the numerical simulations is discussed.

4.3.1 Superconducting Transition

The first comparison between the results of the 2D anisotropic FEM model and the measurements made in the developed facility was carried out on the tape resistance as a function of temperature. This simple measurement consists of a four terminal sensing with an operating current equal to 1 A. The current is fed in the copper bus bar, as described in Section (2.5), while the voltage is taken on the YBCO side of the tape on a 24 cm long length.

Fig. (4.16) reports the resistance of an SCS600-AP YBCO tape, manufactured by SuperPower® inc., as a function of the maximum temperature measured on the sample. In fact, since the tape is cooled only by conduc-
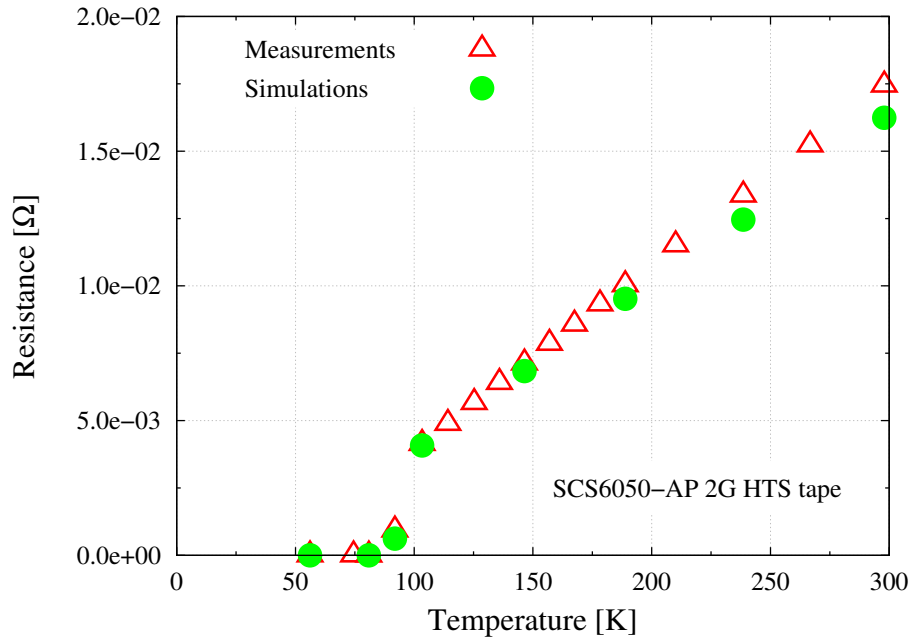
Figure (4.16) *Measurements and simulation of the transition from normal to superconducting state of a 2G YBCO tape.*

tion inside the cryostat, the temperature is not uniform and it varies with a profile similar to that shown in Fig. (4.17). The numerical simulations are performed with these initial temperature profiles. In order to ensure its stationarity until the heat pulse start, a heat distributed input over the whole upper surface of the tape is computed for each measurement.

Measurements and simulations are in good agreement, the resistance of the tape decreases linearly with decreasing temperature until the critical temperature is reached. Around 92 K the resistance suddenly drops to non measurable values indicating that the transition from the normal to the superconducting state has occurred. This correspondence implies consistency in the electrical material properties. Small differences between measured and computed resistances are visible in the normal conducting region. However, this error, of about 5% on average, reduces with decreasing temperature and it is probably due to the approximation made on the initial temperature profile.
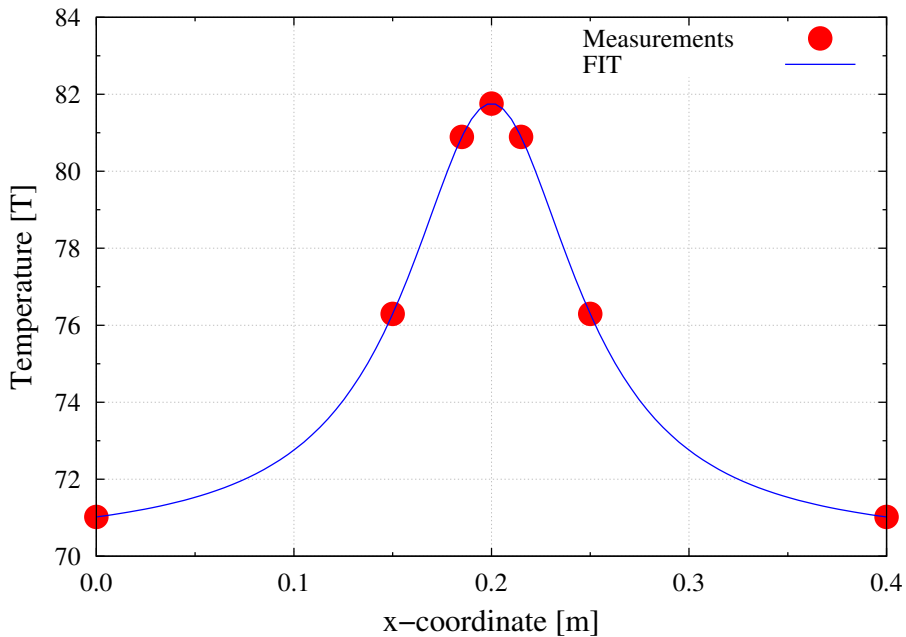
Figure (4.17) *Initial temperature profile during measurements. The red dots indicate the temperature measured while the blue line is the temperature profile obtained from their fit.*

4.3.2 Critical Current

After the resistance measurements and the reaching of the superconducting regime, the critical current of the sample is evaluated. The heater mounted on the 2nd stage of the cryocooler is controlled by the Temperature Controller and the measurements starts when the desired maximum temperature on the sample is reached. The current is then incremented by steps as already discussed in Section (2.6.1).

The I_c obtained on the YBCO SCS6050-AP are reported in Fig. (4.18) together with the results of the superconductor parametrization fitting function, calculated with Eq. (3.6). The continuous and the dashed line are the best curves which fit measurements with an external magnetic flux density of 0 T and in self field respectively. It is clear from this comparison that the self field has to be taken into account in the definition of the superconducting parameters.

In Fig. (4.19) and Fig. (4.20) the electric field evolution during the measurement performed at 87.35 K and the $E\text{-}I$ characteristic of the one performed at 84.55 K are reported. The computed and experimental electric
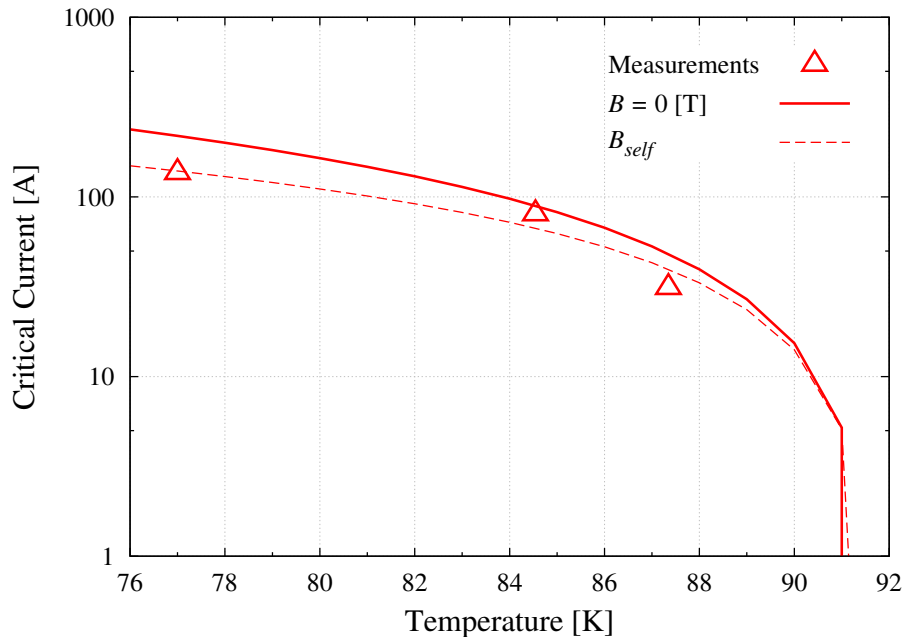
Figure (4.18) *Critical current of an YBCO SCS6050-AP tape as a function of temperature. The lines represent the expected values obtained with the superconductor parametrization.*
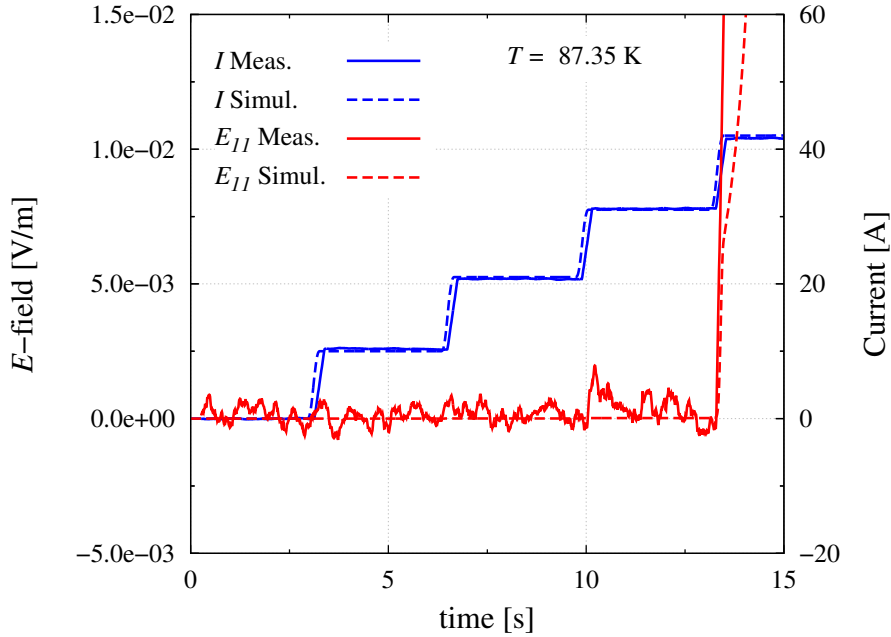
Figure (4.19)   *Electric field evolution during a critical current measurement. The solid lines represent experimental values while the dashed line are computed by the anisotropic model.*

field traces show very good agreement over the whole measurement. However the corresponding temperatures, reported in Fig. (4.21), have remarkable differences. The temperature evolution in the hot spot, located just below the heater in the middle of the tape, has a steep trend characterized by a sudden growth once exceeded the critical current value. A good agreement could be achieved thanks to the introduction of the temperature sensors thermal mass and the tuning of the transversal thermal resistances between the tape and the diodes. With a thermal resistance $k_{diode} = 0.01$ W/m·K the computed and the measured temperature have similar trends. However, the experimental value decreases until the electric field starts to grow. This behaviour is not caught by the model since the initial temperature profile is considered stable.

This result, confirmed by the minimum quench energy study that will be discussed in the next section, clearly indicate that the thermal mass of the sensors is not negligible and the substitution of the diodes with smaller temperature probes is mandatory for more reliable temperature control of the YBCO tapes.
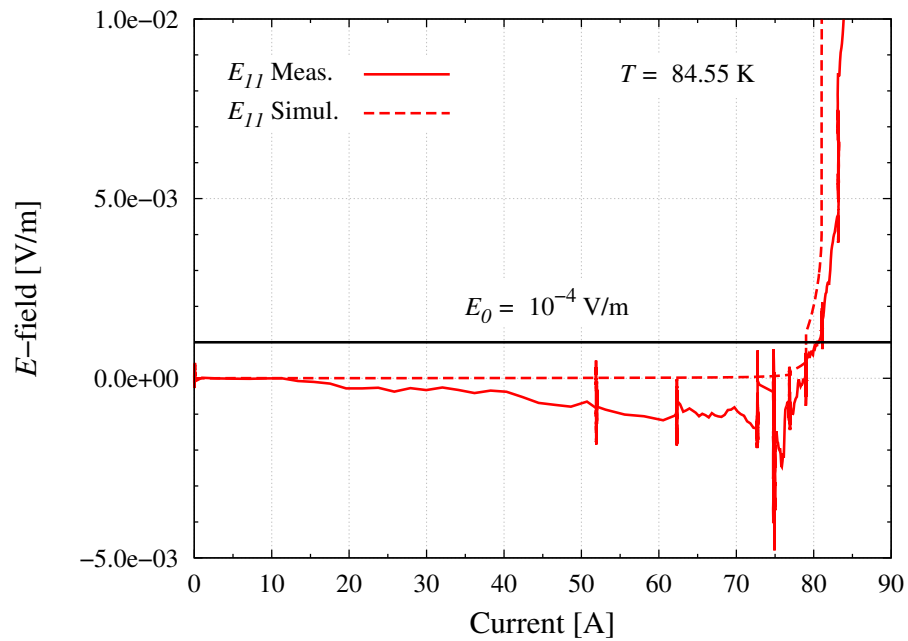
Figure (4.20) *E-I characteristic of the YBCO SCS6050 tape at 84.55 K.*
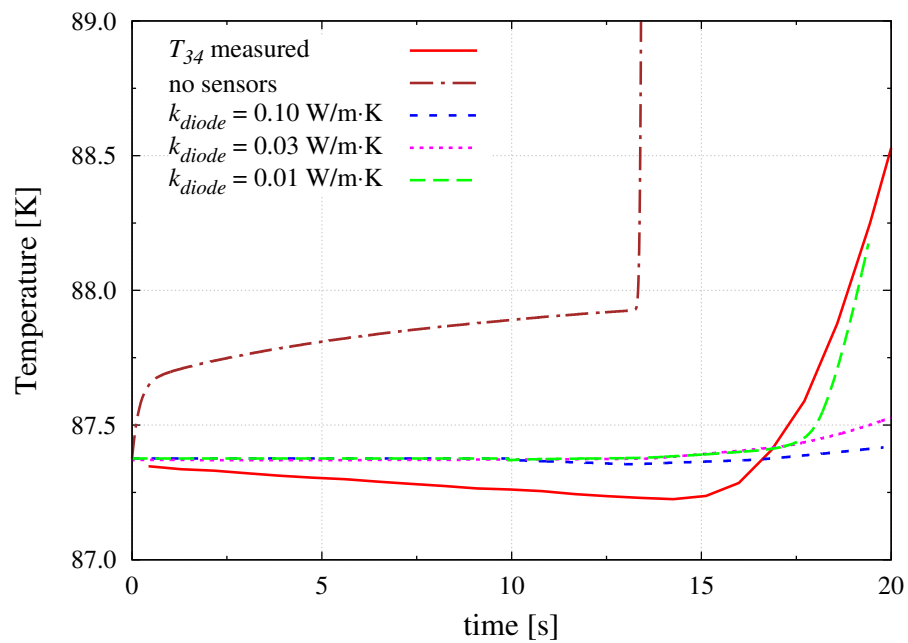
Figure (4.21) *Temperature evolution during a critical current measurement: measurement vs. simulations.*

4.3.3 Minimum Quench Energy

Once the critical current as a function of temperature has been defined, the thermal stability of the sample can be investigated. During minimum quench energy measurements a voltage pulse is induced in the heater attached to the tape, thus depositing heat inside it, while the current is kept constant. The analysis is performed increasing or decreasing the external heat power until the minimum energy which causes an irreversible transition to the normal conducting state occurs at fixed temperature and ratio between the transport and the critical current.

Typical voltage evolutions during a recovery and a quench are reported in Fig. (4.22) and Fig. (4.23) respectively. In the first case the total voltage measured grows up to about 5.0e-4 V during the feeding of the heater resistor and returns to be unmeasurable 0.5 s after the pulse end. Increasing the heat power produced from 1.2 W to 1.3 W, in the same operating conditions, the voltage exceeds the voltage threshold of 0.01 V and the current power supply is switched off. In this case the transition is considered irreversible, the quench occurs and the minimum quench energy is recorded. In the same graphs the results of the simulations are reported.
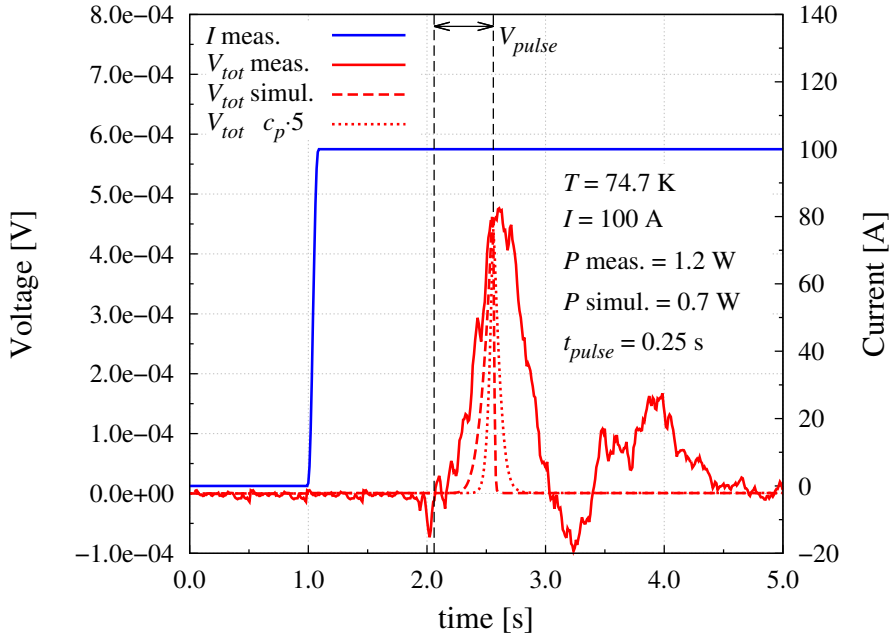
Figure (4.22)   *Voltage evolution during a recovery measurement and simulations.*

In the recovery case the computed and the experimental voltage are similar during its growth but the sample recovers the superconducting state as soon as the heater is switched off. In order to better reproduce the voltage profile a parametric study on the thermal properties were carried out. The sudden fall of the voltage, at the end of the heater pulse, is removed increasing the specific heat of the tape multiplying it by five. The voltage trends are now similar but the computed one is sharper. A detailed study of the possible causes of this difference should to be carried out as well as an accurate check of the reliability of voltage measurements.

In the quench case the model is able to reproduce the voltage evolution with only a small difference in the time at which the voltage starts to grow. However, both cases require a heat power input equal to about half of the measured one. These results indicate that during measurements not the whole heat produced by the heater is actually deposited inside the tape, confirming what explained in Section (4.2).
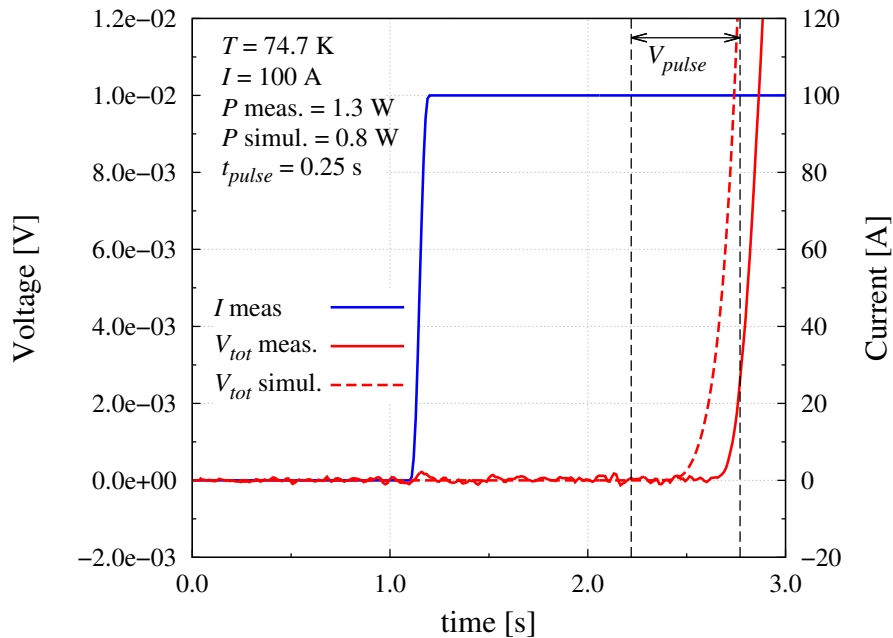
Figure (4.23) *Voltage evolution during a quench measurement and simulations.*

T [K]	$c_{p,Cu}$	$c_{p,Ag}$	$c_{p,Hast}$	$c_{p,YBCO}$	$c_{p,NiW}$	$c_{p,SS}$
5	0.192	0.232	0.740	0.667	38.180	2.481
10	1.206	1.798	1.929	3.470	38.180	5.489
15	3.839	6.844	4.017	7.182	38.180	9.545
20	8.814	15.675	7.452	11.678	38.180	15.128
25	16.706	28.521	12.684	16.845	38.180	22.645
30	27.860	44.477	20.163	22.575	38.180	32.404
35	42.327	61.540	30.337	28.772	38.180	44.590
40	59.843	78.557	43.656	35.345	38.180	59.238
45	79.863	94.071	56.207	42.211	52.277	76.231
50	101.648	108.070	71.974	49.296	68.180	95.306
55	124.375	120.610	88.773	56.529	85.279	116.082
60	147.250	131.810	106.087	63.851	103.045	138.101
65	169.590	141.800	123.476	71.204	121.030	160.865
70	190.872	150.690	140.590	78.541	138.863	183.884
75	210.741	158.610	157.174	85.818	156.255	206.713
80	228.996	165.670	173.058	92.997	172.995	228.968
85	245.558	171.970	188.134	100.045	188.951	250.348
90	260.444	177.590	202.350	106.935	204.073	270.632
92	265.945	179.670	207.791	109.641	209.891	278.403
100	285.529	187.130	228.165	120.153	233.139	307.396
150	349.243	213.880	314.429	172.814	328.584	419.439
200	369.317	225.200	359.082	207.129	382.863	462.098
250	377.036	231.760	385.728	233.091	416.080	479.739
300	380.552	236.850	403.968	242.447	444.924	488.035

Table (A.1) *Specific heat as a function of temperature in J/(m·K).*

T [K]	k_{Cu}	k_{Ag}	$k_{Hast.}$	k_{YBCO}	k_{NiW}	k_{SS}
5	157.700	11308.000	1.497	1.261	385.300	0.410
10	313.900	12846.000	2.695	2.740	385.300	0.924
15	462.600	8193.300	3.653	4.328	385.300	1.492
20	591.200	4889.300	4.424	5.774	385.300	2.068
25	684.300	3085.400	5.048	6.929	385.300	2.627
30	731.400	2075.400	5.557	7.727	385.300	3.156
35	734.500	1472.300	5.977	8.170	385.300	3.650
40	706.100	1144.000	6.327	8.303	385.300	4.107
45	661.200	935.590	6.622	8.200	343.900	4.530
50	611.400	798.480	6.873	7.945	307.800	4.919
55	564.000	705.590	7.092	7.608	277.300	5.278
60	522.400	641.070	7.284	7.231	252.000	5.610
65	487.800	595.280	7.456	6.807	231.600	5.917
70	459.900	562.140	7.611	6.261	215.500	6.201
75	438.000	537.710	7.754	6.002	203.000	6.467
80	421.100	519.390	7.887	5.782	193.200	6.715
85	408.200	505.400	8.013	5.588	184.900	6.948
90	398.400	494.520	8.132	5.421	176.800	7.167
92	395.200	490.850	8.178	5.360	173.300	7.251
95	391.100	485.920	8.247	5.276	167.400	7.375
100	385.800	478.980	8.357	5.152	156.600	7.573
150	375.000	446.390	9.372	4.649	114.100	9.225
200	379.100	432.520	10.340	4.617	98.890	10.726
250	381.100	424.400	11.290	4.553	92.020	12.401
300	380.800	419.490	12.230	4.745	90.000	14.420

Table (A.2) *Thermal conductivity as a function of temperature in W/(m·K).*

T [K]	ρ_{Cu}	ρ_{Ag}	$\rho_{Hast.}$	ρ_{YBCO}	ρ_{NiW}	ρ_{SS}
5	8.45E-10	9.91E-12	1.22E-06	7.63E-27	1.56E-09	5.54E-07
10	8.45E-10	1.11E-11	1.22E-06	2.09E-26	1.56E-09	5.58E-07
15	8.48E-10	1.80E-11	1.22E-06	6.13E-26	1.56E-09	5.62E-07
20	8.56E-10	3.88E-11	1.22E-06	1.92E-25	1.56E-09	5.66E-07
25	8.76E-10	8.69E-11	1.22E-06	6.58E-25	1.56E-09	5.70E-07
30	9.16E-10	1.78E-10	1.22E-06	2.47E-24	1.56E-09	5.74E-07
35	9.86E-10	3.23E-10	1.23E-06	1.04E-23	1.56E-09	5.79E-07
40	1.09E-09	5.24E-10	1.23E-06	4.98E-23	1.56E-09	5.83E-07
45	1.25E-09	7.72E-10	1.23E-06	2.80E-22	1.66E-09	5.87E-07
50	1.44E-09	1.05E-09	1.23E-06	1.91E-21	1.95E-09	5.91E-07
55	1.66E-09	1.35E-09	1.23E-06	1.67E-20	2.41E-09	5.95E-07
60	1.90E-09	1.66E-09	1.23E-06	2.01E-19	3.03E-09	5.99E-07
65	2.18E-09	1.97E-09	1.23E-06	3.69E-18	3.78E-09	6.03E-07
70	2.48E-09	2.28E-09	1.23E-06	1.24E-16	4.66E-09	6.07E-07
75	2.80E-09	2.59E-09	1.23E-06	1.05E-14	5.64E-09	6.11E-07
80	3.15E-09	2.89E-09	1.23E-06	4.41E-12	6.72E-09	6.15E-07
85	3.50E-09	3.19E-09	1.23E-06	5.74E-08	7.88E-09	6.19E-07
90	3.87E-09	3.49E-09	1.23E-06	2.68E-06	9.11E-09	6.23E-07
92	4.01E-09	3.61E-09	1.23E-06	2.70E-06	9.63E-09	6.25E-07
95	4.24E-09	3.79E-09	1.23E-06	2.74E-06	1.04E-08	6.27E-07
100	4.61E-09	4.09E-09	1.23E-06	2.80E-06	1.17E-08	6.31E-07
150	8.25E-09	7.12E-09	1.24E-06	3.40E-06	2.65E-08	6.70E-07
200	1.16E-08	1.03E-08	1.25E-06	4.00E-06	4.14E-08	7.08E-07
250	1.50E-08	1.38E-08	1.25E-06	4.60E-06	5.57E-08	7.45E-07
300	1.83E-08	1.75E-08	1.26E-06	5.20E-06	6.97E-08	7.81E-07

Table (A.3) *Electrical resistivity as a function of temperature in $\Omega{\cdot}m$.*

Conclusion

The aim of this thesis, carried out at the LIMSA laboratory of the University of Bologna, is the experimental analysis and numerical simulations of quench in high temperature superconducting tapes and coils.

During the Ph.D. period an experimental apparatus for the thermal and electric characterization of superconducting tapes and coils was developed. In particular, it was necessary to assemble and test the cryocooler, the cryostat, the vacuum system, the current leads and signal feedthrough. Great effort has been made in order to define a proper mounting procedure, which allows the achievement of the temperature needed for superconductivity to occur, while ensuring quick access to samples to facilitate its instrumentation.

A dedicated data acquisition software was realized and the facility was successfully tested with critical current and quench measurements on different YBCO coated conductor tapes.

In order to simulate the quench behaviour of the HTS tapes a 2D finite element model, in the COMSOL Multiphysic® environment, was developed. The problems of a FEM analysis applied to the study of the tapes, due to their high aspect ratio, were tackled thanks to an anisotropic approach. The thickness of the tape, usually equal to 100 μm, is multiplied by a constant factor and the heat and electrical balance equations are compensated by introducing material anisotropy. The FEM model was validated comparing its results to literature measurements and to a 1D distributed parameter circuit model coupled to a thermal model. Then the FEM results were compared to the measurements performed in the facility.

Finally the model was successfully extended to the study of coils. The tape homogenized properties were defined thanks to a circuital approach in order to consider the tapes far enough from the heat source as a single element, thus savings computational time. Afterwards, the same method was used for the homogenization of a tape stack, composed by homogenized tapes electrically insulated with each other with an insulating material. This procedure allows the definition of a multi-scale hierarchical model, able to simulate the windings with different degrees of detail: the greatest precision

115

is located around the heat deposition area while gradually less details are considered with increasing distance from it.

Future Developments

Although this Ph.D. research period comes to an end, a lot of work and ideas that I had at the beginning remain unfinished. Science is a never-ending story and as we try to close a topic new questions and challenges open.

In this section I would like to briefly summarize future works to be made on the measurement facility and further developments of the simulation model.

The facility is finally working, superconducting transitions as well as critical current and quench measurements have been observed. However, everything can be improved, from the minimum temperature achieved on tape, to voltage and temperature more and more reliable and accurate, to the characterization of windings and coils. For this purpose I would soon substitute the NI-PCI board with a new one capable of measuring voltage differences up to 1 nV. Moreover, the temperature diodes have to be replaced with smaller ones, attached to the sample with the same technology used for the heater resistors, that is epoxy resin. To save costs and mounting time I think that K-type thermocouples, whose final edge should be immersed in the LN_2 used to cool down the final sections of the ambient temperature current leads, would be the better choice.

Regarding the model the first improvement would be its extension to the solution of the magnetic induction field. Its role during current redistribution may be potentially relevant during fast transitions to the normal conducting state. In second place the model could be generalized to the study of superconductors cooled by liquid coolants. Hydrodynamic processes can considerably complicate the model in terms of both memory and computational time. However, a first simplified model of liquid coolants, modelled with distributed heat power release, is under development.

Finally the homogenized model has to be validated with in situ measurements of electrical and thermal behaviour of coils and windings during quenches. An homemade winder has already been built and the design of a pancake coil is under development.

Ringraziamenti

I tre anni di dottorato sono già finiti e sono passati molto velocemente. Questa esperienza è stata davvero intensa, stimolante ed alle volte frustrante. Il confine tra un esperimento andato a buon fine e risultati completamente inattesi è stato molto sottile.

Fortunatamente in questa esperienza non sono stato da solo, al mio fianco in ogni momento, felice o meno che fosse, c'è sempre stata Alessandra. Voglio quindi cogliere l'occasione per ringraziarla di cuore e dedicarle il mio lavoro: senza di te al mio fianco non credo sarebbe stato possibile tutto questo.

Un sentito ringraziamento anche alla mia famiglia che mi ha sempre sostenuto e che mi ha fornito gli stimoli e la possibilità di cercare di realizzare le mie aspirazioni. A mio padre Claudio: anche se non te lo ho mai detto direttamente spero tu sappia che sei da sempre il motivo del mio interesse verso la scienza. A mia madre Miria per tutto quello che ha fatto per me, per avermi incoraggiato e spronato sempre. A mio fratello Fabio perchè siamo la coppia di fratelli più particolare che ci sia, e questa "biodiversità", come tu mi insegni, è senza dubbio un pregio inestimabile. Alle mie zie Lorena e Denise e ai miei zii Andrea e Luca perchè se penso al significato di famiglia e poi alla nostra famiglia allargata sento di vivere nei migliori dei mondi possibili. Infine a mia nonna Dea, perchè anche se non sei riuscita a vedermi laureato in fondo ce la ho fatta solo per una questione puramente genetica: "questo ragazzo è tutto sua nonna".

Devo poi doverosamente ringraziare il Dr. Ing. Breschi per aver creduto in me ed avermi dato non solo l'opportunità di fare il dottorato presso il Laboratorio di Ingegneria dei Magneti e Superconduttività Applicata dell'Università di Bologna, ma anche di avermi concesso il privilegio di poter lavorare nei centri di ricerca più avanzati d'Europa: il CERN di Ginevra e ITER a Cadarache. Un particolare ringraziamento lo devo anche a coloro coi quali ho lavorato spalla a spalla in tutti questi anni di ricerca. In ordine cronologico il Dr. Ing. Luca Trevisani che mi ha seguito durante la tesi triennale e il tirocinio specialistico, il Dr. Ing. Pier Paolo Granieri mio tutor durante il periodo di tesi specialistica al CERN e il Prof. Ing. Pier Luigi Ribani responsabile del

laboratorio e supervisore durante il dottorato. La vostra passione e dedizione alla ricerca e alla conoscenza sono state un grande stimolo e un riferimento. Infine un sentito ringraziamento al "tennico" Andrea Albertini per il suo costante aiuto in tutto ciò di pratico che è stato necessario fare per far funzionare l'apparato di misura e perchè se finisco sapendo fare qualcosa con le mie mani lo devo in buona parte a lui.

Un ringraziamento particolare poi a tutti coloro che mi hanno distratto dal lavoro e hanno preservato la mia umanità:

- i miei amici forlivesi, quelli che ci sono sempre anche quando sei lontano geograficamente: Oscar, Vasu, Mancio, Agno, Laura, Mari e da pochissimo Agata;

- i miei amici bolognesi, compagni di collegio e di università: Bruno, Barba, Massi, la squadraccia di basket CUSB, Mena, Plax, Chonz, Giorgio, Gigi, Corio;

- tutti coloro che sono passati per i Pick'N Rolla, in particolare: Deto, Salo, Manfre, Rossi, Papa, Poggio, Ste, Maku, Nick;

- tutti i "colleghi" del DIE-DEI con speciale menzione per: Fabio, Giacomo, Chiara C. B., Chiara L., Mauricio, Piero, Filo, Chandru, Giovanni, Paolo, Gabriele e Michele.

Bibliography

[1] V.Z. Kresin and S.A. Wolf. *Fundamentals of Superconductivity*. Plenum Press, New York, 1957.

[2] L. London and H. London. "The Electromagnetic Equations of the Supraconductor". *Proceedings of the Royal Society of London. Series A, Math. and Phys. Sciences*, **149**(866):71–88, March 1935.

[3] J. Bardeen, L. N. Cooper, and J. R. Schrieffer. "Microscopic Theory of Superconductivity". *Phys. Rev.*, **106**(1):162–164, Apr 1957.

[4] V.L. Ginzburg and L.D. Landau. "On the Theory of Superconductivity". *Zh. Eksp. Teor .Fiz*, **20**(1064), 1950.

[5] M.N. Wilson. *Superconducting Magnets*. Oxford University Press, Oxford, 1983.

[6] Lyndon Evans and other. *The Large Hadron Collider: a Marvel of Technology*. CERN and EPFL Press, Lausanne, 2009.

[7] J. G. Bednorz and K. A. Müller. "Possible High T_c Superconductivity in the Ba-La-Cu-O System.". *Zeitschrift fur Physik B Condensed Matter*, **64**(2):189–193, 1986.

[8] Thomas M. Flynn. *Cryogenic Engineering*. Marcel Dekker, New York, 2005.

[9] J. G. Weisend II. *Handbook of Cryogenic Engineering*. Taylor & Francis, 1998.

[10] J. W. Ekin. *Experimental Techniques for Low-Temperature Measurements*. Oxford University Press, New York, 2006.

[11] Omega®. *Kapton Insulated Flexible Heaters.* http://www.omega.co.uk/pptst/KHR_KHLV_KH.html.

[12] Lakeshore Cryotronics. *Cryogenic Temperature Controllers.* http://www.lakeshore.com/products/Cryogenic-Temperature-Controllers/Model-335/Pages/Overview.aspx.

[13] Ltd. Sumitomo Heavy Industries. *RDK-408D 4K Cold Head.* http://www.janis.com/products/productsoverview/4KCryocooler/RDK-408D2ClosedCycleRefrigerator.aspx#.

[14] H. M. Chang and S. W. Van Sciver. "Thermodynamic Optimization of Conduction-Cooled HTS Current Leads". *Cryogenics*, **38**(7):729–736, February 1998.

[15] M. H. Sohn, S. Kim, K. D. Sim, E. Y. Lee, H. M. Kim, H. Y. Park, K. C. Seong, and Y. K. Kwon. "Development of Cryogen Free I_c Measurement System". *Physica C*, **468**:2161–2164, May 2008.

[16] L. Ren, Y. Tang, J. Shi, N. Chen, J. Li, and S. Cheng. "Cryocooler Cooled HTS Current Lead for a 35 kJ/7 kW-class High-T_c SMES System". *Physica C*, **468**:2115–2118, June 2008.

[17] Lakeshore Cryotronics. *Solder Specifications.* http://www.lakeshore.com/products/cryogenic-accessories/solder/pages/Specifications.aspx.

[18] Lakeshore Cryotronics. *Silicon Diodes DT-670.* http://www.lakeshore.com/products/Cryogenic-Temperature-Sensors/Silicon-Diodes/DT-670/Pages/Specifications.aspx#curvedt670.

[19] Lakeshore Cryotronics. *Cryogenic Temperature Monitors.* http://www.lakeshore.com/products/Cryogenic-Temperature-Monitors/Model-211/Pages/Overview.aspx.

[20] G. E. Guadagni. *Programmare? Impariamo con LabVIEW.* Sandit Libri, 2006.

[21] GNU Octave. *High-level Language for Numerical Computations.* https://www.gnu.org/software/octave/about.html.

[22] T. Izumi, Y. Tokunaga, H Fuji, R. Teranishi, J. Matsuda, S. Asada, T. Honjo, Y. Shiohara, T. Muroga, S. Miyata, T. Watanabe, Y. Yamada,

Y Iijima, T. Saitoh, T. Goto, A. Yoshinaka, and A. Yajima. "Progress in development of coated conductors by TFA-MOD processing". *Physica C*, **412-414**:885–889, 2004.

[23] D. W. Hazelton, V. Selvamanickam, J. M. Duval, D. C. Larbalestier, W. D. Markiewicz, H. W. Weijers, and R. L. Holtz. "Recent Developments in 2G HTS Coil Technology". *IEEE Transactions on Applied Superconductivity*, **19**(3), June 2009.

[24] SuperPower® inc. *2G HTS Wire*. http://www.superpower-inc.com/content/2g-hts-wire.

[25] J. Lu, E. S. Choi, and Zhou H. D. "Physical Properties of Hastelloy® C-276^{TM} at Cryogenic Temperatures". *Journal of Applied Physics*, **103**:064908 1–6, March 2008. http://www.bnl.gov/magnets/Staff/Gupta/cryogenic-data-handbook/.

[26] M. J. T. M. Van Bellegem, R. Ankersmit H. A., van Langh, and W. Wei. "Solder on silver: historical usage and the problem of fretting". *Proceedings of Metal 2004*, October 2004.

[27] A. P. Malozemoff, S. Fleshler, M. Rupich, C. Thieme, X. Li, W. Zhang, A. Otto, J. Maguire, D. Folts, J. Yuan, H-P. Kraemer, W. Schmidt, M. Wohlfart, and H-W. Neumueller. "Progress in high temerature superconductor coated conductors and their applications". *Superconductor Science and Technology*, **21**, 2008.

[28] G. A. Levin, P. N. Barnes, J. P. Rodriguez, J. A. Connors, and J. S. Bulmer. "Stability and Normal Zone Propagation Speed in YBCO Coated Conductors with Increased Interfacial Resistance.". *IEEE Transactions on Applied Superconductivity*, **19**(3):2504–2507, June 2009.

[29] R. Brambilla. "The modelling of thin ohmic and superconducting conductors by means of integral equations". *Excerpt from the Proceedings of the COMSOL Conference*, 2007.

[30] B. Zhi-ming, W. Xia, W. Chun-li, and W. Jin-xing. "Quench propagation properties analysis of high-temperature superconductors using finite element method". *Physica C*, **436**:99–102, 2006.

[31] F. Grilli, A. Lucarelli, G. Lüpke, T. Haugan, and P. Barnes. "Dynamic Study of Field and Current Distribution in Multifilamentary YBCO Thin Films". *Excerpt from the Proceedings of the COMSOL Conference*, 2008.

[32] F. Roy, B. Dutoit, F. Sirois, and F. Grilli. "2D Magneto-Thermal Modeling of Coated High-Temperature Superconductors". *Excerpt from the Proceedings of the COMSOL Conference*, 2007.

[33] O. Chevtchenko. "Modeling of High Temperature Superconducting Tapes, Arrays and AC Cables Using COMSOL". *Excerpt from the Proceedings of the COMSOL Conference*, 2010.

[34] Chan W. K., P. J. Masson, C. Luongo, and J. Schwartz. "Three-Dimensional Micrometer-Scale Modeling of Quenching in High-Aspect-Ratio $YBa_2Cu_3O_i7 - \delta$ Coated Conductor Tapes - Part I: Model Development and Validation.". *IEEE Transactions on Applied Superconductivity*, **20**(6), December 2010.

[35] Wan Kan Chan and Justin Schwartz. "Three-Dimensional Micrometer-Scale Modeling of Quenching in High-Aspect-Ratio $YBa_2Cu_3O_i7 - \delta$ Coated Conductor Tapes - Part II: Influence of Geometric and Material Properties and Implications for Conductor Engineering and Magnet Design.". *IEEE Transactions on Applied Superconductivity*, **21**(6), December 2011.

[36] Wan Kan Chan and Justin Schwartz. "A Hierarchical Three-Dimensional Multiscale Elctro-Magneto-Thermal Model of Quenching in $REBa_2Cu_3O_7 - \delta$ Coated-Conductor-Based Coils.". *IEEE Transactions on Applied Superconductivity*, **22**(5), October 2012.

[37] F. Grilli. *"Numerical Modelling of High Temperature Superconducting Tapes and Coils"*. PhD thesis, Ecole Polytechnique Federale de Lausanne, 2003.

[38] J. Duron, L. Antognazza, M. Decroux, F. Grilli, S. Stavrev, B. Dutoit, and O. Fisher. "3-D Finite Element Simulations of Strip Lines in a YBCO/Au Fault Current Limiter". *IEEE Transactions on Applied Superconductivity*, **15**(2), June 2005.

[39] COMSOL. *COMSOL Multiphysics® User's Guide*.

[40] R Weshe, P. Bruzzone, S. March, C. Marinucci, and D Uglietti. "HTS Conductors for Fusion: Thermal Stability and Quench". *HTS for Fusion Conductor Workshop Karlsruhe 2011*, 2011.

[41] J. E. Jensen, R. B. Stewart, W. A. Tuttle, and H. Brechna. *Brookhaven National Laboratory Selected Cryogenic Data Notebook*. Unites States Department of Energy, Springfield, VA 22161, 1980.

[42] P. Bauer, H. Rajainmaki, and E. Salpietro. *EFDA Material Data Compilation for Superconductor Simulation.* Max-Planck-Institute für Plasmaphysic, 18 April 2007.

[43] M. Khoshnevisan, W. P. Pratt, P. A. Schroeder, S. Steenwyk, and C. Uher. "Low-temperature Resistivity of Silver". *J. Phys. F: Metal Phys.*, **9**(1), 1979.

[44] R. A. Matula. "Electrical Resistivity of Copper, Gold, Palladium, and Silver". *J. Phys. Chem. Ref. Data*, **8**(4):1147, 1979.

[45] A. D. Berger. "stability of sc cables with twisted stack ybco cc". Plasma Science and Fusion Center, Massachusetts Institute of Thecnology, Cambridge, USA, 2012.

[46] P. M. Knupp. "Remarks on Mesh Quality.". *46th AIAA Aerospace Science Meeting and Exhibit*, January 2008.

[47] V. M. Rodriguez-Zermeno, N. Mijatovic, C. Traeholt, T. Zirngibl, E. Seiler, A. B. Abrahamsen, N. F. Pedersen, and M. P. Sorensen. "Toward Faster FEM Simulation of Thin Film Superconductors: A Multiscal Approach.". *IEEE Transactions on Applied Superconductivity*, **21**(3):3273–3276, 2011.

[48] American Superconductor. *HTS Wire.* http://www.amsc.com/solutions-products/hts_wire.html.

[49] X. Wang, U. P. Trociewitz, and J. Schwartz. "Self-field quench behaviour of $YBa_2Cu_3O_7 - \delta$ coated conductors with different stabilizers.". *Superconductor Science and Technology*, **22**(8), 2009.

[50] M. Bonura, L. Rossi, and C. Senatore. "Thermal Conductivity of MgB_2 Wires and YBCO Tapes in High Magnetic Fields.". *11th European Conference on Applied Superconductivity*, September 2013.

[51] M. Breschi, P. L. Ribani, X. Wang, and J Schwartz. "Theoretical explanation of the non-equipotential quench behaviour in Y¿Ba¿Cu¿O coated conductors". *Superconductor Science and Technology*, **20**, 2007.

[52] Y. H. Kim, T. H. Sung, S. C. Han, Y. H. Han, N. H. Jeong, and K. No. "Characterization of a Cube Textured Cu_2O Buffer Layer on Cu Tapes for YBCO Coated Conductors". *IEEE Transactions on Applied Superconductivity*, **17**(2), June 2007.

[53] Y. Li, L. Liu, H. Liu, X. Sun, D. Hong, D. Xu, and Y. Wang. "Influence of Buffer Layer Surface Morphology on YBCO Critical Current Density Deposited on NiW Tapes". *IEEE Transactions on Applied Superconductivity*, **21**(3), June 2011.

[54] V Corato. *Personal comunication*. ENEA Frascati.

[55] P.P. Granieri. Analisi di stabilità e propagazione del quench in magneti superconduttori per acceleratori di particelle. Master's thesis, Università degli studi di Bologna, 2007.

[56] M. Breschi. *Current Distribution in Multistrand Superconducting Cables*. PhD thesis, Università di Bologna, 2001.

[57] L. Bottura. "Modelling Stability in Superconducting Cables". *Physica C*, **310**:316–326, December 1998.

[58] E.D. Marquardt, J.P. Le, and R. Radebaugh. "Cryogenic Material Properties Database". *Presented at the 11ᵗʰ International Cryocooler Conference*, page 7, June 2000.

[59] F.W. Grover. *Inductance Calculations*. Dover Publications, New York, 1962.

[60] L. Bottura, C. Rosso, and M. Breschi. "A General Model for Thermal, Hydraulic and Electric Analysis of Superconducting Cables". *CERN LHC Project Report 358*, page 27, 2000.

[61] L. Pantieri. L'arte di scrivere con LaTeX. http://www.guit.sssup.it/.

[62] T. P. Sheahen. *Introduction to High-Temperature Superconductivity*. Plenum Press, New York, 1994.

[63] U. Besi Vetrella, G. Celentano, M. Marchetti, G. Messina, L. Morici, P. Sabatino, R. Viola, and A. della Corte. "HTS Coils Fabrication From Commercial 2G YBCO Tapes: Measurements and Simulation.". *IEEE Transactions on Applied Superconductivity*, **24**(3), 2014.

[64] J. A. Demko and R. C. Duckworth. "Cooling Configuration Design Considerations for Long-Length HTS Cables.". *IEEE Transactions on Applied Superconductivity*, **19**(3), June 2009.

[65] M. J. Gouge, J. A. Demko, R. C. Duckworth, D. T. Lindsay, C. M. Rey, M. L. Roden, and J. C. Tolbert. "Testing of an HTS Power Cable Made From YBCO Tapes.". *IEEE Transactions on Applied Superconductivity*, **17**(2), June 2007.

[66] R. Grabovickic, J. W. Lue, M. J. Gouge, M. J., J. A. Demko, and Duckworth. "Measurements of Temperature Dependence of the Stablity and Quench Propagation of a 20-cm-Long RABiTS Y-Ba-Cu-O Tape.". *IEEE Transactions on Applied Superconductivity*, **13**(2), June 2003.

[67] G Celentano, G. Messina, A. Agrisani Armenio, A. Augeri, F. Fabbri, V. Galluzzi, A. Mancini, F. Rizzo, A. Rufoloni, A. Vannozzi, U. Gambardella, A. Saggese, G Iannone, and P Sabatino. "Quench Behavior of a Conduction Cooled $YBa_2Cu_3O_{7-x}$ Tape Pancake Coil.". *IEEE Transactions on Applied Superconductivity*, **23**(3), June 2013.

[68] G Celentano, G. M. Polli, A. Agrisani Armenio, A. Augeri, V. Galluzzi, A. Mancini, A. Rufoloni, A. Vannozzi, U. Gambardella, A. Saggese, and S Pace. "Hot Spot Simulated Transition in YBCO Coated Conductors: Experiments and Simulations.". *IEEE Transactions on Applied Superconductivity*, **19**(3), June 2009.

[69] A. Agrisani Armenio, A. Augeri, G. Celentano, V. Galluzzi, A. Mancini, A. Rufoloni, A. Vannozzi, U. Gambardella, A. Saggese, P. Sessa, and S Pace. "Stability Measurements on YBCO Coated Conductors.". *IEEE Transactions on Applied Superconductivity*, **18**(2), June 2008.

[70] G. M. Zhang, D. J. Knoll, D. N. Nguyen, P. Sastri, X. Wang, and J. Schwartz. "Quench Behaviour of $YBa_2Cu_3O_7$ Coated Conductor with AC Transport Current.". *IEEE Transactions on Applied Superconductivity*, **17**(4), December 2007.

[71] H. Song and J. Schwartz. "Stability and Quench Behaviour of $YBa_2Cu_3O_{7-x}$ Coated Conductor at 4.2 K, Self-Field.". *IEEE Transactions on Applied Superconductivity*, **19**(5), October 2009.